Development and Optimization of Analytical Methods to Study Neurochemistry Using Capillary Liquid Chromatography

by

Michael Trey Rerick

Bachelor of Science in Chemistry, University of Pittsburgh, 2015

Submitted to the Graduate Faculty of the
Dietrich School of Arts and Sciences in partial fulfillment
of the requirements for the degree of
Doctor of Philosophy

University of Pittsburgh

2021

UNIVERSITY OF PITTSBURGH

DIETRICH SCHOOL OF ARTS AND SCIENCES

This dissertation was presented

by

Michael Trey Rerick

It was defended on

August 2, 2021

and approved by

Dr. Adrian C. Michael, Professor, Department of Chemistry

Dr. Shigeru Amemiya, Professor, Department of Chemistry

Dr. Nathan Yates, Associate Professor, Department of Cell Biology

Dissertation Director: Dr. Stephen G. Weber, Professor, Department of Chemistry

Development and Optimization of Analytical Methods to Study Neurochemistry Using Capillary Liquid Chromatography

Michael Trey Rerick, Ph. D.

University of Pittsburgh, 2021

In recent decades, advances in probing the neurochemical environment of the brain have led to a deeper understanding of how behavioral and clinically relevant information is encoded. Regulation of neuronal release and reuptake mechanisms and hydrolysis breakdown influences a broad range of biological processes, and the dysregulation of these mechanisms has been linked to neurological disorders of clinical importance. It is therefore imperative that technology to sample the fragile tissue of the brain and to detect signaling molecules be improved. Efforts to develop minimally invasive approaches with high spatial resolution, temporal resolution, and selectivity lie at the forefront of this research to further our knowledge of the central nervous system. In this work, we investigate methods to improve the temporal resolution and density of information for online measurements of microdialysis coupled high-performance liquid chromatography. Through the incorporation of temperature-assisted solute focusing (TASF), we were able to develop a method for 1-minute simultaneous monitoring of two clinically relevant neurotransmitters, dopamine (DA) and serotonin (5-HT). Microdialysis methods were further investigated using capillary LC-MS/MS methods to validate long-term microdialysis membrane integrity in traumatic brain injury animal models. Lastly, a 3D printable device was developed combining electroosmotic perfusion and microdialysis sampling for a novel approach to neurochemical monitoring. This device is less invasive than traditional microdialysis

implantation, and provides more control over tissue residence time than passive diffusion approaches. Finite element models to study fluid flow were also concurrently developed and compared to experimental data to determine the validity of results relative to theory.

Table of Contents

List of Tables

List of Figures

List of Equations

Acknowledgments

I first want to thank my family for their love and support over the years as I pursued continuing my education. I am forever grateful to my wife, Lindsey, for her unwavering support over the years. Despite all of the challenges, you were always by my side with strength and optimism encouraging me to continue forward. Thank you to my parents and brother for always pushing me to believe in myself and for the inspiration to pursue my goals. I wouldn’t be where I am today without you all.

I have been fortunate during my time at the University of Pittsburgh to learn and connect with many incredible people. Thank you to my graduate advisor, Dr. Stephen Weber for the freedom to pursue a variety of research areas and the guidance to develop as a professional. Thank you to my undergraduate advisor and research collaborator, Dr. Adrian Michael, for providing mentorship and support during the times I needed it most. Thank you, Dr. Michelle Ward, for inspiring me to pursue a career and eventually a PhD in the field of analytical chemistry. Your advising was vital during a time when I was unsure of my future direction. Thank you to the past and present members of the Weber and Michael research groups, including Bart Degreef, Steve Groskreutz, Rachael Wilson, Anthony Horner, Erin Shields, Khanh Ngo, Yejin Yang, Katy Nesbitt, Erika Varner, Elaine Robbins, and Emily Gifford who I have learned so much from. A special thank you to Andrea Jaquins-Gerstl for the invaluable support and advice since I first joined as an undergraduate researcher that I will forever value. Last, I would like to thank Dr. Nathan Yates and Dr. Shigeru Amemiya for serving as my committee members and broadening my understanding of chemistry.

1.0 Overview

1.1 Liquid Chromatography

Liquid chromatography (LC) is a widespread analytical method used to separate target analytes from a given sample matrix. Separation is achieved by differences in the analyzed solutes' interactions between a solid stationary phase and a liquid mobile phase. Most commonly, a stainless-steel column is packed with a stationary phase of functionalized silica particles and the mobile phase, commonly a buffered mixture of water/methanol or water/acetonitrile, is pumped through the medium using pressure driven flow. A valve is used to introduce a low volume sample into the mobile phase flow path ahead of the column, where separation is achieved based on differences in solute affinity for the stationary phase and mobile phase. Each solute will have a retention factor, k, for a given set of chromatographic conditions, defined as the ratio of time spent interacting with the stationary and mobile phase. Variance in solute retention factors results in a range of velocities for solutes moving through the column, leading to differences in elution times. This separation technique is then paired with a detection method including UV-Vis, fluorescence, electrochemistry, or mass spectrometry to generate a chromatogram for a given sample as the solutes elute off the column.

This separation method has been used extensively within industrial and research settings due to its near universality of possible separations, and has led to its incorporation within a broad range of applications including pharmaceuticals, forensics, environmental, and medicinal study. The versatility stems from the ability to change both mobile phase composition and stationary phase surface modifications to optimize the selectivity of a given separation for the solutes of interest. Stationary phase particles are typically manufactured from porous silica, ranging in size from 1.7 – 10 µm, and modified with surface functional groups leading to various sub-branches of the technique. For example, hydrophilic interaction liquid chromatography (HILIC) silica is modified with polar functional groups, including amino- and cyano-bonded phases, and paired with nonpolar mobile phase compositions using high acetonitrile ratios.[1-3] This method has been largely successful in separations of large biomolecules including carbohydrates[4, 5] and proteins[6, 7] containing many hydrophobic and charged functional groups. However, the work contained herein focuses on the most widely used subset of LC, reversed-phase liquid chromatography (RP-LC), utilizing silica particles modified with hydrophobic C_{18} chains and polar, low methanol/acetonitrile, mobile phase compositions.[8, 9]

1.2 Defining Chromatographic System Performance

The ultimate goal of most chromatographic methods is the isolation of solutes of interest from other components within the sample mixture. Poppe described chromatography as a series of repeated equilibrations between the solute and the stationary phase selected, which ultimately leads to a separated mixture[10]. Resolving power, also referred to as efficiency, is most commonly defined by the number of theoretical plates obtained for a given set of conditions. This is derived from plate theory, first introduced by Martin and Synge[11], where each of these series of repeated equilibrations described by Poppe are equivalent to a "theoretical plate". The more equilibration steps obtained for a given system, the higher to resolving power of that separation.[12]

Experimentally, theoretical plate count, N, is determined by:

Equation 1

$$N = \left(\frac{t_R}{\sigma_t}\right)^2$$

where t_R is equal to the retention time of a given solute, and σ_t is equal to the peak standard deviation. Simply put, the more narrow the peak for a given retention time, the more efficient the separation. However, it is common for separation efficiency to be related to a given column. Specifically, relating the efficiency to the column length used, defining the theoretical plate height, H, defined as:

Equation 2

$$H = \frac{N}{L}$$

where L is equal to the length of the chromatographic column. This yields the total distance between theoretical plates, with smaller distances leading to more equilibration steps for a given column length and a more efficient separation.

Often times in HPLC separations, the sample contains a mixture of solutes that must be detected, each with a specific retention for a given set of separation conditions. Solutes with similar retention will elute off the column to the detector at the same time, resulting in overlapping, combined signals and difficulties in peak quantification when using bulk property detectors such as UV-Vis or refractive index. Resolution, a measure of the degree to which two peaks are separated under a given set of conditions, is defined as:

Equation 3

$$R_s = \frac{2\left[t_{R,B} - t_{R,A}\right]}{W_A + W_B}$$

where W_A and W_B are the baseline widths of peaks A and B respectively. Using this equation, baseline resolution between two peaks would be achieved when $R_s > 1.5$. During method development of a mixture containing more than two components, the resolution of the separation is defined by the critical pair or the adjacent peaks with the lowest degree of separation. This resolution is often defined as the critical resolution of the separation, and a target of $R_s \geq 2$ is often used[12].

1.3 Optimizing Chromatographic Performance

At its core, LC separations are a tradeoff between separation efficiency and analysis time. This must be considered when developing LC methods for real-world applications to provide enough theoretical plates for the desired separation within an acceptable timeframe. Carr et al.[13] stated that most LC methods have one of two goals in mind:

1) What is the shortest possible analysis time needed to generate a particular plate count to separate a critical pair of solutes within a mixture?
2) What are the maximum number of plates that can be generated within a given analysis time?

The former is useful when applied to high-speed separations of biomolecules with a goal of maximizing temporal resolution, while the latter is commonly used when studying high-throughput analysis of complex mixtures.

The simplest method for optimizing a given separation is through the use of the van Deemter equation to determine the optimum solvent velocity for the system. This approach, first derived by van Deemter et al. in 1956,[14] predicts plate height as a function of solvent velocity through the column while incorporating system parameters leading to solute band broadening, yielding the equation:

Equation 4

$$H = A + \frac{B}{u_e} + Cu_e$$

where u_e equals the velocity of the mobile phase through the particle bed, while parameters A, B, and C refer to various contributions to band broadening for a given system. These terms refer to eddy diffusion, longitudinal diffusion, and resistance to mass transfer respectively, and are constants determined by factors including solute diffusion coefficients, column length, and particle size. The key to this approach is that with all other factors held constant, the maximum resolving power of a separation is achieved when operating at a flow rate corresponding to the u_e, yielding the minimum H given by Eq. 4.

While this above approach does provide a useful starting point for method optimization, it is an oversimplification to state that the optimum flow rate for a given separation always corresponds to the van Deemter minimum H value. Significant efforts have been made within the chromatographic community to improve efficiency and speed of separations, with advancements made in sub-2 µm particles[15, 16], ultra-high pressure pumps[17, 18], and micropillar arrays[19, 20]. This expands the tools available to optimize not only the flow rate, but the entire system governing the separation to suit the needs of the study.

Only by simultaneously optimizing flow rate, column length, and particle size can the best performance be achieved. This was emphasized by Carr et al.[13] when Equation 5 and 6 were derived for the maximum number of theoretical plates, N_{max}, and maximum speed, t_0/N_{max}, that could be achieved while varying all three mentioned parameters for a given set of van Deemter coefficients and operating the maximum system pressure available, P_{max}.

Equation 5

$$N_{max} = \left[\frac{P_{max}\lambda t_0}{\Phi\eta}\right]^{1/2} \frac{1}{h_{min}}$$

Equation 6

$$\frac{t_0}{N_{max}} = \left[\frac{\Phi\eta t_0}{P_{max}\lambda}\right]^{1/2} h_{min}$$

where Φ equals a dimensionless flow resistance constant, η equals eluent viscosity, λ equals the ratio of interstitial porosity to total porosity of the packed bed, and h min is the value of the van Deemter minimum in reduced coordinates. The key to this relationship is that depending on the needs of the separation, maximum plate count can be sacrificed for a decreased analysis time.

1.4 Capillary Scale HPLC Columns

Another important factor to consider when designing a method for a given separation is the internal diameter of the column. The most commonly used chromatographic setup uses analytical scale columns, with internal diameters ranging from 4.6 – 2.1 mm. However, chromatographic columns are manufactured with internal diameters ranging from 4.6 mm down to 50 µm, trending toward more widespread miniaturization.[21] The main benefit to moving to smaller column diameters stems from the increase in concentration sensitivity.[22] Smaller column diameters achieve this by reducing radial dilution of an injected analyte band which in turn concentrates the sample band.[23, 24] This is expanded upon in Figure 1, which shows that as cross-sectional area of the column decreases with decreasing column diameter, the sample, depicted in red, is concentrated into a smaller area. The result of this is an increase in concentration proportional to the column radius squared. This relationship is very influential, as a switch from a 4.6 mm analytical scale column to a 75 µm capillary column would yield roughly a 3700-fold increase in signal for the same injection volume.

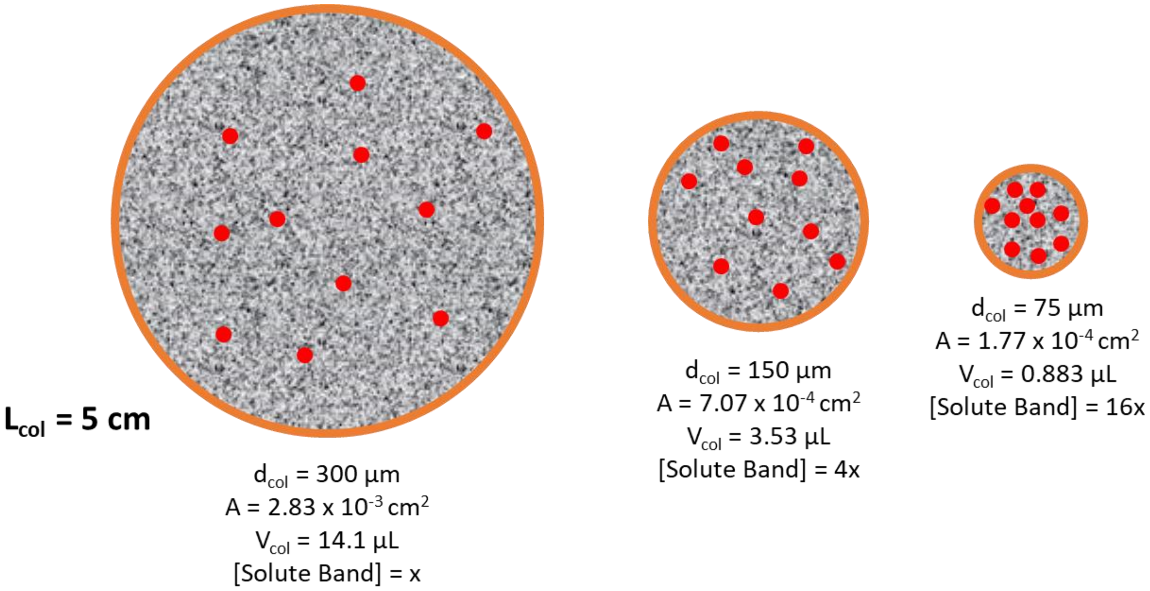

Figure 1. For a fixed column length of 5 cm and fixed solute band width, the concentration of the solute band increases by a factor of 4 for every reduction in column diameter by a factor of 2. This is because the cross-sectional area that the fixed length solute band occupies is decreased with decreasing diameter, reducing the volume for a given number of moles.

The sensitivity enhancement of column miniaturization will not result in an increase in peak height indefinitely. As the ratio of volume injected to total column fluid volume increases (Figure 2), the width of the solute band from injection becomes the major contributor band spreading.[25, 26] Thus, a linear increase in peak height with increasing injection volume is no longer observed, and the peak becomes broadened. This effect is known as volume overload.[27-32] As a general rule, the injected volume should not exceed 1% of the total column fluid volume in order to avoid these effects. This means in order execute an efficient separation with the 50 x 0.075 mm column described in the previous section, an injection volume of roughly 1 nL would be required. The hardware to introduce a sample this small does not currently exist, so the sensitivity enhancements must be restored by other means. These negative effects can be mitigated through solute focusing techniques, using temperature[33-46] or solvent strength[32, 47-50] to increase retention at the head of the column, to compress the solute band length and concentrate the solute on-column.

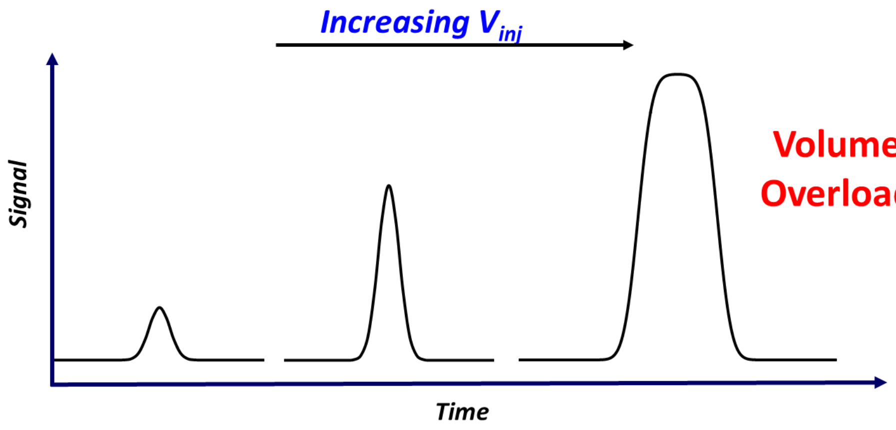

Figure 2. Example peak shape illustrating the broadening effects of volume overload. As V_{inj} increases, a linear increase in peak height is not maintained indefinitely, reaching a maximum signal height. Further increase to V_{inj} would not increase signal height and increase peak width. This effect worsens as V_{inj}/V_{col} increases and as the retention factor of the analyte upon injection decreases.

The sensitivity enhancement associated with capillary columns has led to their extensive incorporation studying biological applications. Methods requiring measurement of proteins[51-53], neuropeptides[54-56], and neurotransmitters[57, 58] regularly analyze low volume samples containing trace amounts of analyte. The low μL-nL flow rates associated with column miniaturization also couple extremely well to common mass spectrometry ionization sources such as electrospray ionization (ESI).[59, 60] The research throughout utilizes this sensitivity enhancement for *in vivo* neuroscience applications to study nM-pM concentrations of neurotransmitters and neuropeptides.

1.5 In vivo Sampling Methods

While capillary HPLC provides as excellent means of separation and detection of complex solute mixtures, improving sample collection technology is also important. This is especially true within the field of neurochemistry where basal extracellular concentrations of commonly studied analytes, including neurotransmitters and neuropeptides, often lie within the nano- to picomolar concentration range.[61] Sample handing must be minimized due to loss of solute mechanisms including adsorption and degradation following collection.[62] These challenges are further intensified by the desire for higher temporal resolution when studying mechanisms such as behavior where extracellular concentration changes happen on the second-to-minute timescale.

Push-pull perfusion (PPP), first development in 1961,[63] is an *in vivo* sampling method used to study the chemical composition of the extracellular environment.[64-69] Fluid flow through the tissue is controlled by implanting two capillaries into the desired brain region. A pump is connected to the perfusion capillary to induce pressure driven flow, while the collection capillary is connected to vacuum to collect the perfusion solution. Miniaturization of the capillaries over the years allowed for a reduction of perfusion flow rates. This reduced the injury caused by high flow rates and backpressure within the tissue[70-73] and allowed for near complete reuptake of the perfusion solution.[74] One major disadvantage is the challenge of connecting PPP directly to detectors for online analysis. The nL/min flow rates providing benefits for recovery and mitigation of tissue injury also yield very low collected sample volumes. The liquid internal channels of the capillaries are also exposed directly to the tissue. This means there is no barrier to prevent large molecules including proteins from entering the collection capillary leading to clogging and post collection hydrolysis of substrates.

Microdialysis (MD) is another widely used sampling technique within the neuroscience community as a means of investigating the extracellular space within the brain.[61, 75, 76] A semi-permeable membrane is implanted in the brain tissue, while a physiological buffer similar to the sampled environment is perfused through the interior. Analytes smaller than the molecular weight cutoff of the membrane will diffuse into the probe and be transported to the outlet tubing. Retrodialysis can also be implemented for localized delivery of drugs or substrates to the area surrounding the probe by adding these agents to the physiological buffer used to perfuse the probe. Dialysate can be collected and stored for later analysis or directly transported to a separation and detection method in a process known as online microdialysis. Chronic neurological diseases such as drug addiction[77] and schizophrenia[78] have been studied using microdialysis, along with monitoring small molecule metabolites including glucose and lactate to study traumatic brain injury.[79-83]

1.6 Scope of Work

The focus of this dissertation is the development and optimization of reversed-phase HPLC methods to be utilized for biological applications. The understanding of capillary scale temperature-assisted solute focusing has been expanded by developing new hardware which allows for multiplicative focusing of the solute band (Ch. 2). The new hardware includes 10 independently controlled thermoelectric cooling elements (TECs), programmed through LabVIEW, to modulate column temperature in three discrete focusing zones. Paraben standards were used for this work to illustrate the capabilities of the technique. The 10-TEC was able to enhance concentration sensitivity for a selected solute with conditions optimized *in silico* using Matlab scripts. In Chapter 3, we applied TASF to high-speed, *in vivo* separations of neurotransmitters. Again, Matlab scripts were utilized to predict retention and reduce method development time. Volume overload effects were mitigated in separations of serotonin (5-HT), yielding a method to enhance concentration sensitivity for this application. Multiplicative TASF was then performed using online microdialysis to develop a novel method for simultaneous *in vivo* dopamine and serotonin measurements with 1-minute temporal resolution for the first time.

Chapter 4 shifts the focus to studying sampling techniques for neurochemical applications. In this chapter, microdialysis probe integrity is investigated to determine if the steady glucose decline observed in traumatic brain injury model rats is correlated with microdialysis membrane failure. To do this, retrodialysis of a non-native, inert amino acid peptide was performed on day 1 and day 7 following implantation. A method for quantifying this peptide was developed using online derivatization through demethylation of the N-terminus and quantifying with capillary LC-MS/MS. It was found that the microdialysis probe was functioning properly for up to 7 days after probe implantation, validating that the loss of glucose observed in traumatic brain injury model rats had biological significance.

To conclude, Chapter 7 introduces a novel probe design for controlled tissue perfusion and collection within the brain to advance the previously developed electroosmotic perfusion-microdialysis (EOP-MD) work. In earlier iterations, a solid support with internal channels was manufactured using direct laser writing. A microdialysis probe could be epoxied in place, for a reproduceable sampling distance of roughly 200 µm. Tissue perfusion was controlled by electroosmotic flow with directional delivery to the microdialysis probe for continuous sampling. The device was redesigned to remove the microdialysis probe from the brain, and transport solutes from the extracellular space to an external reservoir containing the microdialysis probe. This device benefits from decreased time to steady state compared to previous models for improved data density for a given sampling period. The removal of the microdialysis probe from the tissue also mitigates the penetration injury associated with implantation with the new device reducing the implanted volume by nearly 90%. Finite element models were concurrently developed to determine the relationship with probe dimensions and collection, and to provide a method for determining important parameters such as tissue residence time needed for future work to study enzymatic activity quantitatively.

2.0 Multiplicative On-Column Solute Focusing Using Spatially Dependent Temperature Programming for Capillary HPLC

Reprinted with permission from Rerick, M. T.; Groskreutz, S. R.; Weber, S. G. Analytical Chemistry, **2019,** *91*, (4), 2854-2860. Copyright (2019) American Chemistry Society.

2.1 Introduction

The use of capillary columns in high-performance liquid chromatography has been advantageous when applied to the fields of metabolomics,[84-86] proteomics,[54, 87] and online monitoring of neurotransmitters.[88-90] The low analyte concentrations and nL – low μL sample volumes commonly encountered in these areas of study benefit from capillary scale separations because focusing of dilute solutes on-column is possible even with such small sample volumes.[91-93] However, there is a limitation to the degree of solvent focusing[94-96] when the ratio of the injected volume to the total column fluid volume (V_{inj}/V_{col}) is large and the k' of the analyte during injection is small. In this case, band broadening related to the injection becomes significant due to volume overload.[97] In these cases, the linear relationship between the volume of sample injected onto the column and the height of the signal is lost, because increasing sample volume only increases the width of the measured peak at a constant peak height. Further concentration of large volumes, or peak sharpening of these dilute samples on column would be desirable to increase signal-to-noise ratios, but this can be difficult to achieve with solvent alone, and of limited value for solutes that have poor retention even in aqueous solvents (when using reversed phases). One such application that uses very low concentrations of organic modifier is online, fast microdialysis separations of neurotransmitters.[98] For one-minute separations, sample volumes are on the order of 1 μL and target neurotransmitter concentrations are single-digit nM. These stringent time constraints also eliminate gradient elution as a means to focus due to the added time required for column re-equilibration for solvent to flow through the dwell volume. Therefore, there is a need for a methodology that will allow for multiplicative focusing to reverse the detrimental effects of volume overload without relying on solvent focusing alone for all applications benefitting from capillary scale separations.

Modulating column temperature to achieve focusing has proven to be a powerful tool when using capillary scale columns.[99-101] The low thermal mass of these columns means the internal column temperature equilibrates rapidly with the external temperature[102], reducing negative radial temperature gradient effects observed in larger column diameters.[103-105] Sample enrichment techniques using sub-ambient column temperatures have been explored by Greibrokk to improve separations of biological samples.[35, 36, 106-108] Spatially targeted temperature control for solute band focusing has been demonstrated both at the inlet[33] and outlet[109] of the column. Recently, the Nielsen group utilized spatial and temporal changes in column temperature to enhance the peak shape of several bovine serum albumin peptides.[110]

Previously, we have used temperature-assisted solute focusing (TASF)[46, 111-113] to apply sub-ambient column temperatures to the first 1-2 cm of the column during injection to induce focusing and reverse volume overload effects of the entire sample matrix. Simulations based on calculations of retention factors for the leading and trailing edges of an injected zone at each time-step during a solute zone's progress down the column using the Neue-Kuss equation[114] have provided not only a powerful screening method for separation conditions and temperature modulation timing but also a verification of experimental results. However, such simulations do not contain information about the shape of the eluted zone. In our previous work, we convoluted the rectangular zone defined by the two zone edges with a Gaussian profile defined by the accumulated increments of plate height as each edge traversed the column, $\Delta\sigma_l^2/\Delta x$, where the numerator is the increase in length-based variance and the denominator is the distance over which the increase occurs.

Here we simulate and demonstrate experimentally successive, on-column focusing of a test solute, ethyl paraben while not affecting a second solute. The improved simulation reflects experimentally observed, unusual peak shapes occurring when a temperature change is induced while the solute band resides within two temperature zones. The experimental control of temperature is achieved with a device consisting of a linear array of ten 1.0 x 1.0 cm thermoelectric cooling elements (TECs) capable of independently modulating column temperature.[100] Each step in the multiplicative focusing program works by creating conditions to make the trailing edge of a zone move faster than the leading edge for compression of the solute band. In order to demonstrate the flexibility of the active temperature control as well as the synergy gained from employing simulations, we have chosen a very simple mixture, ethyl- and *n*-propyl parabens (PB2 and PB3) to specifically evaluate the new TASF technology. We used the simulations for initial scouting of approximate suitable conditions to achieve the desired separation. These guided experiments to determine optimal timing of temperature changes to maximize PB2 focusing.

2.2 Theory

When a sample volume, V_{inj}, is injected, the leading edge of the solute band travels a distance L_{inj} which depends on the flow rate, F, mobile phase average velocity, u_{ave}, and retention factor during injection, k_{inj} (Eq.7 & 8).

Equation 7

$$u_{solute} = \frac{u_{ave}}{1 + k_{inj}}$$

Equation 8

$$L_{inj} = \left(\frac{V_{inj}}{F}\right)\frac{u_{ave}}{1 + k_{inj}} = t_{inj}\frac{u_{ave}}{1 + k_{inj}}$$

The length of the solute band contributes to the magnitude of band broadening and thus volume overload, an effect that worsens with long injection time and low analyte retention. To achieve an optimal sensitivity enhancement from focusing, the magnitude of L_{inj} should be such that it contributes only slightly, e.g., 5%, to the width of the eluted peak. With a fixed L_{inj}, focusing can be achieved by modifying the temperature at the head of the column during injection to increase k_{inj} while increasing V_{inj} proportionally. Typically, in reversed phase LC, the solute's partial molar retention enthalpy is negative in the absence of solute and buffer ionization effects. Therefore, decreasing the temperature at the head of the column leads to focusing. However, there are limitations to the minimum focusing temperature that can be used for a given separation. The lower limit of temperature for common reversed-phase studies is near -20 ºC due to mobile phase freezing point concerns[115]. A larger concern is temperature's effect on mobile phase viscosity.

Decreasing even a short 1 cm segment of the column to sub-ambient temperature results in significant increases in backpressure.

The ten-TEC TASF device solves this problem by allowing for longer initial (column head) focusing zones of variable length to permit larger injection volumes of more poorly retained analytes, while also allowing for multiple independent focusing stages. Thus, focusing can be achieved multiplicatively rather than in one single step, eliminating the need to focus at extremely low temperatures to achieve the same effect.

2.3 Experimental

2.3.1 Reagents and Chemicals

Uracil, ethylparaben (PB2), and n-propylparaben (PB3) were purchased from Sigma-Aldrich (St. Louis, MO). LC/MS grade acetonitrile, HPLC grade acetone, 99.9% HPLC grade 2-propanol, and HPLC grade phosphoric acid were purchased from Fisher Scientific (Fair Lawn, NJ). DI water was from an in-house Milli-Q Synthesis A10 purification system and was used without further treatment.

2.3.2 Column Preparation

Capillary columns used in all experiments were packed with Acquity BEH C_{18}, 1.7 µm particles (Waters Corp., Milford, MA) using 150 µm i.d., 360 µm o.d. fused silica capillaries

(Polymicro Technologies, Phoenix, AZ) as the column blank. Column frits were made by sintering 2 µm solid borosilicate spheres (Thermo Scientific, Fremont, CA) using an electrical arc into the end of a column blank. Particles were slurried in 2-propanol at a concentration of 65 mg/mL and sonicated for 20 minutes before packing using the downward slurry method. A Haskel model DSF-150 pneumatic amplification pump (Burbank, CA) was used to pack the column at 20,000 psi for 20 minutes using acetone as the packing solvent, before allowing the pressure to dissipate naturally. The remainder of the blank was then packed with 8 µm solid silica spheres (Thermo Scientific) for an additional 20 minutes at 20,000 psi before allowing the pressure to dissipate naturally. These were slurried at a concentration of 70 mg/mL in 50:50 (v/v) 2-propanol/water. This generates a column with two materials: 2.3 cm of silica spheres from the inlet to the leading edge of the first TEC, the "packed void" and 12.1 cm of C_{18} stationary phase beginning at end of the packed void. The column is fitted directly into the valve, so the packed void is used to ensure the stationary phase begins at the edge of the first TEC. The need for a packed void discussed previously[113] leads to variation in the length of stationary phase packing among columns. The length of the stationary phase packing material is dependent upon the mass of particles added to the packing apparatus since it is not possible to overfill a capillary and cut to the precise length. With careful consideration to slurry concentration and volume used, target lengths can reproducibly be achieved with roughly ± 1-2 cm of accuracy, but exact millimeter lengths of packing material must be measured after depressurization.

2.3.3 Chromatography

Stock solutions of 10 mM PB2 and PB3 were made in acetonitrile. A stock solution of 10 mM Uracil was made in Milli-Q water. Final dilutions of standard samples all contained 140 µM uracil and were made in mobile phase. The mobile phase was prepared by mixing an aqueous buffer (80% w/w) with acetonitrile (20% w/w). The aqueous buffer contained 10 mM H_3PO_4 to minimize ionization of free silanols on the stationary phase.

A Thermo/Dionex UltiMate 3000 Nano LC (NCS-3200RS, Germering, Germany) capillary pump was used to deliver mobile phase. The pump was connected to an externally mounted 6-port two-position Cheminert injection valve (C72x-669D, VICI Valco, Houston, TX) using a 750 x 0.100 mm nanoViper capillary. A second 750 x 0.100 mm nanoViper capillary was used as a 6000 nL sample loop. The packed void end of the column was placed directly into the valve and was cut to an appropriate length so the interface between the packed void and packing material lay at the edge of the TASF device. A flow rate of 2 µL/min was used for the length of the experiment. A Waters Acquity TUV fitted with a 10 nL nano flow cell (Waters Corporation, Milford, MA) was used for detection at 254 nm and was connected to the outlet of the column using a 350 x 0.025 mm i.d. x 0.360 mm o.d. fused silica capillary using PTFE unions. An Atlas analog-to-digital converter and Chromeleon version 6.8 software (Thermo) were used to acquire data at 100 Hz.

2.3.4 TASF Device

A diagram of the device used is shown in Figure 3. Hardware was similar to that used previously.[46] Ten 1.0 cm x 1.0 cm thermoelectric cooling elements (TECs) (Custom Thermoelectric, Part No. 04801-9G30-34RB, Bishopville, MD) labeled A - J from the column inlet made up an array of independently controlled temperature-based focusing segments. Each TEC was silver soldered to an individual 1 cm wide copper plate which were screwed onto a custom liquid-cooled copper heat sink fit into a polyvinylchloride housing. Each TEC was monitored with a 36-gage Type-T thermocouple (Omega Engineering, Stamford, CT) attached to the surface with epoxy and was connected to a National Instruments 9213 16-channel high speed thermocouple input module (Austin, TX). A Maxim Integrated 1968 electronic TEC driver (V_{max} = 5 V, I_{max} = ±3 A, Sunnyvale, CA) interfaced with a NI 9264 32-channel analog voltage out module was used to control individual TEC polarity.

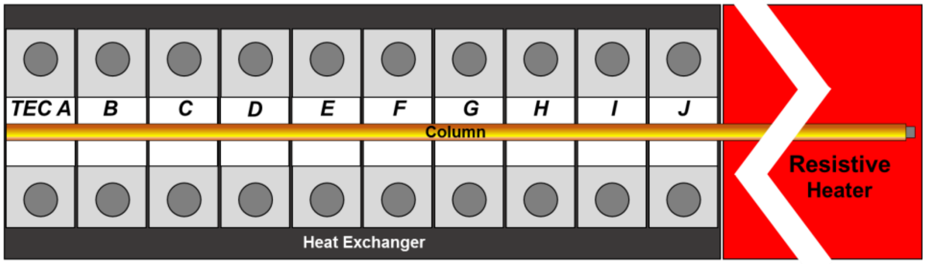

Figure 3. The 10-TEC device utilizes ten independently controlled TECs labeled A-J to control the temperature of the column. Each TEC is a 1.0 x 1.0 cm^2 Peltier device seen in previous versions. The column was fitted directly to the valve and a packed void was used to ensure the stationary phase packing started at the inlet end of the TEC A. Downstream of TEC J, a resistive heater is maintained at the separation temperaure.

A Thermo Haake K10 (Newington, NH) digital temperature controller pumped a mixture of ethylene glycol maintained at 25 ºC through the heat sink at 1 L/min. A Love Model 1500 proportional-integral-derivative (PID) controller (Dwyer Instruments, Michigan City, IN) controlled a Kapton resistive heater (KH-103-10-P, Omega) to maintain the isothermal portion of the device. LabVIEW programs (National Instruments) were written in-house to control the temperature of the TEC and to collect temperature profiles at 10 Hz. Control of the TEC polarity and injection valve was achieved through these programs using an NI 9403 digital I/O module. Remote start signals to interface the Chromeleon software was done using an NI USB-6008 DAQ.

2.3.5 Chromatography with TASF

Samples of 10 µM PB2 and PB3 containing 140 µM uracil (void marker) in mobile phase were introduced onto the 121 x 0.150 mm column with 4000 nL injection volumes at a flow rate of 2 µL/min. To ensure only thermal focusing was used to revert volume overload, the final sample solvent was mobile phase. Because the column is fitted directly into the valve, the solutes flow through a short 2.3 cm section of 8 µm borosilicate particles before reaching the C_{18} phase at the edge of TEC A as described above. Isothermal runs were first performed by holding all TECs and the resistive heater at 70 ºC. One-stage focusing runs were performed by cooling TECs A-D to 5 ºC for 30 seconds prior to injection and heating to separation temperature at staggered time points between 130 – 160 seconds in 10 second increments. During this time, TECs E-J and the resistive heater were held at 70 ºC. Two-stage focusing runs were performed by cooling TECs A-F to 5 ºC prior to injection. TECs A-D were heated to separation temperature at 140 s, and TECs E-F were heated to separation temperature at staggered time points between 190 – 210 seconds in 5 second increments. Three-stage focusing runs were performed by cooling TEC A-G to 5 ºC prior to injection. TECs A-D were heated to separation temperature at 140 s, and TECs E-F were heated to separation temperature at 200 s. TEC G was heated to separation temperature at staggered time points between 205 – 260 seconds in 5 second increments. All runs were performed in duplicate, except runs at optimal focusing times which were performed in triplicate. All runs utilized the same chromatographic conditions, varying only in the timing of temperature changes.

2.4 Results and Discussion

2.4.1 Technical Improvements to TASF Instrumentation

The addition of more TECs necessitates expansion of the LabVIEW software since each TEC is controlled individually. Control of individual TEC temperature is maintained by an algorithm in LabVIEW. Previous programs using simple feedback loops were capable of 10.4 ºC/s temperature changes. In the current device, PID control was implemented to achieve faster step changes in temperature of up to 40 ºC/s with optimal tuning. The LabVIEW program can alter the temperature of the individual TECs to conform with any sequence of temperatures/times.

2.4.2 Simulations

We have previously[46] simulated isocratic "peaks" by tracking only the leading and trailing edges of chromatographic zones and convolving[116] the rectangular zone shape at the end of the column with a Gaussian profile accurately reflecting the dynamics of the chromatography. Here each injected band is separated into ten equal-width, adjacent bands. Individual concentration profiles were generated for each segment as described above and then summed for a total concentration profile of the entire injected band. In the previous and current simulations, retention factors are calculated using the Neue-Kuss equation, Eq. 9 the four parameters having been previously determined by least-squares regression on retention data (Table 3 in supplemental information). At each time step (0.1 s) in the simulation the local solute velocity based on the local k value yields the distance each of the 11 edges travels, Δz, for a given time step. The local contribution to the plate height (Δh) in that step, $\Delta\sigma^2/\Delta z$, is determined from a dimensionless van

Deemter equation with the diffusion coefficient calculated for the local, temperature-dependent solvent viscosity. The sum of the values of Δh define the column contribution to the peak variance while the distance between the leading and trailing edges defines the contribution of the injection profile to the peak variance.

Equation 9

$$\ln(k) = \ln(k_{0,T}) + \frac{D}{T} + 2\ln(1+ac) - (1+\frac{D}{T})\frac{B_T c}{1+ac}$$

The following simulations incorporated experimentally determined values of extracolumn volume and the packed void on the column. A 4000 nL injection volume of an unretained marker, PB2 and PB3 was introduced onto the column, and three focusing zones were used to selectively focus PB2 using seven 1.0 x 1.0 cm segments corresponding to TECs A-G. A schematic of temperature programming and solute band compression is shown in Figure 4.

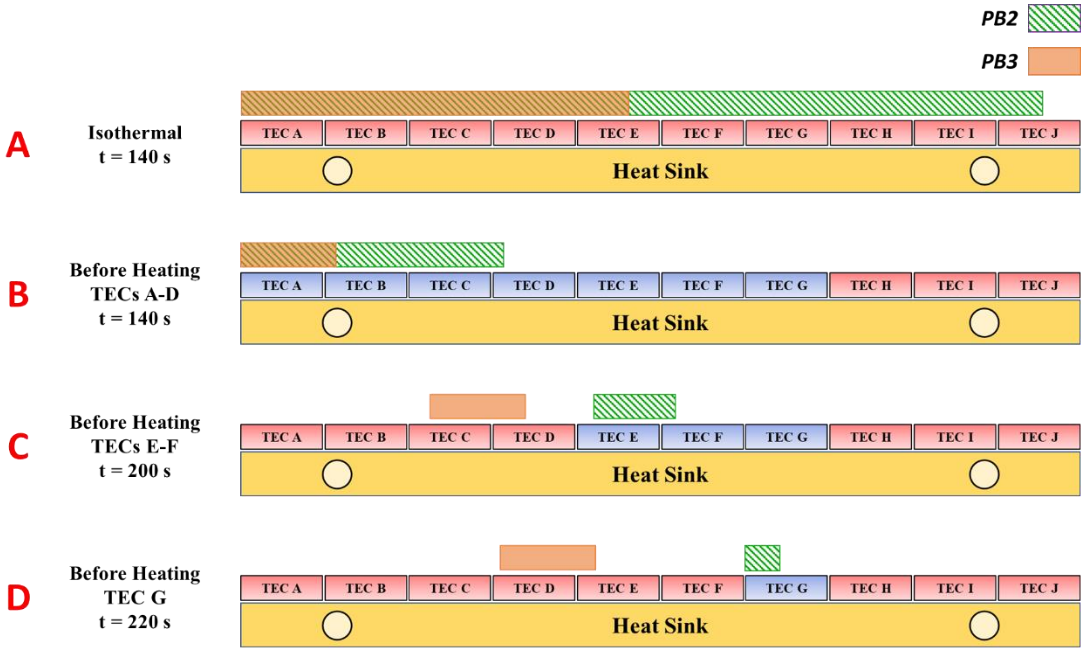

Figure 4. Visual representation of the PB2 (green diagonal) and PB3 (orange) solute bands during the 4-2-1 focusing experiment. Bands that appear orange with stripes illustrate both bands occupying the same portion

of the column. An injection time of 120 s is illustrated. Timing of step increase in temperature correspond to the optimum focusing times found experimentally to yield the largest peak height for PB2. The solute zone widths (A) at 140 s under 70 °C isothermal conditions, (B) immediately before heating TECs A-D from 5 to 70 °C at 140 s, (C) immediately before heating TECs E-F from 5 to 70 °C at 200 s, and (D) immediately before heating TEC G from 5 to 70 °C at 220 s. Each focusing time was then delayed by 24 s to account for the experimentally determined pre-column dead volume to calculate the true effective focusing time to best match the experimental results. The PB2 solute band undergoes three stages of compression in each cooled zone, while no compression is observed for PB3 after 140 s under TASF conditions.

To illustrate the extent of our control over the focusing process, we sought to create a narrow zone for PB2 and only PB2, with the PB3 band only experiencing band compression during the initial focusing stage. The simulated chromatograms under isothermal, one-, two-, and three-stage focusing conditions are shown in Figure 5. Peak heights and enhancement factors relative to isothermal peak heights are shown in Table 1 for PB2. Under isothermal conditions, the PB2 solute band displays a wide “peak” due to volume overload. One stage of focusing reduces the zone width, but the width is unacceptable. Each subsequent focusing step simulated further compresses the solute band, enhancing the maximum signal observed ultimately predicting a 27-fold increase in peak height. Following the initial stage of compression, PB3 retention time and peak shape are unaffected by the subsequent focusing stages targeting PB2 further down the column.

Table 1. Simulated enhancement of peak height through multiplicative focusing of PB2 under each focusing condition.

Conditions	Peak Height	(Peak Height) / (Peak Height)$_{iso}$
Isothermal	0.10	1.0
One-Stage	0.31	3.1
Two-Stage	0.95	9.5
Three Stage	2.68	27

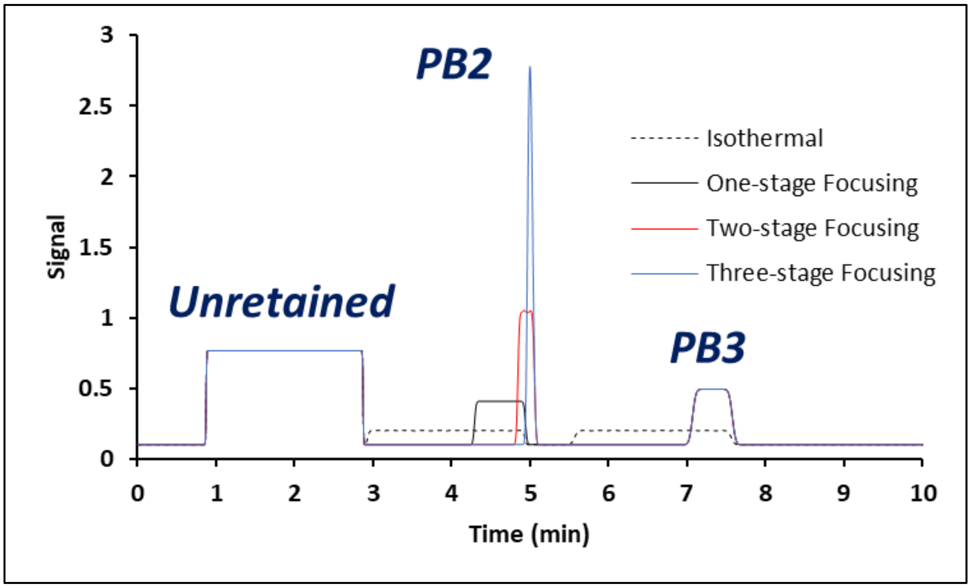

Figure 5. **Simulated chromatograms for isothermal, one-, two-, and three-stage focusing of an unretained marker, PB2, and PB3. The focusing times for each stage where the zones change from 5 °C to 70 °C were 140, 200, and 220 s. The PB2 peak is enhanced with each zone for a 27-fold increase in signal when compared to the isothermal run and is selectively focused from PB3 after the first stage. Selectivity for PB2 focusing is demonstrated by PB3 retention time and peak shape remaining constant after the initial focusing stage. Column: 121 x 0.150 mm with Acquity BEH C18 1.7 µm particles, mobile phase 20/80 (w/w%) acetonitrile/10 mM H_3PO_4. Flow rate was set to 2 µL/min.**

In experimental work we have observed odd peak shapes during TASF optimization especially when optimizing the third switching time. The odd shapes occur when the temperature changes while a solute zone is in two adjacent TASF zones. The simulated concentration profiles for a range of switching times for the third zone from t = 215-280 s are shown in Figure 6 for PB2. At 210 s, the PB2 solute band has not yet reached the cooled zone, so the observed peak is similar to what is observed for two-stage focusing only. The leading edge of the solute band passes into the third focusing zone starting at 215 s. For switching times in the range of 225-245 s the solute zone is mostly or completely within the confines of the seventh TEC before switching. From that point, peak height decreases as the leading edge starts to elute from the third focusing zone before the temperature step is initiated. By 260 s, the entire solute band has left the focusing zone before the step change occurs, resulting in a peak that once again matches the two-stage focusing signal. Figure 9 in the supplemental information demonstrates how these variations in peak shape are generated using discretized injected zones.

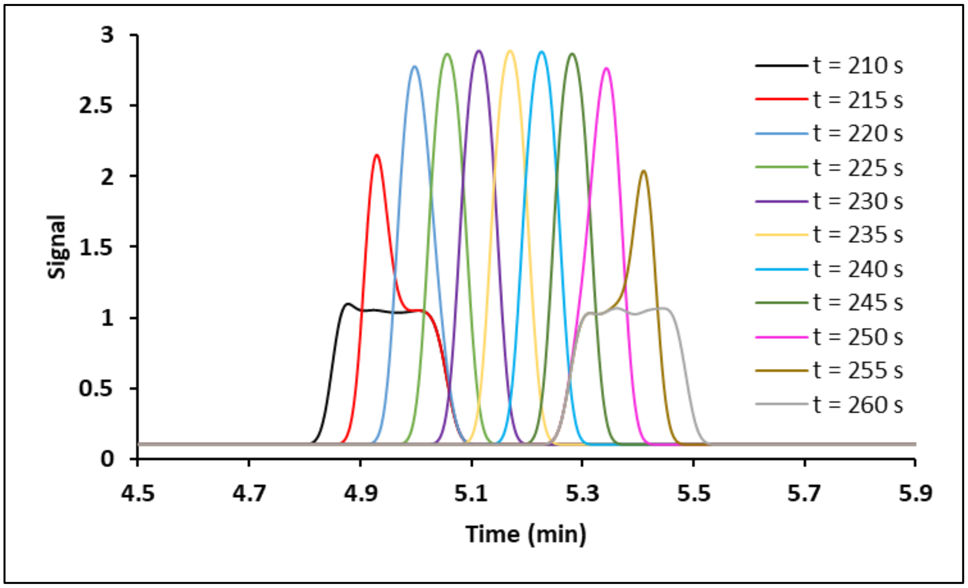

Figure 6. The simulated optimization profile of PB2 for staggered changes in temperature for three-stage focusing. Each profile's color corresponds to a time listed on the right. These times are when TEC G undergoes a step change in temperature from 5 to 70 °C. For all traces, the step changes in temperature for TECs A-D and E-F occurred at 140 and 200 s respectively. Chromatographic conditions were identical to those stated in Figure 5.

2.4.3 Experimental Three-Stage Focusing

Based on the results of preliminary simulations, we studied the peak heights and enhancement factors relative to isothermal peak heights experimentally. The isothermal run shown in Figure 7A displays the characteristic plateaued peak shape predicted by the simulations. Focusing time optimization for one-, two-, and three-stage focusing is shown in Figure 7B-D for PB2. For the first two stages, small variations in these focusing times did not have a dramatic impact on peak shape. Because of this, optimal timing was chosen to be 10 s after the entire solute band entered the focusing zone. The timing of events at the third stage is more critical. During the third stage of focusing, the peak demonstrates a spectrum of shapes, with a maximum height and sharpness (shown at 220 s). Figure 11 in the SI demonstrates the correlation between observed peak height and the FWHM.

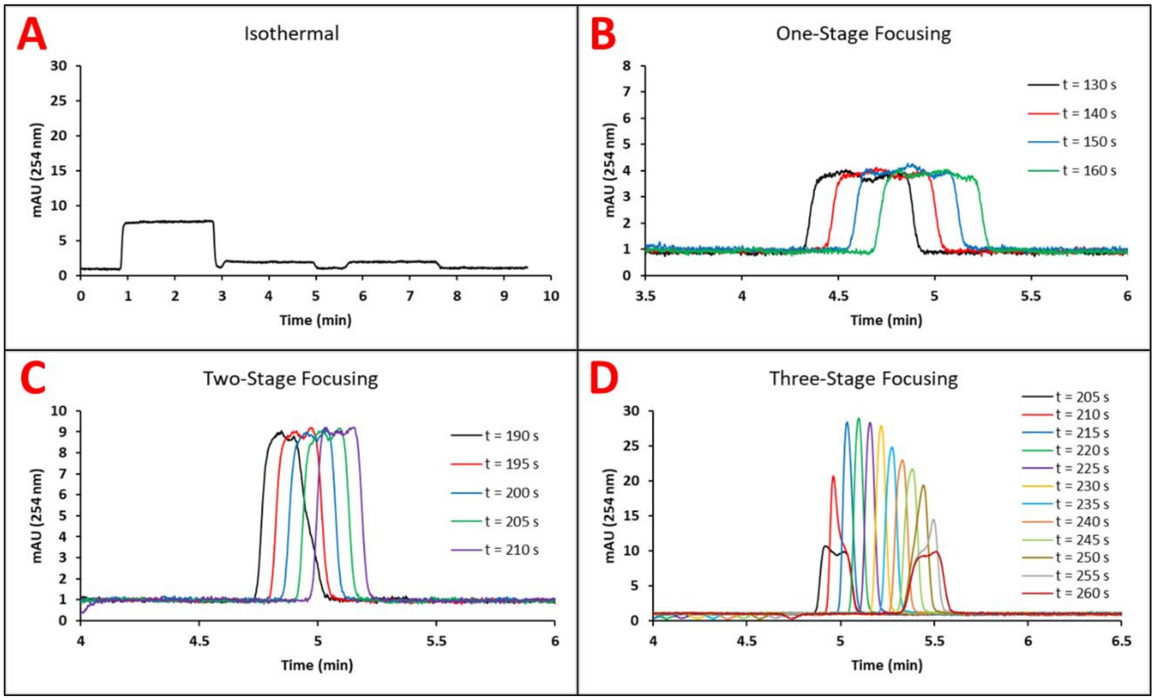

Figure 7. **The isothermal run (A) of uracil, PB2, and PB3 standards displays characteristic table-top volume overload peaks at an injection volume of 4000 nL. Focusing time optimization was performed on PB2 for one-stage (B), two-stage**

(C), and three-stage focusing (D) and times were chosen based on maximum signal. Column: 121 x 0.150 mm with Acquity BEH C18 1.7 µm particles, mobile phase 20/80 (w/w%) acetonitrile/10 mM H_3PO_4. Flow rate was set to 2 µL/min. Focusing temperature and separation temperatures were 5 °C and 70 °C.

Table 2. Enhancement of peak height through multiplicative focusing of PB2 under each focusing condition.

Conditions	Peak Height	(Peak Height) / (Peak Height)$_{iso}$
Isothermal	1.37	1.00
One-Stage	3.24	2.36
Two-Stage	8.15	5.95
Three Stage	28.00	20.4

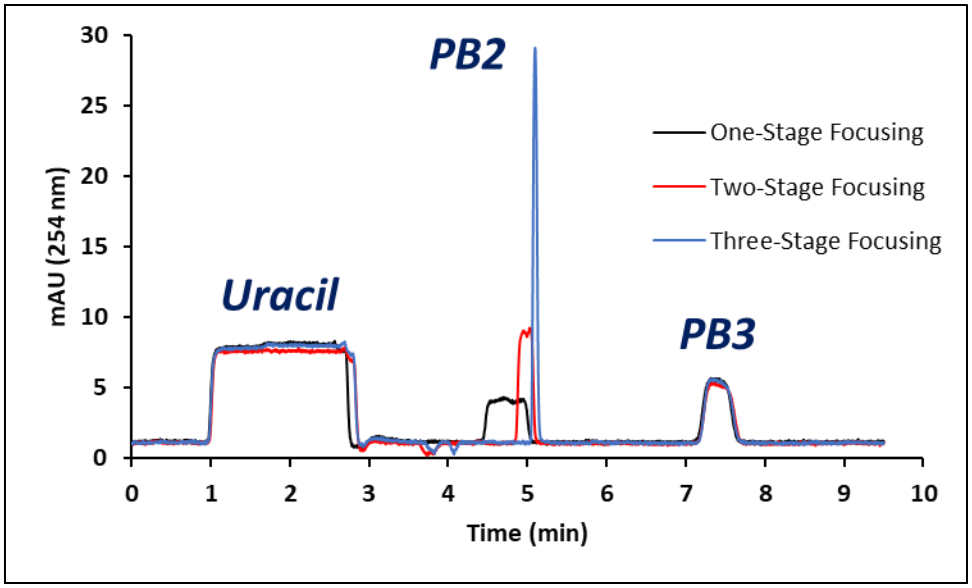

Figure 8. Overlay of one- (black), two- (red), and three-stage (blue) focusing of uracil, PB2 and PB3. The PB2 peak undergoes peak height enhancement at each stage for a 20.4-fold increase when comparing three-stage focusing to isothermal runs. Selectivity for PB2 focusing is demonstrated by PB3 retention time and peak

shape remaining constant after the initial focusing stage. All chromatographic conditions were identical to Figure 7.

The chromatograms under the optimal focusing times are overlaid in Figure 8 for one- (black), two- (red), and three-stage (blue) focusing. Broadly speaking, the experimental results are in good agreement with the simulations. There is an asymmetry in the experimental results that is not in the simulation. This is most clearly seen as the experimental peaks decrease in height and increase in width at the long-time end of the series while the simulated peaks do not. Also, see Table 2 the maximum peak height enhancement was roughly 25% lower than predicted by the experiments. This is likely caused by post-column band broadening which is not accounted for in the simulations (N.B. the post column volume's contribution to the observed retention time is, however, accounted for.) Despite the complexity of the chromatographic process, the simulation adequately represents the peak shapes.

The results provide evidence that this device can successfully execute the complex temperature programming timing required to both selectively focus one solute within a mixture, and to focus the solute in multiple compression events. The PB2 peak height was enhanced by a factor of 20.4. To achieve this result in a single compression step would require cooling to -58 °C, hypothetically by extrapolating the Neue-Kuss equation for PB2. PB3 retention is not affected after the first stage of focusing. This displays selectivity in the approach and the opportunity to increase throughput of a desired separation through focusing solutes with low retention negatively affected by volume overload while maintaining the fastest elution time possible for highly retained compounds.

This methodology displays high run-to-run reproducibility even with the complex and precise temperature programming involved. Variability by even a few seconds in the timing of temperature changes can shift retention time and change observed peak heights as observed in Figure 7. An overlay of three runs using the fully optimized three-stage focusing conditions is shown in Figure 12 in the SI. The standard deviation of the retention time was 0.005 min and for the peak height was 0.32 mAU (n=3) for ethyl paraben. It is worth noting that the focusing times were randomized during the optimization, so these runs displayed are not back-to-back injections. This further emphasizes the high level of control both in maintaining column temperature and the timing of the temperature changes using this improved instrumentation.

2.5 Conclusions

Summarizing, the improvements in both TASF hardware and simulations allow us to achieve selective, multiplicative focusing of a solute which would be unachievable with traditional solvent-based focusing or single stage TASF. While we have demonstrated this with the simple paraben mixture, the retention times and extent of focusing of any retained solutes can be manipulated with this flexible technique by adjusting the number of focusing zones and the timing of the temperature changes to suit the desired goals. The simulations provide a fast screening method for viable conditions for the desired separation. The effectiveness of this method has been validated by a significant correlation between the simulations and experimental results. These results establish the next step forward in on-column temperature-based solute focusing, providing a broader scope of applications for this technology.

It must be re-stated that, if the timing of the temperature changes is not optimal, broad peaks can occur. Thus, the procedure described here is more suited to simple chromatograms than complex ones, and perhaps for complex mixtures where a limited number of analytes is of interest. While instrumental limitations would ultimately affect the accuracy of the control of dozens of smaller TECs, one can easily envision more complex temperature programs and more, smaller TECs to accomplish both focusing and selective improvement of resolution of components of a mixture.

2.6 Supporting Information for Multiplicative On-Column Solute Focusing Using Spatially Dependent Temperature Programming for Capillary HPLC

Table 3. Neue-Kuss parameters for PB2 and PB3 used to calculate retention with varying temperature and mobile phase composition.

	$\ln k_{0,T}$	B_T	a	D
Ethyl paraben	4.30	2.64	1.99	3271
Propyl paraben	4.24	2.70	2.03	3774

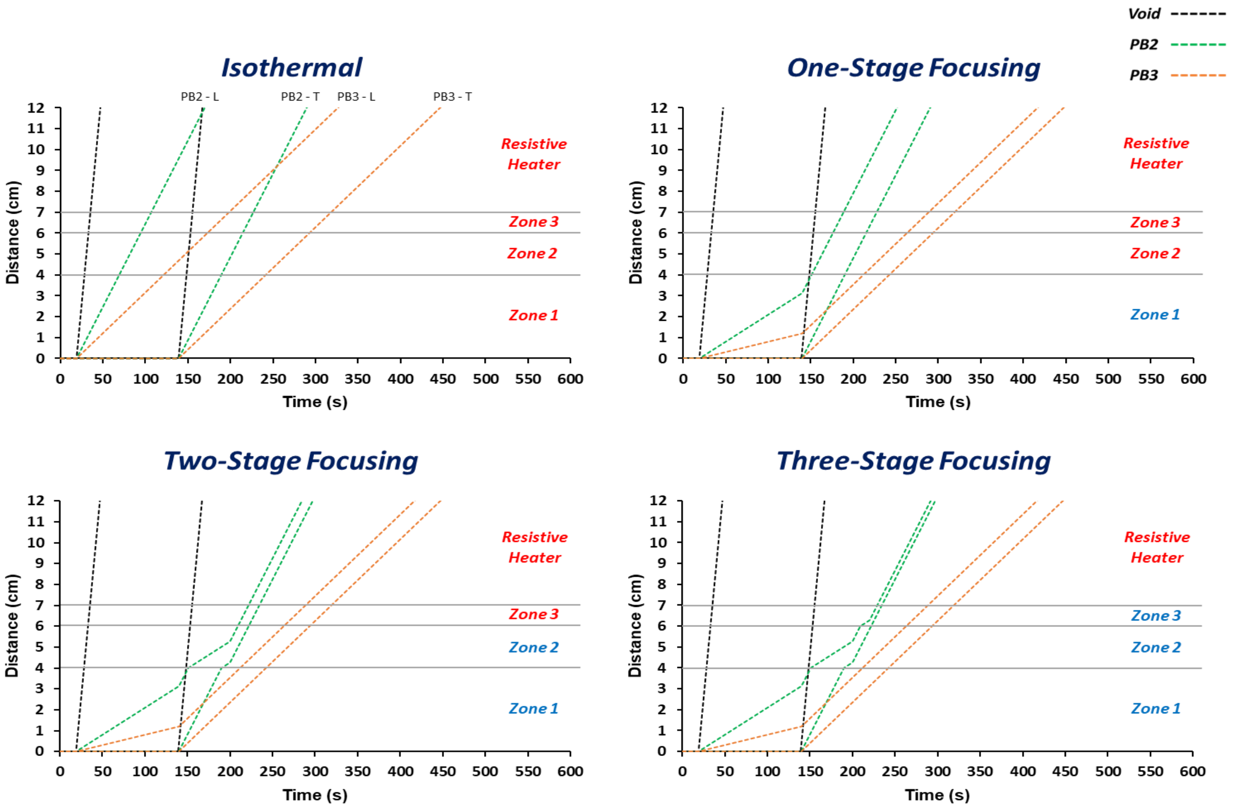

Figure 9. The velocity profiles of an unretained void marker (black), PB2 (green), and PB3 (orange) under isothermal, one-, two-, and three-stage focusing conditions. The distance the leading (L) and trailing (T) ends of each solute band have traveled are tracked under each condition and plotted against the separation time. The distance between the leading and trailing ends represent the physical width of the solute band on-column, while the slopes indicate the band velocity. A step change in temperature fom 5 to 70 °C occurs at 140, 200, and 220 s for zone 1, 2, and 3 respectively.

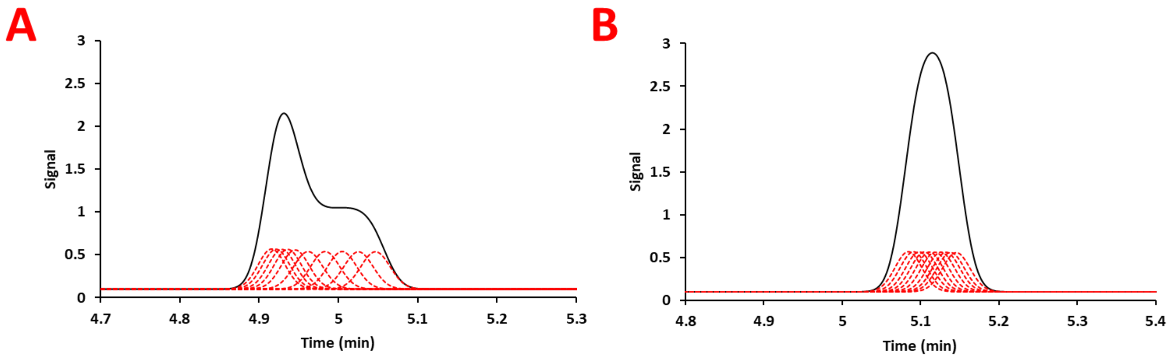

Figure 10. Peak generation is shown using the discretized peak method for nonoptimal (A, t = 215 s) and an optimal (B, t = 230 s) focusing time. Red traces correspond to 10 individual observed concentration profiles of the PB2 solute band, staggered in time by $t_{inj}/10$. These concentration profiles are summed to generate the total concentration profile shown in black.

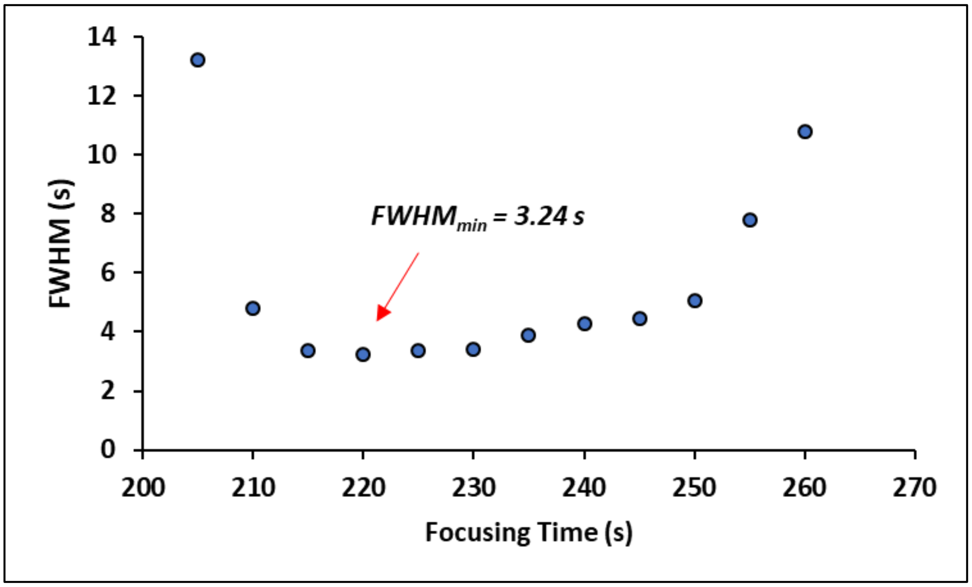

Figure 11. The experimental FWHM measurements as a function of focusing time to determine the optimum temperature programming conditions for the three-stage focusing of PB2. Timing corresponds to when TEC G was programmed for a step increase to the separation temperature. The focusing time yielding the highest peak height (220 s) also exhibits the smallest FWHM value.

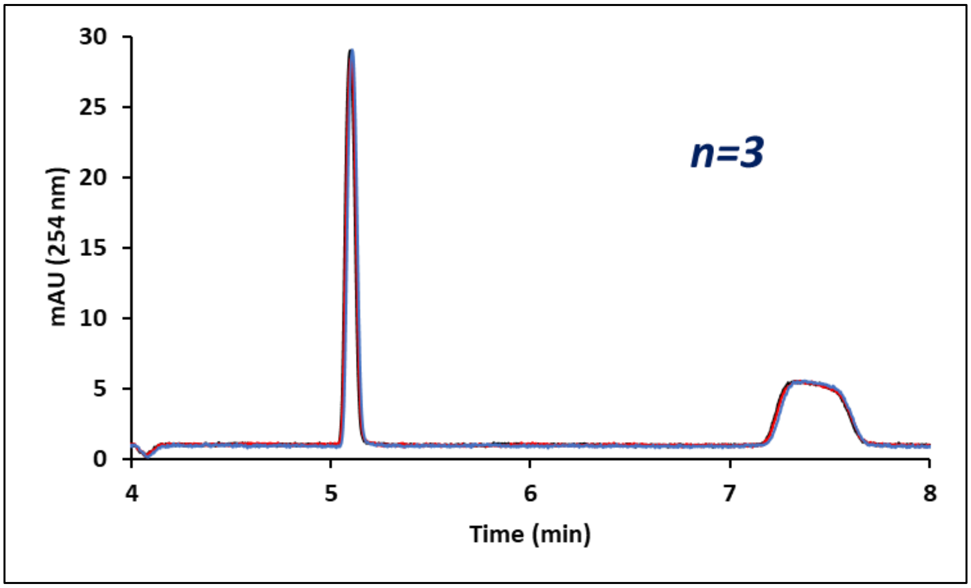

Figure 12. Overlay of optimized three-stage focusing runs. High reproducibility is observed for both the PB2 and PB3 peaks demonstrating tight control of TEC temperature and timing of step increases at each stage.

3.0 Applying Temperature-Assisted Solute Focusing to High-Speed Separations of Monoamine Neurotransmitters

3.1 Introduction

Monoamine neurotransmitters including dopamine (DA) and serotonin (5-HT) are small molecules capable of influencing physiology within the brain.[117-120] This is primarily controlled through release and reuptake mechanisms from neurons regulating their concentration within the extracellular space.[121] Dysregulation of these mechanisms can lead to neurological diseases including anxiety[122], Parkinson's disease[123], and obsessive compulsive disorder (OCD)[124-126]. Therefore, it is important to accurately quantify these concentrations simultaneously within the extracellular space to improve the understanding of these processes and develop means of treatment. Monitoring neurotransmitter concentration over the course of days or weeks is suitable for studying chronic conditions, but extracellular neurotransmitter concentrations affect behavioral decision making on the timescale of seconds to minutes.[127, 128] Therefore, high temporal resolution is needed to elucidate information regarding the link between chemical neurotransmission and behavior.

In recent years, measurements of neurochemical concentrations have been executed using fast-scan cyclic voltammetry (FSCV)[129-131] or microdialysis coupled high-performance liquid chromatography. FSCV has significant advantages when using volume limited samples with exceptional temporal resolution down to sub-second measurements. However, its lack of chemical selectivity makes simultaneously monitoring multiple analytes challenging, and it suffers from an inability to monitor basal concentrations. Microdialysis is capable of monitoring basal concentrations of multiple extracellular species at once.[61, 75, 132] This is highly desirable capability when studying neurological conditions involving complex regulatory pathways. While multiplexing has been demonstrated[133], these techniques have been limited to offline measurements and a loss of temporal resolution when compared to FSCV with minute timescale separations times[134-139]. While improvements to microdialysis technology could be beneficial, the major challenges resulting in a loss of temporal resolution are separations based.

In online microdialysis coupled HPLC, the temporal resolution dictates both the total separation time and the total time allowed to deliver sample to the system for each injection. These factors lead to the core complications with decreasing temporal resolution: 1) generating enough theoretical plates to separate the sample's critical pair of solutes, and 2) delivering enough sample to the system to yield a signal above the detection limits. As described in Section 1.3, lower separation time often comes at the cost of less efficiency. When targeting a sub-minute separation of DA and 5-HT, conditions to elute the latter within the time constraints cause the former to elute within a high intensity, early eluting interference peak. To address detection limit concerns, concentration sensitivity can be enhanced by decreasing the internal diameter of the columns, an approach that has led to capillary columns becoming widely used within the neuroscience community. However, as discussed in Section 1.4, volume overload effects introduce a limit to the total enhancement available without solute focusing, causing further degradation of the earlier eluting DA signal.

Mitigating volume overload effects when studying DA and 5-HT is challenging because these solutes are poorly retained on reversed-phase columns. To mitigate this, the adoption surfactant addition to the mobile phase has become a common practice to bolster retention through ion pairing.[140] When an anionic surfactant is added to the mobile phase when using RP-LC

columns, hydrophobic interactions between the alkane chains will "coat" the stationary phase in the added surfactant. Mobile phase pH conditions and buffers are chosen to protonate neurotransmitter amine groups, which increase retention through charge interaction with the negatively charged sulfonate groups of the surfactant. Despite this, it is not uncommon for neurotransmitters to have a k' < 10 even at nearly 100% aqueous mobile phase conditions.
Under these conditions, solvent focusing used commonly in HPLC is not a viable avenue for increasing separation efficiency, and retention must be manipulated by other means.

Temperature-assisted solute focusing (TASF) is perfectly suited for this particular application. Due to the low thermal mass of capillary scale columns, temperature changes of up to 80 °C occur within seconds.[141] This provides the capability to utilize multiple focusing zones to optimize a given high-speed separation. Our lab has previously demonstrated the ability to utilize multiplicative focusing through sequential sub-ambient temperature changes at the head of the column using parabens.[45, 46] In this work, we first demonstrate the ability to apply multiplicative TASF techniques to fast neurotransmitter separations. This was done by first executing two-stage focusing on 5-HT in aCSF. This initial work provided validation that TASF was capable of mitigating volume overload for neurotransmitters and provided validation for the Matlab scripts used for method optimization. To expand upon this work, multiplicative TASF was then applied to 1-minute separations of both DA and 5-HT both *in vitro* and *in vivo*. To our knowledge, this is the first time this had been achieved for these two solutes.

3.2 Experimental

3.2.1 Reagents and Chemicals

Sodium acetate and glacial acetic acid were purchased from J. T Baker (Phillipsburg, NJ). Serotonin hydrochloride (5-HT), dopamine hydrochloride (DA), nomifensine maleate salt, L-ascorbic acid (AA), and sodium 1-octanesulfonate (SOS) were purchased from Sigma-Aldrich (St. Louis, MO). LC/MS grade acetonitrile, HPLC grade acetone, 99.9% HPLC grade 2-propanol were purchased from Fisher Scientific (New Brunswick, NJ). Artificial cerebrospinal fluid (aCSF) was 142 mM NaCl, 1.2 mM $CaCl_2$, 2.7 mM KCl, 1.0 mM $MgCl_2$, 2.0 mM NaH_2PO_4, pH 7.4. DI water was from an in-house Milli-Q Synthesis A10 purification system and was used without further treatment.

3.2.2 Column Preparation

The method for making frits for the column blanks was followed the procedure outlined by Kennedy[142]. A 25% (v/v) solution of formamide and Milli-Q water was diluted 1:1 with potassium silicate. A 10 µL drop was then placed on a piece of Watman filter paper (Cat No. 1822-025). The end of the column blank was pressed against the wet section of the filter paper and twisted to leave a hole twice for each column blank. They were then placed in an oven Thermo Focus series GC oven set to 85 ºC for 12 hours. The Acquity BEH C_{18}, 1.7 µm particles (Waters, Milford, MA) were slurried in 2-propanol at concentrations of 65 mg/mL and 40 mg/mL for the 150 and 75 µm i.d. column blanks respectively. This was sonicated for 20 minutes before packing using the downward slurry method. A Haskel model DSF-150 pneumatic amplification pump (Burbank, CA) was used to pack the column at 20,000 psi for 20 minutes using acetone as the packing solvent, before allowing the pressure to dissipate naturally. 8 µm solid silica spheres (Thermo Scientific) were slurried at a concentration of 70 mg/mL in 50:50 (v/v) 2-propanol/water, and were used to pack the remainder of the column blank. After loading the silica sphere slurry, the column was pressurized for an additional 20 minutes at 20,000 psi before allowing the pressure to dissipate naturally.

3.2.3 Chromatography

3.2.3.1 Two-Stage Focusing of 5-HT

Stock solutions of 10 mM 5-HT and AA were prepared in aCSF containing 20 mM HOAc. Subsequent dilutions were made in this solution with final dilutions made in aCSF. All final 5-HT standards contained 25 µM AA. Mobile phase was prepared by mixing an aqueous buffer (92% w/w) with acetonitrile (8% w/w). The aqueous buffer contained 50 mM sodium acetate, 10 mM SOS, and 0.15 mM disodium EDTA. Acetic acid was used to adjust the pH to a value of 5 using a Fisher Acumet 10 pH meter. Prior to use, the mobile phase was degassed and filtered twice through 0.45 µm nylon membrane filters (Millipore).

A Thermo/Dionex UltiMate 3000 Nano LC (NCS-3200RS, Germering, Germany) was used. The outlet of the pump was connected to a Cheminert injection valve with a 750 x 0.100 mm nanoViper capillary. A second 127 x 0.100 mm nanoViper capillary was used as a 1000 nL sample loop. The packed void end of the column was placed directly into the valve, and was cut to an appropriate length so the interface between the packed void and packing material lay at the edge of the TASF device. A flow rate of 1.6 and 6.4 µL/min was used for the length of the experiment for the 75 and 150 µm columns respectively. The outlet of the capillary column was connected to BASi radial-style electrochemical detection flow cell by a 10 cm, 25 µm i.d. capillary. Analytes were detected at 700 mV versus a Ag/AgCl reference electrode (3 M NaCl), using a 3 mm glassy carbon electrode with a 25 µm thick gasket. Potential control was achieved using a BASi LC-4C potentiostat with a 1.0 Hz low-pass filter. An Atlas analog-to-digital converter and Chromeleon version 6.8 software (Thermo) was used to acquire data at 100 Hz.

3.2.3.2 One-Minute Separations of DA and 5-HT

Stock solutions of 10 mM 5-HT, DA, and AA were prepared in aCSF containing 50 µM AA. All dilutions maintained the sample matrix for subsequent dilutions. Mobile phase was prepared by mixing an aqueous buffer (96% w/w) with acetonitrile (4% w/w). The aqueous buffer contained 50 mM sodium acetate, 10 mM SOS, and 0.15 mM disodium EDTA. Acetic acid was used to adjust the pH to a value of 5 using a Fisher Acumet 10 pH meter. Prior to use, the mobile phase was degassed and filtered twice through 0.45 µm nylon membrane filters (Millipore).

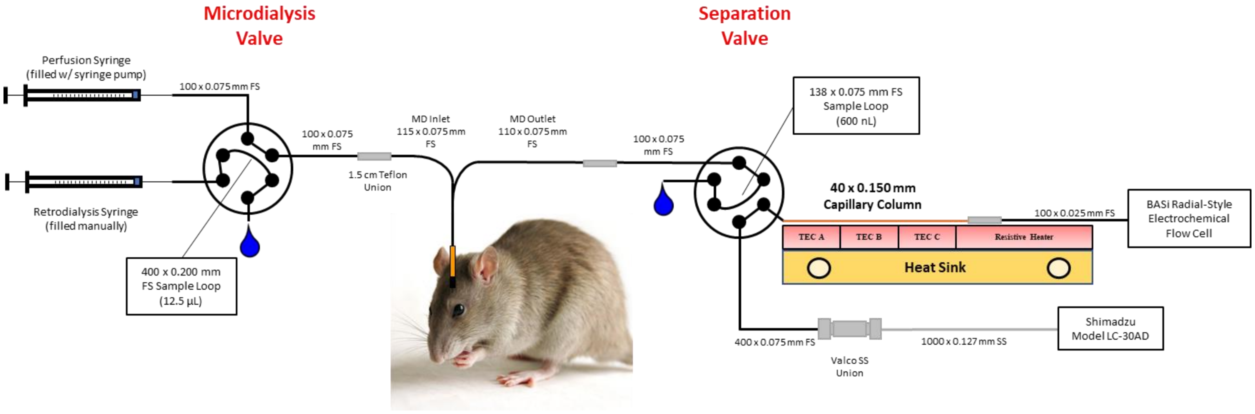

Figure 13. A schematic of the *in vivo* instrumentation used. A two-valve configuration is used including a separation valve which controls the timed injections and a microdialysis valve which switches positions during K$^+$ or nomifensine stimulations. The perfusion syringe is operated by a syringe pump and delivers a constant 0.6 µL/min flow rate, while the sample loop of the microdialysis valve is filled manually with the

retrodialysis syringe. The 40 x 0.150 mm column is connected directly to the valve and rests on the 3-TEC TASF device. The column is connected directly to the BASi flow cell using a 1.5 cm Teflon union.

A detailed schematic of the instrumentation is shown in Figure 13. For *in vitro* experiments the microdialysis probe inlet and outlets were removed from the Teflon unions and connected with a 350 x 0.075 mm fused silica capillary. A Shimadzu Model LC-30AD (Canby, Oregon) pump was used. The outlet of the pump was connected to 1.0 m of 0.005" i.d. stainless steel tubing, and connected to the valve with a union (Vici Valco), and a 400 x 0.075 i.d. x 0.360 mm o.d. fused silica capillary. For the separation valve, a 138 x 0.075 i.d. x 360 mm o.d. fused silica capillary was cut in-house and used as the sample loop with an internal volume of 600 nL. For the microdialysis valve, a 400 x 0.200 i.d. x 0.360 mm o.d. fused silica capillary was made to be used as the stimulation sample loop with an internal volume of 12.5 µL. The packed void end of the column was placed directly into the valve, and was cut to an appropriate length so the interface between the packed void and packing material lay at the edge of the TASF device. Constant pressure controls were implemented into the LabVIEW programming which changed the flow rate of the Shimadzu pump between 16 and 10 µL/min for separation and focusing conditions respectively. For the K^+ and nomifensine stimulations, the microdialysis valve switched positions to introduce the manually loaded stimulation solution into the flow path of the microdialysis probe. The outlet of the capillary column was connected by a 10 cm, 25 µm i.d. capillary to BASi radial-style electrochemical detection flow cell. Analytes were detected at 450 mV versus a Ag/AgCl reference electrode (3 M NaCl), using a 3 mm glassy carbon electrode with a 25 µm thick gasket. Potential control was done by BASi LC-4C operating with a 1.0 Hz low pass filter. Data acquisition at 50 Hz was controlled by a PeakSimple Model 333.

3.2.4 TASF Device

A diagram of the device used is shown in Figure 14. Hardware was similar to that described in Section 2.3.4. Three 1.0 cm x 1.0 cm TECs labeled TEC A, B, and C made up an array of independently controlled temperature-based focusing segments. Care was taken to minimize the distance between the edges of the TECs below 100 µm.

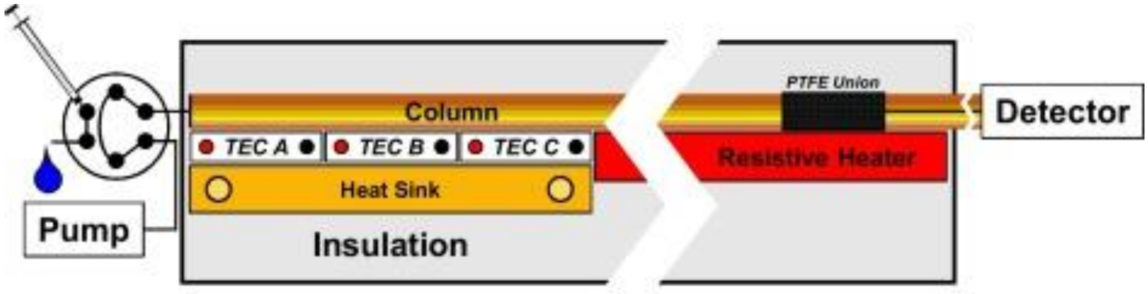

Figure 14. The 3-TEC device utilizes ten independently controlled TECs labeled A-C to control the temperature of the column. Each TEC is a 1.0 x 1.0 cm^2 Peltier device seen in previous versions. The column was fitted directly to the valve and a packed void was used to ensure the stationary phase packing started within the TEC A zone.

3.2.5 TASF Experimental Conditions: Two-Stage Focusing of 5-HT

Isothermal, one-stage, and two-stage focusing conditions were performed on a 39 x 0.150 mm column and a 43 x 0.075 mm column using 500 nL injections. Under isothermal conditions, the entire length of the column was maintained at 65 ºC. Optimal one-stage focusing conditions were found by cooling the first TEC 30 seconds before the injection to 15 ºC, followed by rapid increase to match the separation temperature at varied time points. These time points were staggered by 10 seconds, and an optimal focusing time was chosen based on the highest maximum peak height. This was then repeated to determine optimal two-stage focusing conditions by cooling the first two TEC's 30 seconds before injection to 15 ºC. The first TEC was heated to match the separation temperature at the time point corresponding to the optimal one-stage focusing time. The second TEC was then heated at time points staggered by 10 s where an optimum focusing time was found based on maximum peak height.

3.2.6 TASF Experimental Conditions: One-Minute Separations of DA and 5-HT

Standards of 10 nM DA and 5-HT diluted in 50 µM AA in aCSF were run on the 4.0 cm column at 16 µL/min using 500 nL injection volumes. Under isothermal conditions, all three TECs and the resistive heater were maintained at 70 ºC. Only TEC C was used for focusing under TASF conditions. This TEC remained at 70 ºC during the injection, followed by a reverse in polarity to cool to 5 ºC for focusing, and then is subsequently heated back to 70 ºC all within one separation. To find optimal focusing times, this TEC was cooled at time points ranging between 3 – 15 seconds and heated at time points ranging between 13 – 35 seconds. An optimal focusing time was chosen based the resolution between DA and both the aCSF and temperature change interferences.

3.2.7 *In vivo* Microdialysis Preparation and Surgery

In house concentric style microdialysis probes were made with hollow fiber membranes (13 kD MWCO, Specta/Por RC, Spectrum, Ranco Dominguez, CA) 4 mm in length and 280 µm in outer diameter. Fused silica capillaries (75 µm I.D., 150 µm O.D., Polymicro Technologies, Phoenix, AZ) were used for the inlet and outlet lines. Prior to use, probes were soaked in 70% ethanol and then flushed and immersed in aCSF with DEX for several hours prior to implantation into the brain.

Rats (male, Sprague-Dawley, 250-350g, Charles River, Raleigh, NC) were anesthetized with isoflurane, adjusted to flat skull[143] and implanted with a microdialysis probe. The scalp was shaved and the skull was exposed. A craniotomy was performed and the dura was carefully removed away to expose the brain. The incisor bar was adjusted so that the dorsal-ventral measurements at lamda and bregma were no more than 0.01 mm apart. The microdialysis probe was lowered into the striatum using flat skull coordinates 1.2 mm posterior to bregma, 2.5 mm lateral to midline, and 7mm below dura. Probes were secured with bone screws and acrylic cement and the incision was closed with sutures. Anesthesia was removed and the rats were housed in a Raturn Microdialysis Bowl (MD-1404, BASI, West Lafayette, IN) constant flow through the microdialysis probe at 0.6 nl/min. This system rotates when an animal starts walking to prevent the animal from rotating and twisting the microdialysis inlet/outlet. The concentration of DEX was 10 µM for the first 24 hours and then 2 µM for the remainder of the experiment.

3.2.8 *In vivo* Procedure

Following one hour of aCSF flow through the microdialysis probe path to stabilize the syringe pump, one hour of 500 nL injections were performed to monitor basal neurotransmitter concentrations. The first 10 injections were performed under isothermal conditions at 70 ºC, and the remainder of the study was performed using the optimized TASF conditions determined using standards in Section 3.2.6. where TEC C is cooled to 5 ºC at 5 seconds and heated to 70 ºC at 25 seconds. After collecting one hour of baseline levels, a 20-minute K^+ stimulation was performed by introducing 100 mM K^+ into the probe flow path using the microdialysis valve. One hour after the onset of DA and 5-HT increase from the K^+ stimulation, the stimulation was repeated using 10 µM nomifensine.

3.3 Results and Discussion

3.3.1 Simulation Analysis: Two-Stage Focusing of 5-HT

Volume overload was not expected to play a significant role when using the larger 150 µm i.d. column diameter, as an injection volume of 500 nL onto a 40 x 0.150 mm column relates to a value of $V_{inj}/V_{col} = 1.26$. However, limited band broadening does occur under these conditions and one stage of focusing leads to an increase in peak height by a factor of 1.8 (Figure 15). The second stage of focusing is predicted to maintain the previous solute band compression, but not induce a further increase in peak height as one stage of focusing is enough to eliminate volume overload effects. Here, the Δk' generated by the 15 – 65 °C change is sufficient to compress the band and reverse the broadening during injection.

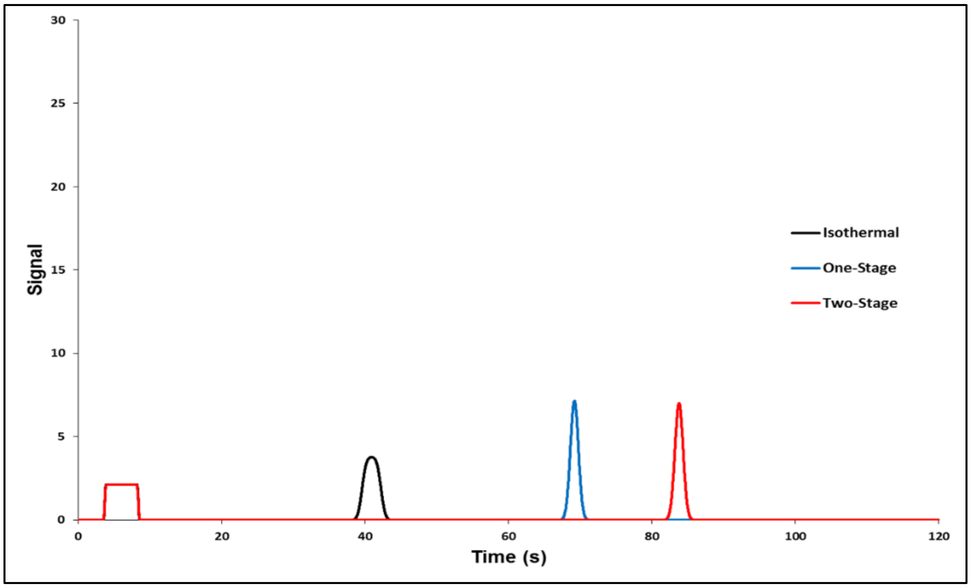

Figure 15. Simulations of isothermal (black), one-stage (blue), and two stage (red) focusing of 5-HT on a 40 x 0.150 mm ID column. A flow rate of 6.4 µL/min was used to maintain temporal resolution below two minutes.

The focusing and separation temperatures were 15 °C and 65 °C respectively. Little enhancement of 5-HT is expected with a second stage of focusing.

Simulations using the 75 µm i.d. column (Figure 16) predict a vast improvement in sensitivity when using two stages of focusing. Volume overload effects are more significant here, with a value of $V_{inj}/V_{col} = 5.06$. A single stage of focusing for 40 seconds at 15 ºC raises the maximum signal from 3.77 to 18.29, for 4.85-fold increase. When a second stage of focusing is added for 60 seconds at 15 ºC, the solute band is further compressed increasing the maximum signal by a factor of 1.55 relative to the first stage of focusing. This maximum signal of 28.34 results in a 7.51 factor increase for two-stage focusing relative to the isothermal separation.

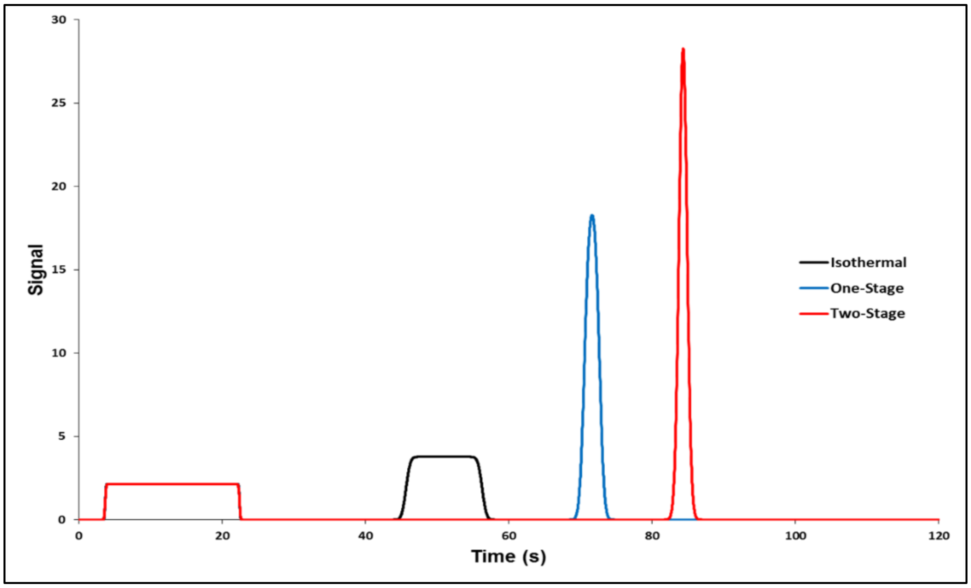

Figure 16. Simulations of isothermal (black), one-stage (blue), and two stage (red) focusing of 5-HT on a 40 x 0.075 mm ID column. A flow rate of 1.6 µL/min was used to maintain temporal resolution below two minutes and maintain constant linear velocity between the two columns. The focusing and separation temperatures were 15 °C and 65 °C respectively. A 7.51 factor increase is expected when two-stage focusing is used when compared to the isothermal run.

These results indicate that with two-stage TASF, the sensitivity enhancement predicted by reducing the column internal diameter by a factor of 2 to obtain a 4-fold increase in signal is theoretically attainable. Without this focusing, volume overload would broaden the signal to values lower than those predicted with the larger column diameter. These results also predict retention times for 5-HT that fall within the initial temporal resolution goal of two minutes. Two stages of focusing can be completed on time scales well below that of the separation, making this technique practically useful for high-speed separations provided that the experimental results match those predicted by the simulations.

3.3.2 Standard Sample Analysis: Two-Stage Focusing of 5-HT

The same conditions used in the simulations were then applied experimentally to reproduce the simulated results. This would validate the simulations for method development purposes using 5-HT, by determining the accuracy of solute band tracking in space during the separation to determine optimal focusing times. Careful control of the set temperature of TEC A & B would be needed to ensure that the 5-HT solute band did not exceed 1 and 2 cm before TEC A and B were heated.

While TASF did help to improve the sensitivity of the separation, multiplicative focusing only improved the maximum signal to a low extent for the 150 μm i.d. column. Maximum peak heights and enhancement ratios are shown in calculated in Table 4, while Figure 17 displays an overlay of optimized one-stage and two-stage separations of 5-HT along with the isothermal run for the 150 μm i.d. column. A peak height for 5-HT was found to be 11.27 nA relative to the baseline. When the separation was repeated using the optimal one-stage focusing time of 50 seconds, a 1.46-fold increase in signal was observed, with a maximum peak height of 16.44 nA. Two-stage focusing with an optimal focusing time of 80 seconds, provided an additional 1.04-fold increase in signal, corresponding to a maximum peak height of 17.18 nA. Together, this produces a total 1.52-fold increase in signal, with the bulk of this enhancement is provided by the first focusing zone. Because of the increase in backpressure needed to cool an additional TEC for two-stage focusing countered by a reduction in flow rate or column length, it does not appear that two-stage focusing would be recommended for this separation using the 150 µm i.d. column as the total benefit compared to one-stage focusing is minimal.

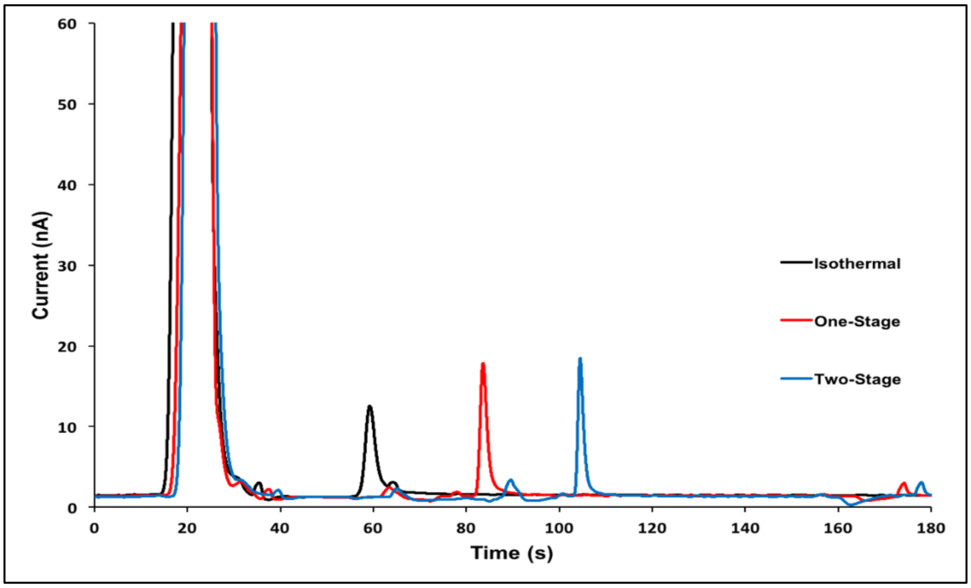

Figure 17. Chromatograms of isothermal (black), one-stage (blue), and two stage (red) focusing of 5-HT. Column: 39 x 0.150 mm with Acquity BEH C18 1.7 µm particles, flow rate = 6.4 µL/min, V_{inj} = 500 nL. The focusing and separation temperatures were 15 °C and 65 °C respectively. As predicted by the simulations, little enhancement is observed through the second stage of focusing with a total enhancement of a 1.52 factor increase.

Table 4. Peak height enhancement data for 150 um ID column with multiplicative temperature focusing

Conditions	Peak Height	(Peak Height) / (Peak Height)$_{iso}$	Plate Count
Isothermal	11.27	1.00	1930
One-Stage	16.44	1.45	9830
Two-Stage	17.18	1.52	25600

Table 5. Peak height enhancement data for 75 um ID column with multiplicative temperature focusing

Conditions	Peak Height	(Peak Height) / (Peak Height)$_{iso}$	Plate Count
Isothermal	3.31	1.00	100
One-Stage	32.09	9.70	10800
Two-Stage	44.64	13.50	17100

Maximum peak heights and signal enhancement ratios for one- and two-stage focusing during runs on the 75 µm column are displayed in Table 5 while Figure 18 displays the overlay of optimized one-stage and two-stage separations of 5-HT along with the isothermal run. As expected with such a large value of V_{inj}/V_{col}, volume overload degraded the maximum value of the isothermal separation significantly. A volume overload peak was observed corresponding to 5-HT which elutes from 86 – 103 s. Rather than this peak being detected as a clean plateau similar to the parabens, the 5-HT volume overload peak is characterized by a plateau followed by a tailing edge spike in signal. This shape is reproducible and consistent with previous studies done over a range of mobile phases and columns. The peak height at the central point of the plateau is equal to 3.31 nA relative to the baseline. One-stage focusing with an optimal focusing time of 60 seconds resulted in a 9.70-fold increase in signal, with a maximum peak height of 32.09 nA. Two-stage focusing provided a further 1.39-fold signal increase at an optimal focusing time of 90 seconds, to produce a maximum peak height of 44.64 nA. The full optimization to determine this focusing time is shown in Figure 19, largely resembling the spectrum of focusing observed using the paraben samples. Like the previous study, focusing for times longer than 90 s results in broadening of the solute band by dispersion and a loss of compression. Together, the two stages of focusing enhances the isothermal signal by a factor of 13.5.

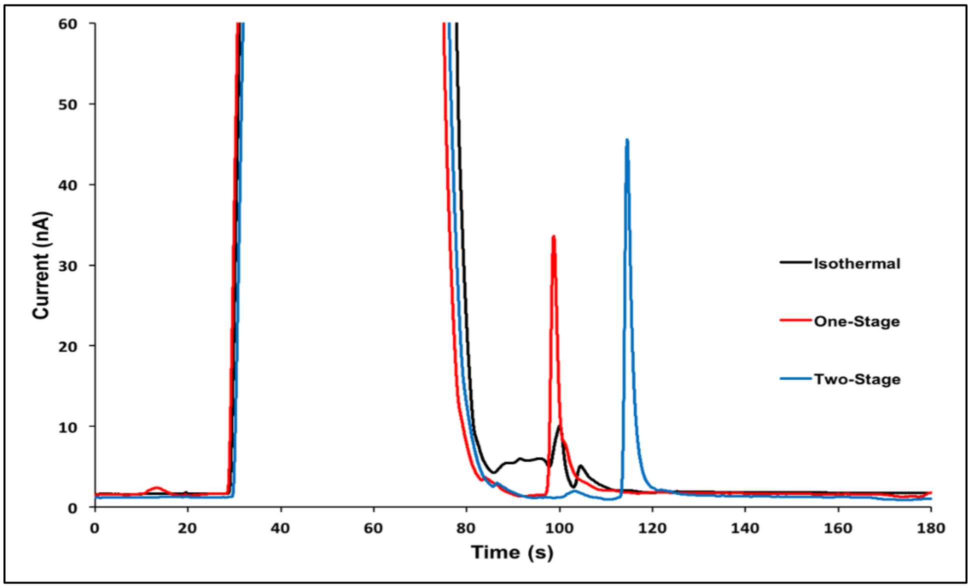

Figure 18. Chromatograms of isothermal (black), one-stage (blue), and two stage (red) focusing of 5-HT. Column: 43 x 0.075 mm with Acquity BEH C18 1.7 µm particles, flow rate = 1.6 µL/min, V_{inj} = 500 nL. The focusing and separation temperatures were 15 °C and 65 °C respectively. The second stage of focusing increases the maximum 5-HT signal by a factor of 13.5 relative to the isothermal signal.

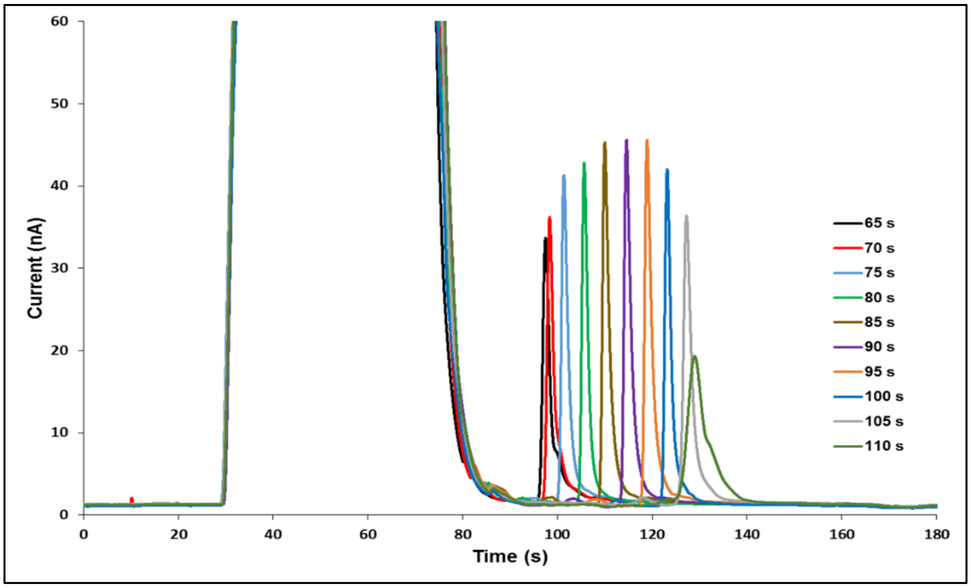

Figure 19. The focusing time optimization for the two-stage focusing of 5-HT on the 43 x 0.075 mm column. Focusing times ranged from 65 – 110 s with 90 s being chosen as the optimum for producing the largest maximum signal.

TASF improved the separation sensitivity using both column configurations, but the capabilities of this device are best shown when comparing the separations for each column configuration that produced the maximum signal. An overlay of the fully optimized two-stage focusing separations of 5-HT for the 150 and 75 µm columns is shown in Figure 20 where the maximum peak heights were 17.18 and 44.64 nA for the 150 and 75 µm columns respectively. This result corresponds to a 2.60-fold increase in signal by reducing the column internal diameter by half and only a 15 s increase in run time.

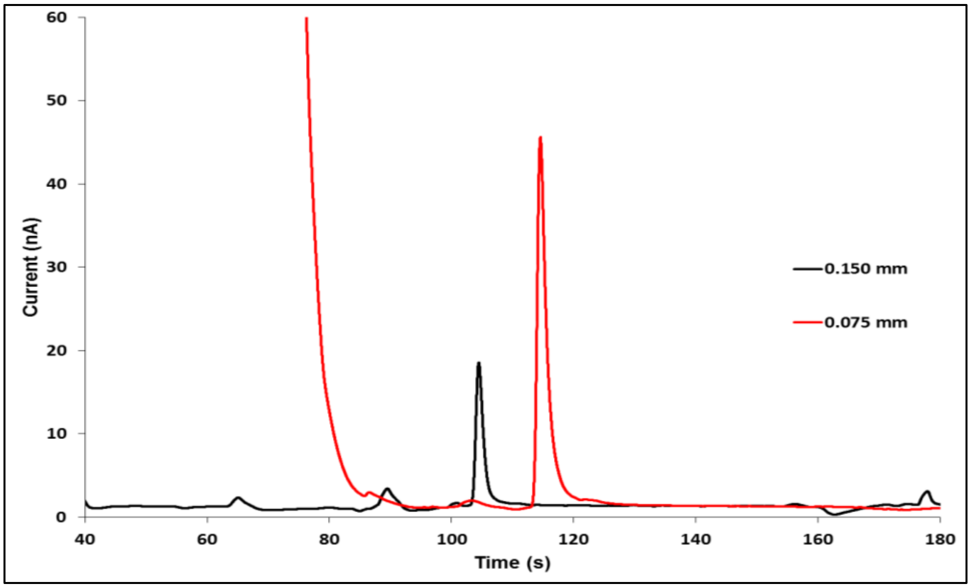

Figure 20. A comparison between the fully optimized two-stage focusing conditions for the 150 µm (black) and the 75 µm (red) columns. Multiplicative focusing reduces the effects of volume overload on the small column for a fixed injection volume, restoring the signal enhancement associated with decreasing diameter by increasing the total signal by a factor of 2.60.

This result is lower than predicted, with the theoretical signal enhancement equal to a 4-fold increase. The most likely reason for this is that the simulations do not predict post-column broadening effects such as those in the connection tubing or detector. As mentioned in the previous section, post-column dispersion effects are worsened as the column diameter decreases. When post-column dispersion is low compared to the column's dispersion contribution, the effects may not be apparent at larger column diameters. However, as column diameter decreases, post-column dispersion effects become large relative to the column dispersion. These effects are not reduced by TASF, resulting in observed peaks that are broader than predicted.

Despite this, the results indicate that TASF can be used to reduce detection limits for high-speed separation of 5-HT through the use of smaller column diameters. The simulations used in method development exhibited the same high level of accuracy for solute band tracking as shown previously for the parabens. Deviations in retention time between the simulations and experimental data are roughly equal to the Δt_0 due to the post-column dead volume of the instrumentation and small changes in column length from the simulated 4.0 cm. With only slight modifications to focusing time, the simulations provided parameters to effectively focus 5-HT in successive compression zones to increase the signal measured for a given injection volume. This result demonstrates the utility of TASF when applied to high-speed separations of 5-HT using capillary scale columns to enhance concentration sensitivity.

3.3.3 Simulation Analysis: One-Minute Separations of 5-HT and DA

After successfully integrating two-stage TASF techniques into 5-HT separations, the simulations were used to develop conditions to simultaneously monitor DA and 5-HT with one-minute resolution. Under isothermal conditions, DA is lost in the early eluting ascorbate interference and broadened through volume overload when the conditions required to reduce the retention time of 5-HT to below one minute are chosen. By focusing at sub-ambient temperatures at TEC C after the ascorbate interference has nearly eluted past 3 cm, the DA solute band can be focused and simultaneously slowed within this zone to while 5-HT continues traveling through the column at higher speeds within the heated zone. Once, the entire 5-HT solute band travels into the focusing zone of TEC C, the temperature will be rapidly heated to elute both peaks down the column. This will not only enhance the signal of both neurotransmitters through compression, but will shift DA retention outside of the ascorbate interference while maintaining one-minute resolution for both neurotransmitters. A visual representation of this method is shown in Figure 21.

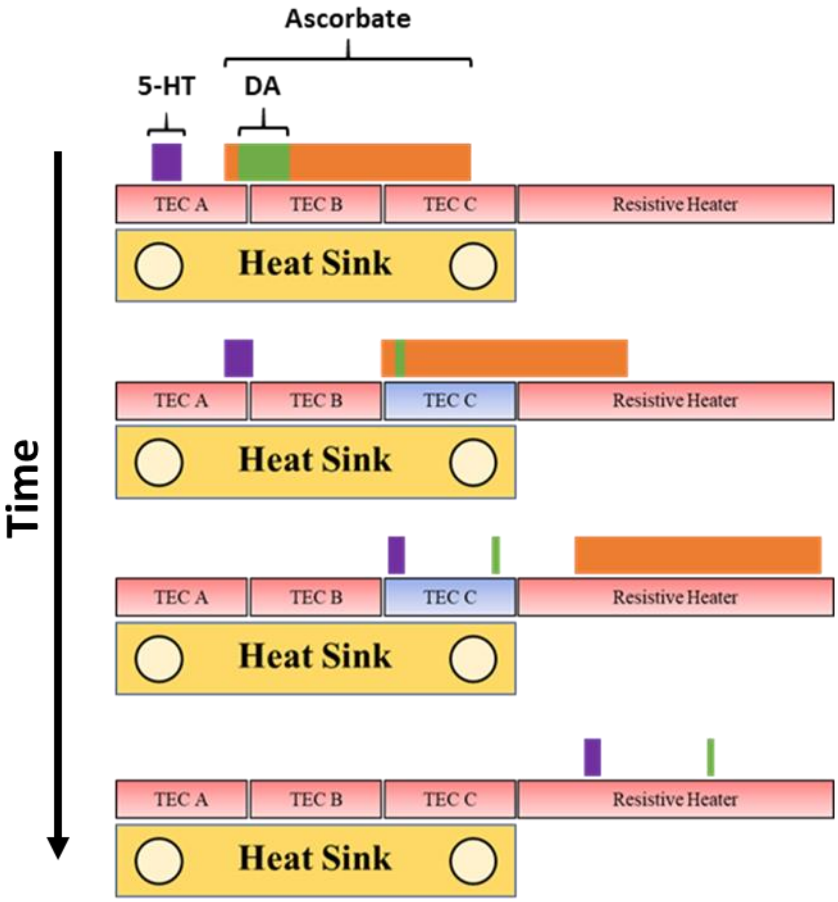

Figure 21. Visualization of TASF conditions proposed for one-minute separations of 5-HT and DA. The major challenge of this separation is to focus the DA solute band to mitigate volume overload broadening effects under conditions that elute 5-HT within one minute. The DA peak also must be separated from the high concentration ascorbate interferece through modulating temperature to subambient temperatures to increase DA retention. TEC C is cooled just as the DA solute band enters the zone, and maintains this temperature until the entire 5-HT solute band has traveled into the zone. The TEC is then rapidly heated to elute both focused solute bands to the detector.

The simulated chromatogram is shown in Figure 22 for isothermal and TASF conditions. The TASF conditions chosen maintain TEC at 5 ºC for the first 25 seconds and is then heated to match the 70 ºC separation temperature. Although the focus of this study the separation of DA and 5-HT in under a minute, 3-MT was also included in the simulation to determine if conditions predicted sufficient resolution with 5-HT to prevent co-elution. Predicted peak heights for each neurotransmitter and the relative enhancement from focusing is shown in Table 6. Not only does focusing increase the maximum peak height of DA by a factor of 2.846, but it shifts the retention time from 22 s to 34 s. It is important to shift DA elution time later than the early eluting interference observed in the dialysate matrix, which decreases dramatically after ~20 s. The 5-HT peak is enhanced more moderately by a factor of 1.685, with a shift in retention time from 43.1 to 46.2 s. Baseline resolution is also maintained between 5-HT and 3-MT. While these simulations do not predict changes in flow rate for constant pressure conditions, they provide initial test conditions to separate solutes of interest and provide a range of focus times to test experimentally. It is predicted that retention times will slightly increase due to a short drop of flow rate when focusing, especially for 5-HT since it has not yet reached the focusing zone when this occurs. This is accounted for by ensuring 5-HT elution time is less than 50 s providing a 10 s buffer before one-minute resolution is lost.

Table 6. Simulated peak height enhancement data for DA, 5-HT, and 3-MT with one-stage TASF

	Peak Height Iso	**Peak Height TASF**	**Peak Height TASF / Peak Height Iso**
DA	13.22	37.62	2.846
5-HT	11.85	19.97	1.685
3-MT	10.54	10.54	1.000

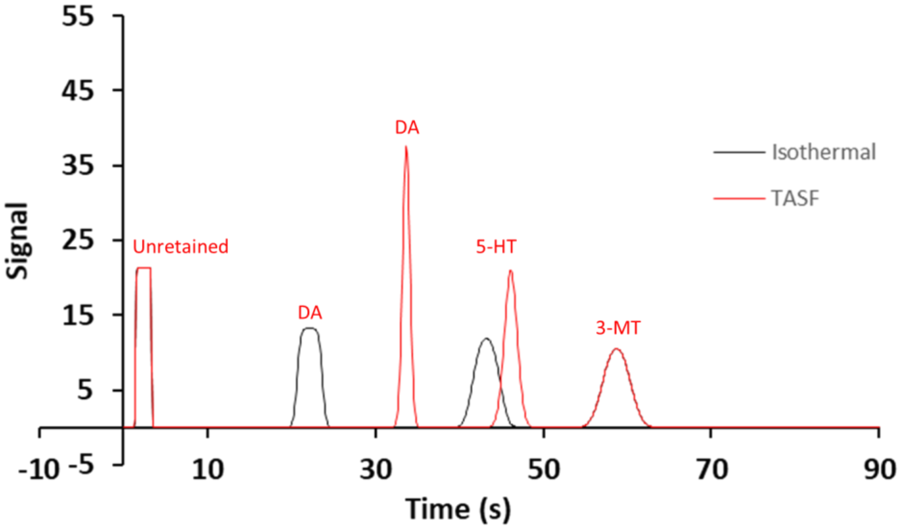

Figure 22. Simulated chromatograms for DA, 5-HT, and 3-MT under isothermal (black) and TASF (red) conditions. Focusing occurs at the TEC C for the first 25 s of the separation at 5 °C before heating to 70 °C. These simulations predict a shift in DA retention to from 23 to 34 s to avoid the tailing ascorbate peak, while also enhancing the signal by a factor of 2.85. The 5-HT peak is moderately focused with a peak enhancement of 1.68 and maintains baseline resolution from 3-MT in under one minute.

3.3.4 Standard Sample Analysis: One-Minute Separations of 5-HT and DA

The major challenge of this separation was maintaining resolution between DA and two interferences which are not accounted for in the simulations. Specifically, the interference generated by the temperature change which elutes before DA and an interference from the aCSF sample matrix which elutes after DA. The former can be modulated by choosing focusing conditions which cool within the first 10 seconds and return to separation conditions within 30 seconds. This provides sufficient trapping of DA and enough time for the heating transient to pass before DA is detected. The latter is generated by the divalent cations within the aCSF solution. This interference was avoided by changing the %B of the mobile phase to shift the retention time between DA and 5-HT. Originally the separation was performed using constant flow conditions as used for all previous studies. Since flow rate must be lower to account for the pressure increase during focusing, a higher %B was needed to maintain one-minute temporal resolution. This caused the interference to co-elute with 5-HT and was the primary motivation for the addition of constant pressure controls. Now, lower %B and higher flow rates could be used to shift the interference closer to DA without sacrificing temporal resolution.

The chromatograms in Figure 23A-D display isothermal and TASF blank runs of 50 µM AA in aCSF (A&C) and standards of 10 nM DA and 5-HT (B&D). The aCSF interference elutes between 31 – 35 seconds for isothermal conditions and between 38 – 42 seconds using temperature programming. The 5-HT peak shape is relatively unchanged by the TASF conditions, although there is a small increase in maximum peak height from 0.339 to 0.427 nA. Focusing times must be optimized for DA, and focusing for times long enough to sufficiently compress the 5-HT solute band causes the DA peak to co-elute with the temperature change interference. The shift in retention time from 48 to 53 seconds under TASF conditions is a consequence of the constant pressure controls temporarily decreasing the flow rate.

The impact of TASF is best represented by observing the DA peak. Under isothermal conditions, it elutes as a broad doublet peak from 20 – 25 s likely due to volume overload as predicted by the simulations. As seen in previous studies, 5-HT generates a characteristically abnormal peak shape from the predicted plateau associated with volume overload so it is likely DA would present similar abnormalities. When temperature programming is applied, the DA peak elutes at 35 seconds with a 3.91-fold enhancement of signal. The observed retention times only differ by several seconds (3 s for DA and 5 s for 5-HT) when compared with the simulations, providing accurate parameters to successfully determine focusing conditions for DA and 5-HT where both elute in under one minute outside of the ascorbate interference.

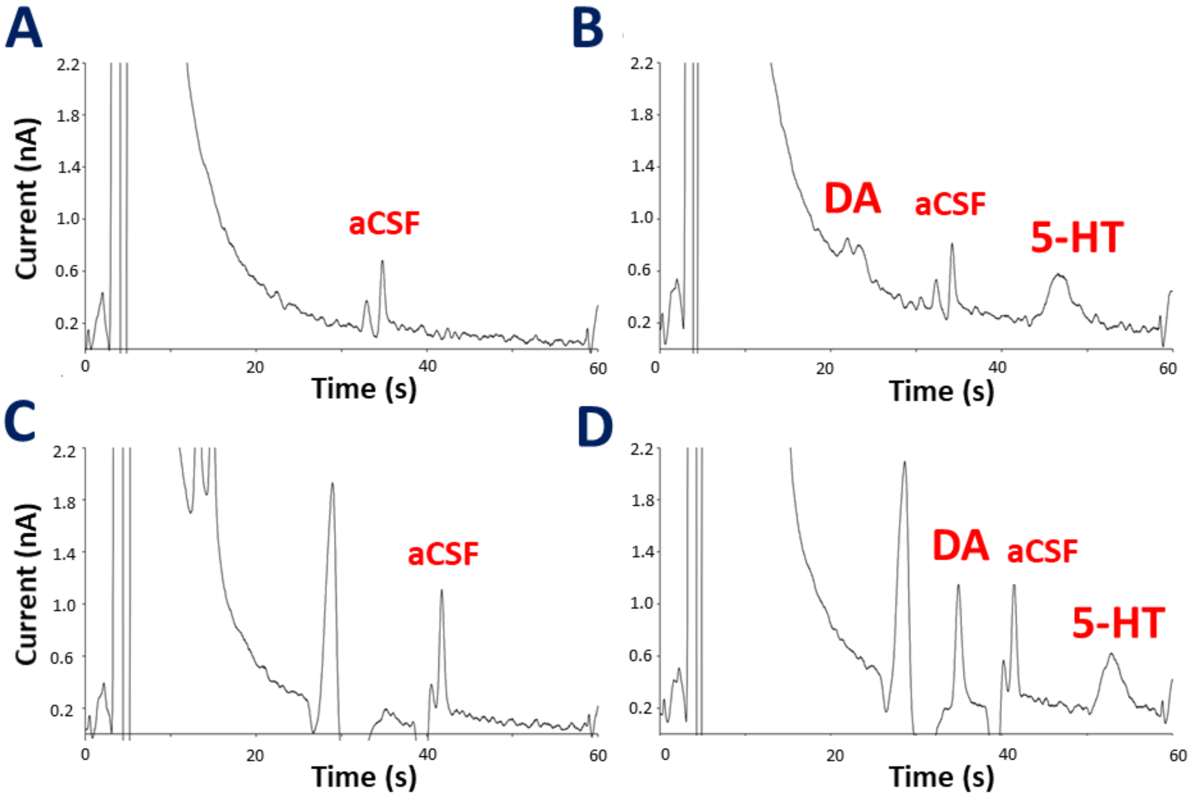

Figure 23. Isothermal runs were performed on both a 50 µM AA in aCSF blank (A) and on 10 nM standards of DA and 5-HT (B). TASF runs were then performed on the blank (C) and the standards (D) to determine retention times for each analyte. The broad volume overload DA peak seen in (B) becomes a sharp peak eluting between the temperature change interference and the aCSF interference with a 3.91-fold signal enhancement.

3.3.5 *In vivo* Analysis

Isothermal runs were first performed to serve as a control to compare to standard samples. Neither neurotransmitter could be observed which is likely due to high noise levels of the detector preventing detection of 5-HT and volume overload degrading the DA signal (Figure 24A). After

10 minutes, the optimized TASF conditions (TEC C, 5:25 s) were used for the remainder of the study. A small peak at 35 s was observed which exactly matches the retention time of DA using standards (Figure 24B), but still no 5-HT peak was observed. Both the temperature change interference and the aCSF interference were present with identical retention times observed in the standard samples.

An important observation of this result is that the *in vivo* dialysate sample matrix does not significantly change the retention time of DA or the two largest interferences present. Tailing of the ascorbate interference is not worse *in vivo* than the tailing of standards containing 50 μm ascorbate. This is useful information for future method development when designing experiments with simulations and choosing retention times to fall outside of this interference.

To ensure the peak at 35 s corresponded to basal DA, a 20-minute stimulation of 100 mM K^+ was performed through retrodialysis. The results of this stimulation are illustrated in Figure 25A-D. The onset of DA increase began 19 minutes after the microdialysis valve was switched which generated not only an increase in the DA signal, but also increased the 5-HT signal above noise levels with a retention time of 52.5 s. This result is particularly encouraging because it provides increased confidence that the peak at 35 s is DA, and that 5-HT matches the standard samples falling within the one-minute temporal resolution goals. This provides unique information regarding the simultaneous measurement of extracellular DA and 5-HT in response to K^+ stimulation. Plots of peak height vs. time are shown in Figure 26. Interestingly, these neurotransmission pathways did not respond in the same way to the K^+ stimulus. While they both lasted for nearly the same length of time, the 5-HT levels spiked to a maximum almost immediately before slowly decaying back down to basal levels steadily. However, the DA levels too several minutes to reach a maximum level, before reaching a steady state, and finally dropping back to basal levels quickly.

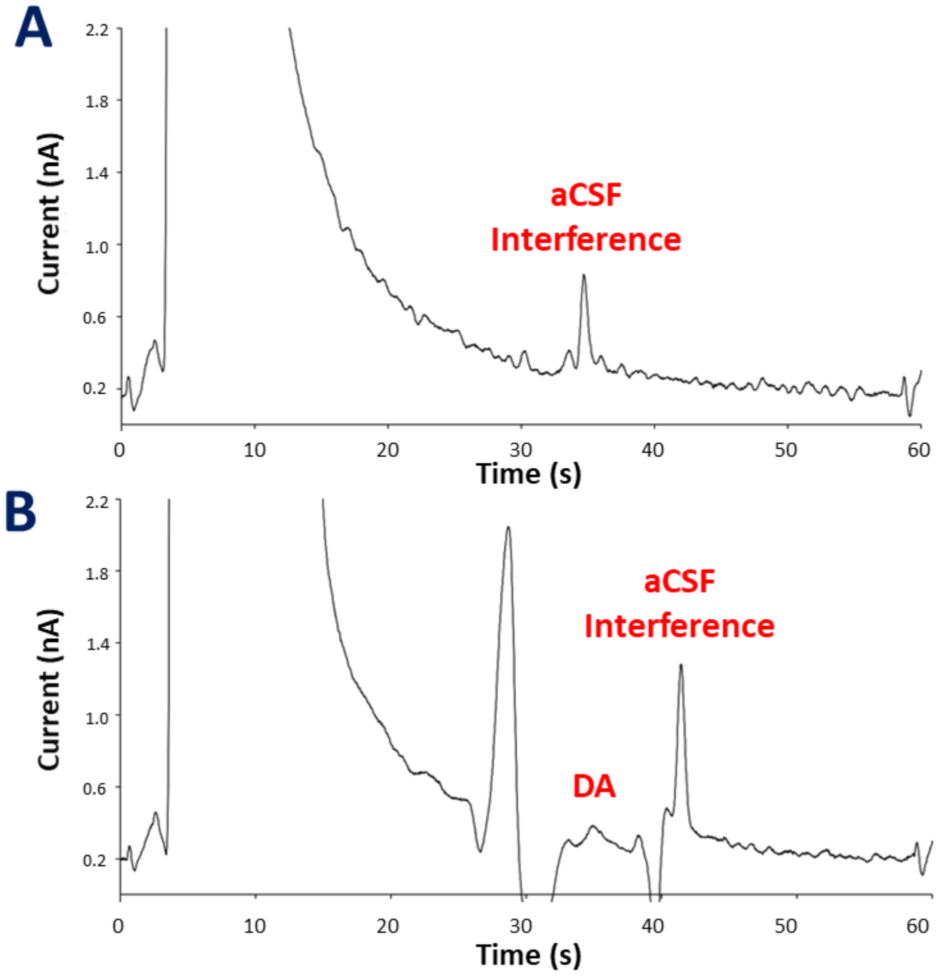

Figure 24. Basal microdialysis samples run under isothermal (A) and TASF (B) conditions. Although noise levels are too high to observe 5-HT, a peak at 35 s elutes where DA is expected. Neither neurotransmitter is detectable under isothermal conditions.

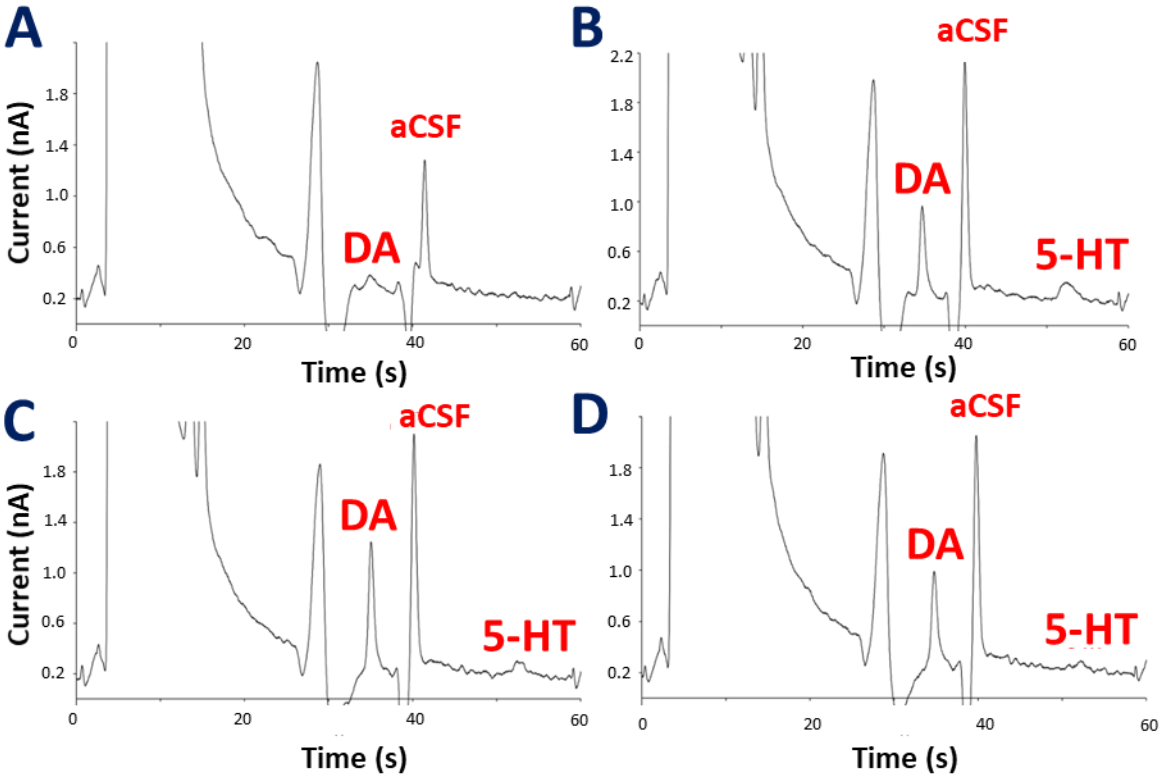

Figure 25. Chromatograms of in vivo microdialysis samples at various time points following 20-minute 100 mM K$^+$ stimulation via retrodialysis. These show the measurement of DA and 5-HT just before stimulation (A), 20 minutes after the start of the stimulation (B), 24 minutes after the start of the stimulation (C), and 37 minutes after the start of the stimulation (D). The K$^+$ stimulation raises 5-HT high enough to detect above the noise levels as well as generating a 8.78-fold increase in the DA signal.

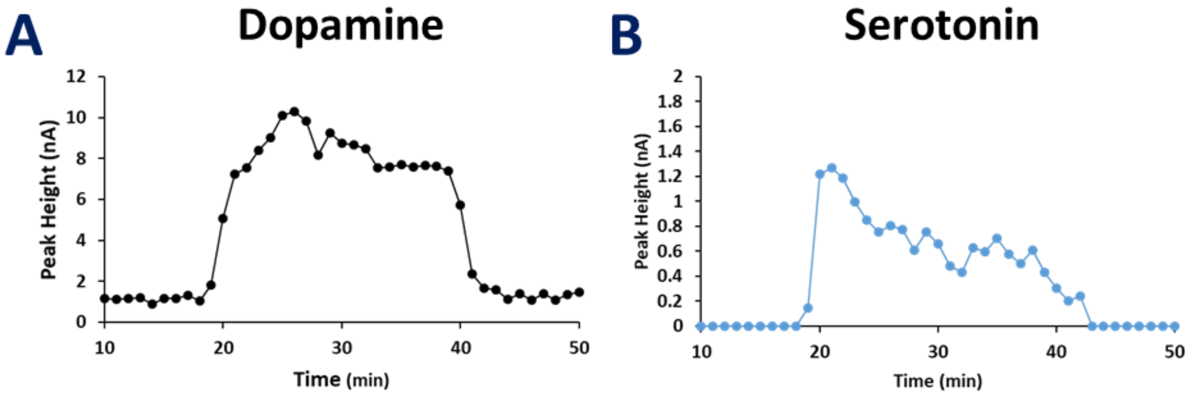

Figure 26. The peak height as a function of time after stimulation is shown for DA (A) and 5-HT (B). Here t = 0 is the time that the stimulation began and t = 20 is the end of the stimulation.

While the K^+ stimulation provides positive evidence that the peak at 35 s is DA, it is not selective for DA leaving doubt that this could be another compound within the sample matrix. To conclude that this is truly DA, a perfusion of 10 μM nomifensine in aCSF was performed using the same technique carried out for the K^+ stimulation. Nomifensine is a DA reuptake inhibitor, which should selectively cause an increase in extracellular DA. The results are shown in Figure 27, where 19 minutes after the microdialysis valve was switched, an onset of the DA signal was observed, generating a 4.40-fold increase in DA signal.

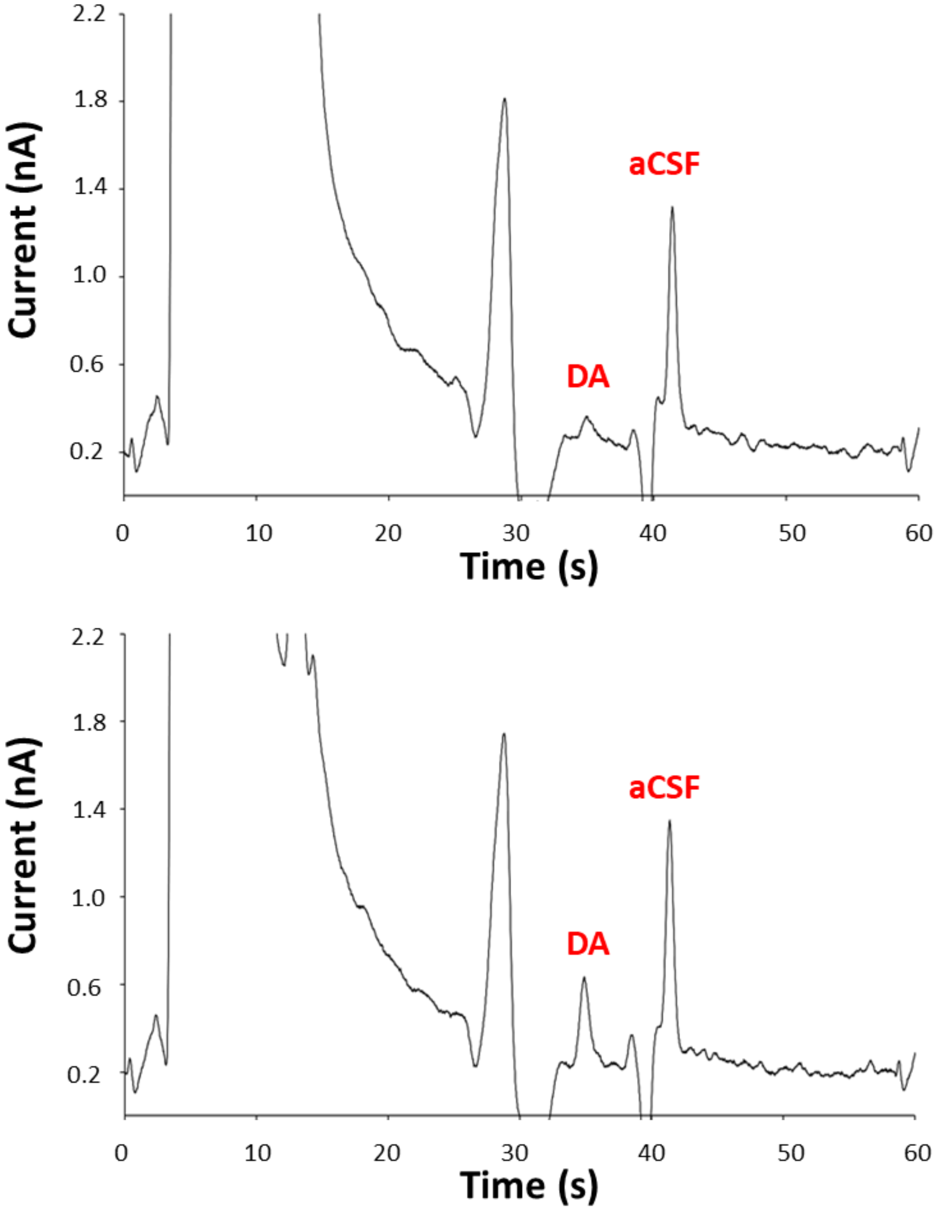

Figure 27. Chromatograms of in vivo microdialysis samples at various time points following 20-minute 10 µM nomifensine stimulation via retrodialysis. These show the measurement of DA and 5-HT just before stimulation (A), and 20 minutes after the start of the stimulation. The nomifensine selectively increased the peak at 35 s providing evidence that this peak is basal DA.

This experiment provides a unique method for using TASF to trap target neurotransmitter solutes within the cooled focusing zone after interferences have eluted, with a goal of decreasing separation times. The time required for method development is significantly reduced by the accuracy of simulations to choose conditions necessary for the desired separation. Instead of using TASF solely to reduce pre-column dispersion, this experiment has shown the versatility of the device to modulate the retention time of analytes based on the temperature dependence of retention and to develop novel separations techniques. Higher %B mobile phase compositions and flow rates can be used to increase the temporal resolution of a given separation, while avoiding volume overload effects for low retention solutes and ensuring fast separations of highly retained solutes. This is important for applications similar to this study where gradient elution is not a viable option to separate solutes with large differences in k'.

3.4 Conclusions

We have demonstrated a separation method to obtain 1-minute temporal resolution of both DA and 5-HT using online-microdialysis coupled HPLC *in vivo* through the implementation of multiplicative temperature-assisted solute focusing techniques. To our knowledge, this is the first time this has been achieved at the time of publication. The implementation of TASF provides a tool to alleviate volume overload effects associated with column diameter miniaturization, and has proven to enhance sensitivity of 5-HT through multiplicative focusing methods. The developed simulations provide an integral tool in method development to screen conditions to achieve a desired separation significantly faster than what could be done experimentally.

4.0 Validation of Dexamethasone-Enhanced Continuous-Online Microdialysis for Monitoring Glucose for 10 Days After Brain Injury

Portions of this chapter were previously published in Gifford, E., K.; Robbins, E., M.; Jaquins-Gerstl, A.; Rerick, M., T.; Nwachuku, E., L.; Weber, S., G.; Boutelle, M., G.; Okonkwo, D., O.; Puccio, A., O.; Michael, A., C. *ACS Chemical Neuroscience* **2021.**

4.1 Introduction

Traumatic brain injury (TBI) is an epidemic reported to affect over 2 million people in the US annually, leading to 227,000 hospitalizations and 61,000 deaths in 2017.[144] In the hours and days following the onset of the initial injury, secondary injuries can spread to the vulnerable tissue surrounding the primary injury site.[145-147] These secondary injuries introduce further negative health risks for the patient including seizures, ischemia, and spreading depolarizations (SD). Monitoring SD events has become a focal point for efforts to improve neurocritical care, because of their strong correlation with predicting patient outcomes.[145, 148, 149] These events cause a wave of neuronal depolarization to disseminate through the cortex and can occur in spontaneous clusters following the initial injury. Repolarization efforts induce high energy strains on the affected tissue, which can result in decreases in extracellular glucose concentrations.[147, 150-153]

Microdialysis has been proven to be a useful tool to provide analytical insight into these SD events with on-going research for its widespread implementation in a clinical setting to improve patient care. The Boutelle group has previously developed rapid sampling microdialysis (rsMD) providing an online electrochemical assay to monitor both glucose and lactate in 30 second intervals designed to be used bedside in neurointensive care units.[79] More recently, continuous-online microdialysis (coMD) expands upon this technology by directly transporting dialysate to a microfluidic chip containing glucose and lactate biosensors and potassium ion-selective electrodes.[80, 81, 154] This provides an important, portable tool that has been incorporated into a clinical setting to study SD events in patients following TBI.

One concern regarding the implantation of the microdialysis probe into living tissue is the penetration injury and the subsequent foreign body response by the tissue.[155-160] Disruption of the blood-brain barrier activates a near immediate response of microglia, resulting in an encapsulation of the probe.[161] The abnormal state of the tissue surrounding the probe track leads to complications in long-term microdialysis measurements and difficulty in data interpretation.[162-164] Efforts to mitigate this foreign body response has led to the development of dexamethasone enhanced microdialysis.[82, 160, 161, 165-167] In this method, a low micromolar concentration of the anti-inflammatory drug dexamethasone (DEX) is transported locally to the tissue surrounding the implanted membrane through retrodialysis. Results have indicated that this strategy is effective in reducing ischemia, gliosis, and cell loss near the probe track. This significantly improves the quality of microdialysis measurements for long-term studies, and has provided a means to monitor of glucose and potassium transients associated with SD events for 10 days following after the onset of primary injury.[83]

An observation made during the 10-day microdialysis study was the steady decline of glucose to concentrations below the detection limit of the system in 80% of animal models who experienced TBI through controlled-cortical impact (CCI). One hypothesis for this observation is that the TBI causes a metabolic phenomenon depleting pericontusional glucose. However, the same loss of detectable glucose could also be observed due to probe fouling over time impacting the integrity of the membrane itself. Therefore, a method is needed to validate the microdialysis probe integrity in these cases.

The goal of this study is to validate the microdialysis probe performance through the retrodialysis of the non-native peptide $^{D}Y^{D}A^{D}S^{D}F^{D}L$ (yasfl). The D-configuration amino acids yield a peptide which is not hydrolyzed by any known enzyme within the brain, making it a suitable marker to analyze the effects of diffusion in the microdialysis membrane and surrounding tissue. The concentration of this peptide within the analyzed dialysate is governed by Eq 10:

Equation 10

$$C_{out} = R \cdot C_{ext} + (1 - E) \cdot C_{in}$$

where C_{out} is the solute concentration in the dialysate exiting the microdialysis probe, C_{ext} is the extracellar concentration of solute, C_{in} is the solute concentration in the perfusate, R is the recovery fraction, and E is the extraction fraction. In this case, yasfl is not naturally present in the brain, so C_{out} is governed by the perfusate concentration, C_{in}, and the extraction and recovery fractions determined by probe characteristics. Various concentrations of peptide were perfused at day 1 and 7 for control and CCI rats, followed by analytis of dialysate concentrations through LC-MS/MS. Comparison the calculated extraction fraction between the day 1 and day 7 rats, and between the control and CCI rats, would provide insight regarding if the steady glucose decline observed following TBI is correlated to microdialysis membrane integrity.

4.2 Experimental

4.2.1 Retrodialysis Standard Preparation

A 1.0 mM peptide stock solution of $^{D}Y^{D}A^{D}S^{D}F^{D}L$ (yasfl) (GL Biochem, Shanghai, China) was prepared by diluting the solid in water purified using a Millipore Milli-Q Synthesis A10 filtration system. This solution was used throughout the experiment and stored frozen at -20 °C until needed. The 100, 250, and 400 nM retrodialysis standards were prepared through serial dilution of the peptide stock in artificial cerebral spinal fluid (aCSF: 142 mM NaCl, 1.2 mM CaCl2, 2.7 mM KCl, 1.0 mM MgCl2, 2.0 mM NaH2PO4, pH 7.40). These solutions were then filtered using a 0.2 μm PES syringe filter (Corning Inc., Corning, NY) before perfusion.

4.2.2 Dialysate Sample Storage

Collected dialysate samples were stored at -20 °C until ready to be analyzed. Then, a 20 μL aliquot of the each retrodialysis and dialysate solutions diluted to a 200 μL total volume using Optima LC-MS grade water (Fisher Chemical) in separate autosampler vials (Thermo Scientific, Rockwood, TN) before placing in the refrigerated autosampler at 5 °C.

4.2.3 Heavy Label Internal Standard

The heavy peptide internal standard was prepared using an offline demethylation procedure[168], followed by sample cleanup to remove the labeled peptide from the reaction matrix. The peptide stock solution was diluted to a final concentration of 1.0 μM using purified water, and a 198.4 µL aliquot was added to an autosampler vial (Thermo Scientific). To begin the labeling procedure, 2.0 µL of glacial acetic acid (Fisher Chemical, Fair Lawn, NJ) and 8.0 µL of 4% formaldehyde-d_2 (Sigma-Aldrich, St. Louis, MO) were added to the vial before vortexing the mixture. Next, 8.0 µL of 600 mM sodium cyanoborohydride (Sigma-Aldrich) was added to the vial before vortexing and allowing to react for 5 minutes. To quench the reaction, 32.0 µL of 1% ammonium hydroxide (Sigma Aldrich) was added to the vial, vortexed, and allowed to sit for 1 minute. Last, 16.0 µL of 5% formic acid (Sigma-Aldrich) was added to the vial and vortexed one final time. The final concentration of heavy labeled peptide was approximately 0.75 µM.

To avoid untargeted heavy labeling of peptide within the samples during the subsequent online labeling steps, extraction of heavy labeled peptide from the reaction matrix is desired. To do this, 100 µL Pierce C_{18} pipette tips (Thermo Scientific) were used to prepare a purified heavy label internal standard stock solution. The tips were first cleaned by aspirating twice with 50 % LC/MS grade acetonitrile (Fisher Scientific), before phase equilibration by aspirating twice with 0.1% trifluoroacetic acid (Fisher Scientific). Heavy labeled peptide was then loaded onto the pipette solid phase by aspirating the heavy labeled stock solution 10 times. To ensure all labeling reagent had been removed from the solid phase, the tips were aspirated twice in a mixture of 0.1% trifluoroacetic acid and 5% acetonitrile. Finally, the purified heavy peptide stock solution was made by eluting the tip using 100 µL of 50% acetonitrile and diluting to a final volume of 2.0 mL. The final concentration of purified heavy labeled peptide stock was approximately 40 nM. This solution was stored frozen at -20 °C until needed on the day of analysis when it was thawed at room temperature before use. A 30 µL aliquot was diluted to 300 µL total using purified water in an autosampler vial. The final concentration was approximately 4.0 nM yasfl.

4.2.4 Animal Surgeries

All procedures involving animals were approved by the Institutional Animal Care and Use Committee of the University of Pittsburgh. Studies were performed in male Sprague-Dawley rats (Charles River, Raleigh, NC) weighing 250-350g. Concentric-style microdialysis probes were constructed in-house with a 4 mm active sampling length using cellulose membranes with 13 kDa molecular weight cutoff (Spectra/Por). The inlet and outlet lines were fused silica (75 μm ID, 150 μm OD). Prior to use the probes were flushed with ethanol followed by sterile filtered (Nalgene sterile filters, 0.2 μm pore size, Fisher, Pittsburgh, PA) artificial cerebrospinal fluid (aCSF; 142 mM NaCl, 1.2 mM $CaCl_2$, 2.7 mM KCl, 1.0 mM $MgCl_2$, and 2.0 mM NaH_2PO_4 (all salts from Sigma-Aldrich) adjusted to a pH of 7.4). Probes were perfused at 1.67 μL/min with a syringe pump (Harvard Apparatus). Probes were inserted at an angle of 51° from vertical, to ensure that the entire active length was within the cortex. The probes were perfused with aCSF containing 10-μM Dex for the first 24 hrs, 2-μM Dex for the next 96 hrs, and no Dex thereafter.

4.2.5 Column Preparation

The method for making outlet frits for the 50 μm i.d. x 360 μm o.d. column blanks was followed the procedure outlined by Kennedy.[142] A 25% (v/v) solution of formamide and Milli-Q water was diluted 1:1 with potassium silicate. A 10 μL drop was then placed on a piece of Watman filter paper (Cat No. 1822-025). The end of the column blank was pressed against the wet section of the filter paper and twisted to leave a hole twice for each column blank. They were then placed in an oven Thermo Focus series GC oven set to 85 ºC for 12 hours. The Acquity 5 μm BEH C_{18} particles (Waters, Milford, MA) were slurried in 2-propanol at concentrations of 65 mg/mL. This was sonicated for 20 minutes before packing using the downward slurry method. A Haskel model DSF-150 pneumatic amplification pump (Burbank, CA) was used to pack the column at 20,000 psi for 20 minutes using methanol as the packing solvent, before allowing the pressure to dissipate naturally. The column was trimmed to final length of 3 cm.

4.2.6 Chromatography

The separation was achieved using a Dionex UltiMate 3000 Nano LC system (NCS-3200RS, Thermo Scientific, Germering, Germany) fitted with a micro-LC flow selector as the loading pump, and a Dionex Ultimate 3000 HPLC system (NCS-3500RS, Thermo Scientific, Germering, Germany) fitted with a nano LC flow selector as the analytical pump. Each pump was connected to a 6-port two-position 1/16 in Cheminert injection valve (C72x-669D, VICI Valco, Houston, TX) mounted to the MS stage. A Love Model 1500 proportional-integral-derivative (PID) controller (Dwyer Instruments, Michigan City, IN) controlled a Kapton resistive heater (KH-103-10-P, Omega) to maintain the analytical column at 50 °C. A Dionex WPS-3000 RS autosampler with an internal 6-port, two-position valve fitted with a 1.1 uL sample loop was used for heavy internal standard and reagent injections. The autosampler was refrigerated at 5 °C.

The inlet of the column was connected to a 100 x 0.05 mm fused silica capillary by a 360 µm MicroTight Union (Idex Health & Science, Oak Harbor, WA). Each end of this assembly was fitted directly to the injection valve. The inlet of a 150 mm x 50 µm i.d. x 360 µm o.d. capillary was fitted to the valve while the outlet was connected to the inlet of the 150 mm x 10 i.d µm x 360 µm o.d. capillary using a liquid junction tee (Idex Health & Science). The outlet of the 10 µm i.d. capillary was connected to a fused silica PicoTip emitter (New Objective, Woburn, MA) through a PTFE sleeve. This tip was maintained approximately 1 mm away from the MS source throughout the separation. In the loading position, flow from the analytical pump was directed directly to the MS source, and flow from the loading pump was directed to the column and subsequently to waste. In the elution position, flow from the analytical pump was directed through the column to the MS source, while flow from the loading pump was directed to waste.

The HPLC configuration was modified from the previously published procedure[169, 170] in order to increase automation by directing excess labeling reagents and aCSF to waste prior to elution to the MS source during the sample loading phase. The analytical pump utilized online mixing to deliver solvent. Channel A consisted of 0.5 % acetic acid in Optima LC-MS grade water (Fisher Chemical) while channel B consisted of 0.5% acetic acid in Optima LC-MS grade methanol (Fisher Chemical). The loading pump solvents were mixed manually and contained 0.5% acetic acid, 2% methanol, and 97.5% Optima LC-MS grade water (v/v%). Injections from the autosampler were delivered to the column by the loading pump with a flow rate set to 2 μL/min. During the loading steps, the analytical pump delivered 60% B at a flow rate of 0.4 μL/min directed to the MS source. Following the online labeling steps, the valve position was switched to elute the labeled peptide from the column for detection. This mobile phase composition was maintained for 7 minutes before a 0.2 minute step increase to 90% B was made to elute any components in the dialysate with high hydrophobicity from the column. The mobile phase composition was then switched back to 40% B for 1 minute before switching the valve back to the loading position. The column was then allowed to equilibrate under loading pump mobile phase conditions for 1 minute before the start of the next set of injections. The total time for sample loading, labeling, and elution for each sample was approximately 24 minutes.

4.2.7 Online Peptide Labeling

The peptides in the retrodialysis solutions and dialysate were “light” labeled using a procedure described previously.[169, 170] For each peptide sample to be analyzed (either retrodialysis solution or dialysate), the autosampler was used to inject the purified heavy labeled internal standard (from 4.2.3), followed by the dialysate sample, and finally the light labeling reagent. The light labeling reagent contained 350 µL of triethylammonium acetate (100 mM triethyl amine (Sigma-Aldrich) titrated with 100 mM acetic acid to a pH of 7.4), 3.50 µL of 0.6 M sodium cyanoborohydride (Sigma-Adlrich), and 3.50 µL of 4% formaldehyde (J. T. Baker, Phillipsburg, NJ). During all steps, chromatographic conditions were chosen to maintain high retention of peptides in the column at 2% MeOH. This allows for excess labeling reagents to travel through the column to waste and minimizes the loss of peptides. All injections were a volume of 1.1 µL by the autosampler.

4.2.8 Mass Spectrometry

An LTQ XL linear ion trap mass spectrometer (Thermo Scientific) was used to perform LC-MS/MS analysis on the heavy and light labeled peptides. Positive ion mode nanospray ionization was used with a spray voltage set to 2.3 kV applied to the liquid junction tee at the analytical column inlet. Parent ion fragmentation was achieved using collision induced dissociation with a normalized collision energy of 35 and an activation time of 30 ms. The isolation width for daughter ions was set to ± 1.5 m/z. Parent and daughter ions were chosen based on methods described previously.[169, 170] The parent and daughter ions chosen for both light and heavy yasfl are listed in Table 7.

Table 7. MS/MS parent and daughter ions selected for quantitative analysis.

	Parent Ion (m/z)	Daughter Ions (m/z)
Light yasfl	628.30	479.20; 497.20
Heavy yasfl	632.30	483.20; 501.20

4.3 Results and Discussion

4.3.1 Refining Method for Heavy Isotopically Labeled Internal Standard

Early during method development, the procedure adapted from previous work[169] was used for peptide labeling where an offline "heavy" labeling procedure was adapted for the isotopically labeled internal standards, cutting down the total analysis time from one hour to roughly 25 minutes. The internal standard labeling procedure was performed offline in an autosampler vial, with reagent and diluent volumes determining the heavy labeled peptide concentrations. While this did cut down on the total analysis time, it also came at the cost of nonlinearity when labeling high concentrations of peptide in the dialysate. This was first observed when constructing calibration curves where a series of yasfl peptide standards were made ranging in concentration from 0.098 – 400 nM though 1:4 serial dilution and using a 1 nM IS concentration. At high concentrations, relative peak area values (light peak area/heavy peak area) were lower than expected. This effect was also more dramatic at high concentrations.

The origin of this nonlinearity is shown in Figure 28, displaying the heavy peak area for yasfl versus the serial dilution value of the unlabeled peptide. The serial dilution value is an arbitrary value assigned to each unlabeled peptide solution with 1 corresponding to the lowest concentration (98 pM) and 7 corresponding to the highest concentration (400 nM). Because the concentration of the heavy labeled internal standard remains constant at 1.0 nM throughout the experiment, the expected result is a flat peak area profile across all standards. Instead, the measured heavy peak area value begins to increase between serial dilution value 5 (25 nM) and 6 (100 nM).

The reason for this nonlinearity stems from a reaction yield of approximately 99.75% for the light labeling step. When the offline heavy labeled IS injected, the excess heavy labeling reagents in the sample matrix label the remaining 0.25% of unlabeled peptide. This effect is undetectable at low unlabeled peptide concentrations, but becomes significant at high concentrations as 0.25% of the unlabeled peptide concentration approaches the heavy labeled IS concentration. For example, 0.25% of 400 nM unlabeled peptide yields 1 nM unreacted peptide, which if labeled with heavy labeling reagents, will double the detected IS concentration. While increasing the heavy labeled IS concentration would reduce the nonlinearity effect observed over the analyzed concentration range, this would only mask the true problem of untargeted labeling. To resolve this issue, a method to remove the heavy labeled peptide from the heavy labeling reagents prior to injection would be needed.

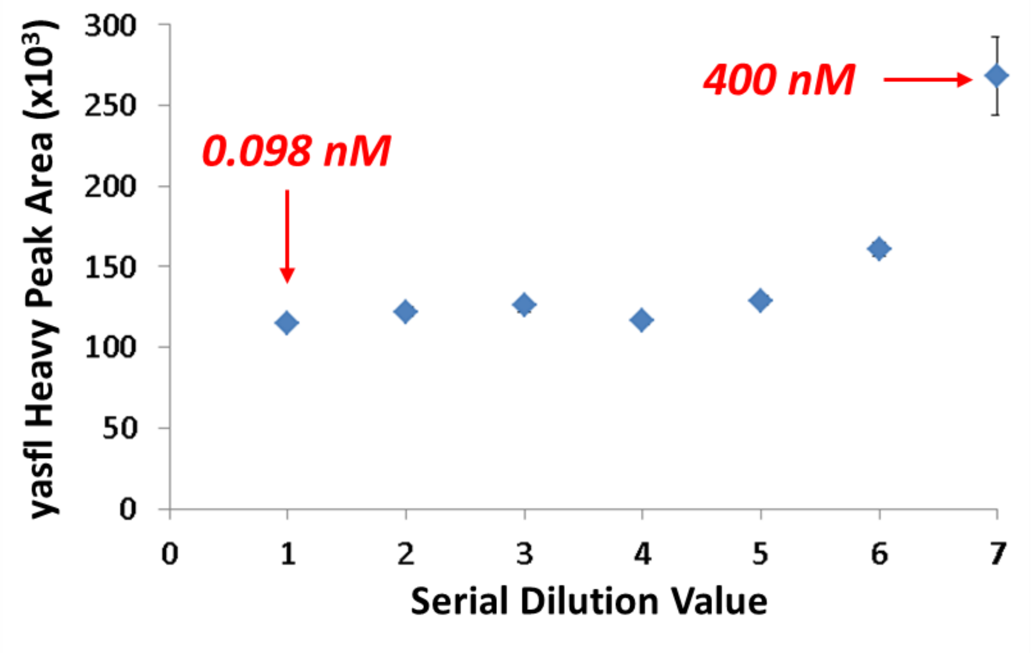

Figure 28. Plot of measured yasfl peak area as a function of the serial dilution value obtained using the original offline heavy labeling procedure without extraction. Serial dilution value is an arbitrary value assigned to each unlabeled peptide concentration through a 1:4 serial dilution of standards. A value of 1 corresponds to the lowest concentration (98 pM) and a value of 7 corresponds to the highest concentration (400 nM). The increasing heavy peak area trend starting between serial dilution value 5 (25 nM) and 6 (100 nM) indicates erroneous heavy labeling of unreacted peptide after the online light labeling procedure. Error bars indicated SEM values where n=3.

To resolve undesired heavy labeling of the dialysate, the final concentration of peptide within the offline heavy labeling procedure was varied from 3.91 – 1019 nM through 1:4 serial dilution. A calibration curve was then constructed in order to later calculate the concentration of heavy labeled peptide following extraction, and to monitor ratios of unlabeled to heavy labeled peak areas. The latter is important in order to ensure the yield of the offline labeling reaction. In all concentrations, over 99.9% of peptide was labeled. The most concentrated sample (1019 nM) was then selected for extraction using Pierce C_{18} pipette tips described above, yielding a 40 nM stock solution of heavy labeled peptide in LC-MS grade water following dilution. Repeating the analysis of unlabeled peptide (shown in Figure 28) with this purified heavy labeled solution, yielded improved results with no effect on measured yasfl heavy peak area as the unlabeled peptide concentration analyzed increases (Figure 29).

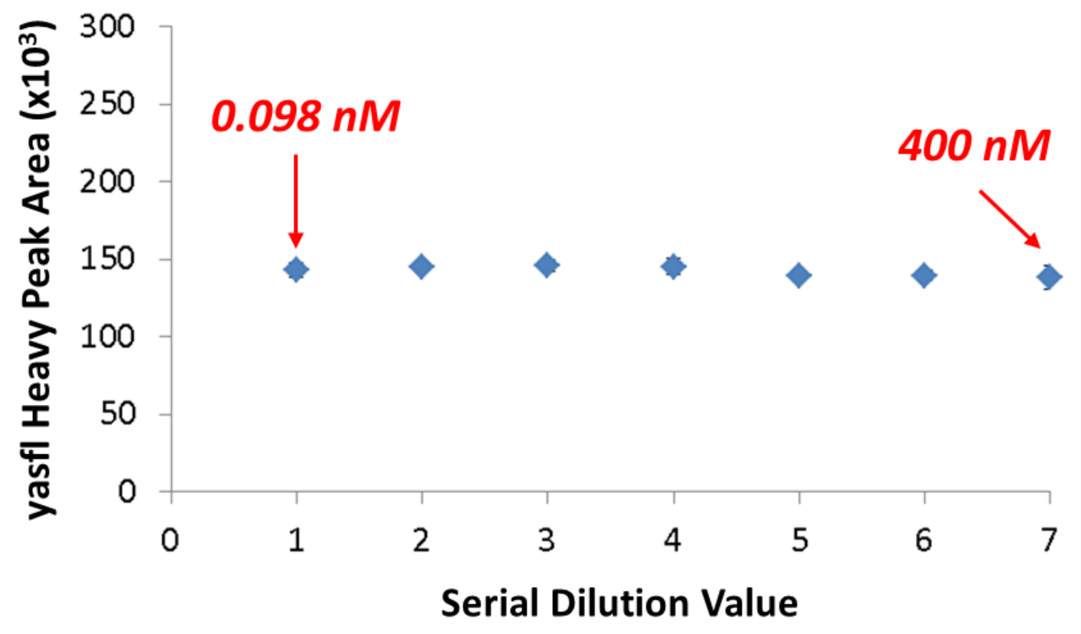

Figure 29. Plot of measured yasfl peak area as a function of the serial dilution value obtained using the new offline heavy labeling procedure which includes ZipTip extraction. Serial dilution value is an arbitrary value assigned to each unlabeled peptide concentration through a 1:4 serial dilution of standards. A value of 1 corresponds to the lowest concentration (98 pM) and a value of 7 corresponds to the highest concentration (400 nM). No difference was observed for heavy peak area across the peptide concentrations analyzed indicating no erroneous heavy labeling of unreacted peptide after the online light labeling procedure. Error bars indicated SEM values where n=3.

4.3.2 Calibration Curve for yasfl

Alongside implementing the purification step for the heavy labeled internal standard, the HPLC configuration was modified (described in detail in Section 4.2.6). Using the previous setup, the column was placed directly in line with the LTQ-XL ion source. In order to prevent excess reagents from the labeling procedure or salts present in the aCSF matrix from entering the ion source, the researcher would have to physically move the column away from the source prior to elution for each injection. In order to increase automation for this study, another valve was added that would control which pump controlled flow through the column. The analytical pump would always direct flow through the PicoTip emitter positioned in line with the ion source to prevent clogging of the 10 μm outlet. The loading pump, in line with the autosampler, would control peptide and labeling reagent loading at low organic mobile phase compositions. All eluent through the column during these stages were directed to waste. During the peptide elution stage, the valve would be switched, directing flow from the analytical column at high organic mobile phase composition through the column, to elute the labeled peptide for MS/MS analysis. Samples could now be loaded into the autosampler and analyzed overnight.

With these changes implemented, a calibration curve was constructed to validate the new procedure. A series of peptide concentrations ranging from 0.098 – 400 nM were made for LE, GGFL, yaGfl, and yasfl through 1:4 serial dilution in aCSF. The purified heavy labeled IS concentration was also increased to 4.0 nM. The calibration curve for yasfl is displayed in Figure 30. Calculated slope and intercept values (±95% CI) are displayed in Table 8. For all peptides analyzed, the calibration curve displayed linearity over the entire concentration range.

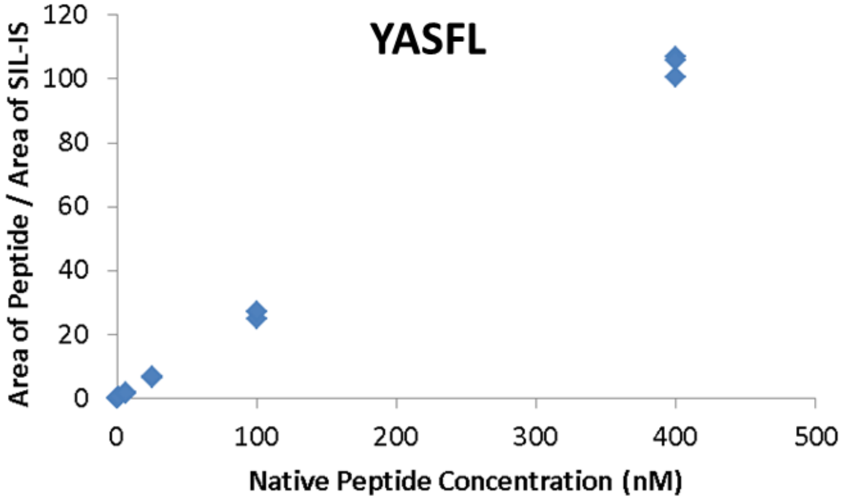

Figure 30. Calibration curve obtained using a serial dilution of yasfl in aCSF. The relative peak area of the y-axis corresponds to the ratio of the light-labeled peptide concentration prepared by serial dilution to the heavy labeled internal standard at a known concentration (4 nM).

Table 8. Calculated slope and intercept (±95% CI) for GGFL, LE, yaGfl, and yasfl

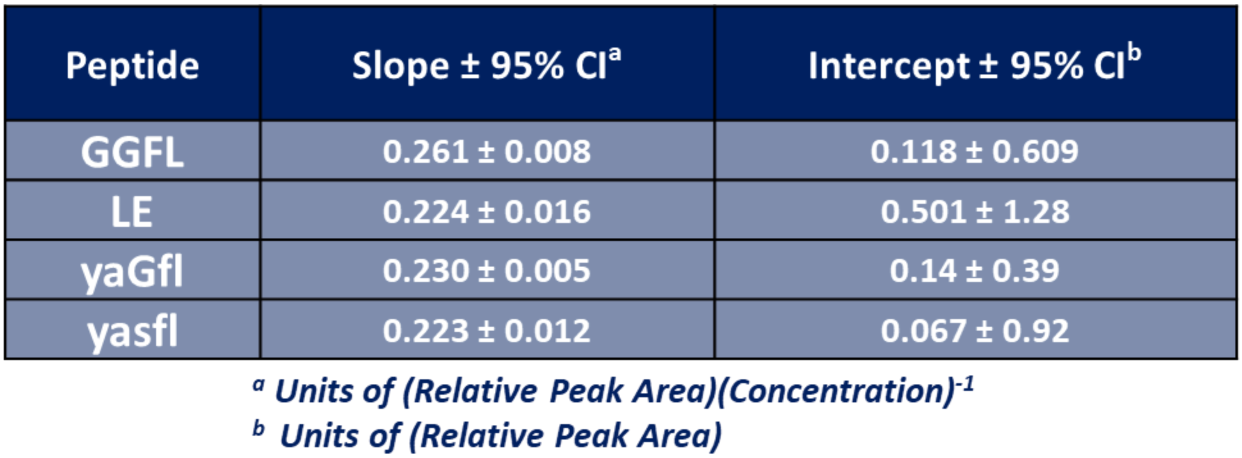

Peptide	Slope ± 95% CI[a]	Intercept ± 95% CI[b]
GGFL	0.261 ± 0.008	0.118 ± 0.609
LE	0.224 ± 0.016	0.501 ± 1.28
yaGfl	0.230 ± 0.005	0.14 ± 0.39
yasfl	0.223 ± 0.012	0.067 ± 0.92

[a] *Units of (Relative Peak Area)(Concentration)$^{-1}$*

[b] *Units of (Relative Peak Area)*

4.3.3 Retrodialysis of yasfl

The non-native pentapeptide, yasfl, was used recently as an internal standard for the determination of neuropeptides in brain dialysates (Wilson et al).[169, 170] We are aware of only one known peptidase, found in the gut of a marine mollusk, that can hydrolyze a peptide containing a D-amino acid. Thus, to the best of our knowledge, yasfl is neither a substrate for any metabolic enzyme present in the brain nor a ligand for any receptor or transporter. Therefore, it is a suitable solute for examining the effects of diffusion in the dialysis membrane and the surrounding tissue on microdialysis-based measurements.

The concentration of a solute in the dialysate at the outlet of a microdialysis probe may have two contributions, one from solute recovered from the external medium (the probe's surroundings) and one from solute delivered by retrodialysis but not extracted into the external medium:[32]

Equation 11

$$C_{out} = R \cdot C_{ext} + (1 - E) \cdot C_{in}$$

where C_{out} is the solute concentration at the probe outlet, C_{in} is the solute concentration at the probe inlet (also the retrodialysis concentration), C_{ext} in the solute concentration in the external medium, R is the recovery fraction, and E is the extraction fraction. Rearranging Eq. 11 gives the equation for the concentration-differences plot:

Equation 12

$$C_{in} – C_{out} = E \cdot C_{in} – R \cdot C_{ext}$$

which has a slope of E and a y-intercept of - R · C_{ext}, the inverse of the solute concentration when C_{in} is zero, so-called conventional microdialysis. Equations 11 and 12 apply to the simple case that E is a constant, as expected for a diffusion-controlled solute such as yasfl.

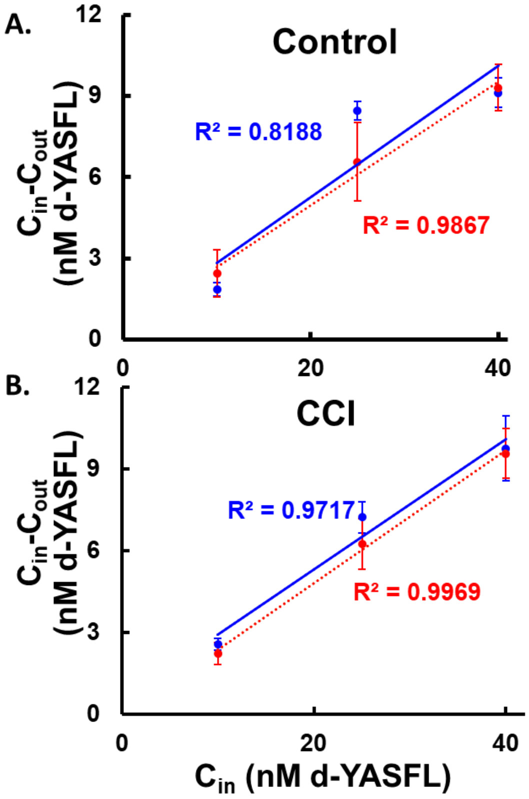

Figure 31. Concentration-difference plots for D- yasfl in A) control rats (n=3) and B) rats injured by CCI (n=5) on day 1 (in blue) and day 7 (in red). Data points are means ± SEM. There were no significant differences among the slopes of the lines as determined by linear regression (ANOVA, p = .9872).

Figure 31 reports concentration-differences plots for yasfl in injured and control rats on days 1 and 7. The E values were determined by linear regression. There were no significant differences in yasfl's E values among the four experimental conditions. The consistency of yasfl's E values confirms that solute diffusion in the dialysis membrane and surrounding tissues undergo no detectable changes due either to the elapsed time since probe insertion or the presence of CCI injury. Thus, Figure 31 confirms that potential confounders, such as blockage of the pores of the membrane and surrounding tissue, do not contribute to the glucose decline after CCI.

4.4 Conclusions

In this work, we have confirmed that microdialysis membrane integrity is not the source of glucose decline observed in animal models following traumatic brain injury through CCI. These results were obtained through the retrodialysis of a non-native peptide, yasfl, and accurate quantitation in the collected dialysate using capillary LC-MS/MS. No significant difference was observed between the calculated extraction fraction between day 1 and day 7 after probe implantation or between the control and CCI groups. Improvements to the chromatographic procedure were made with the goal of:

1) Eliminating untargeted labeling of unreacted peptide during the online demethylation process.
2) Increase sample analysis efficiency by modifying HPLC column and pump configuration to automate the sample cleanup process on-column.

With no evidence of microdialysis probe failure, these results indicate the glucose decline observed in rats injured by CCI is biologically relevent. Furthermore, the lack of observed decline in control animals not injured by CCI indicates a link between the glucose decline and TBI. This study illuminates additional information of TBI's effect on the brain, increasing the collective knowledge available to further develop methods for treatment.

5.0 Development of Electroosmotic Perfusion External Microdialysis Sampling Probe Design – Simulation and Experiment

5.1 Introduction

Ectopeptidases are transmembrane proteins whose catalytic domains face the extracellular space, and are responsible for controlling the local activity of neuropeptides through chemical transformation.[171] Unlike neurotransmitters, regulatory mechanisms involving neuropeptides are primarily controlled by degradation reactions catalyzed by ectopeptidases rather than reuptake mechanisms by neurons.[172] These degradation mechanisms can initiate a multitude of effects as downstream hydrolysis products can influence other domains of physiology than their parent peptide. Dysregulation of ectopeptidases has been linked to a number of disease states, including multiple sclerosis[173-175], rheumatoid arthritis[176, 177], and HIV[178]. Thus, obtaining a deeper understanding of ectopeptidase activity and its regulation is important as they emerge as viable therapeutic targets.[179, 180] However, gaining information about enzymatic activity *in vivo* is challenging due to the lack of approaches available for study.[62]

Studying ectopeptidase activity using natural substrates requires the ability to sample and quantify extracellular concentrations of peptide substrates and hydrolysis products *in vivo*. Sampling methods commonly utilized for probing the extracellular environment were covered extensively in Section 1.5. To summarize, push-pull perfusion (PPP)[67, 181-183] benefits from high spatial resolution of sampled tissue domains and control of tissue residence time. However, when online analysis is desired to reduce solute loss due to sample handling, the low nanoliter-per-minute flow rates associated with PPP are difficult to manage. Microdialysis (MD)[76] , although well-suited for online analysis with flow rates typically within the microliter-per-minute range[184], lacks the control of residence time. Substrates and inhibitors can be locally introduced to the tissue surrounding the probe through retrodialysis[185], but reuptake is primarily controlled through passive diffusion.[185, 186]

Recently, our lab has developed a sampling technique called electroosmotic perfusion-microdialysis (EOP-MD) to study enzymatic activity in vivo.[170] This method is capable of precise control of substrate/inhibitor perfusion flux to control residence time in the tissue and providing manageable sample volumes for online analysis using continuous microdialysis collection. Direct laser writing[187-190] was utilized to manufacture a device with an ability to control the tissue perfusion through electroosmotic flow. A dual-channel design allowed for the perfusion of substrate and substrate + inhibitor within the same rat using a single tissue implantation. A solid support ring allowed for MD probe placement roughly 200 µm away from the perfusion orifice. Combined with capillary LC-MS^2 detection and online isotopic labeling, quantitative estimates of substrate-to-product conversions were obtained for leu-enkephalin (LE) hydrolysis *in vivo*. Through the perfusion of HFI-419, a selective inhibitor of insulin regulated aminopeptidase IRAP[191], dose-dependent inhibition of LE hydrolysis were observed within in a rat neocortex.

The previous design required the implantation of the MD probe into the fragile brain tissue. This process is known to cause penetration injuries affecting the reliability of the information obtained for long-term studies,[155-160] Although these effects can be mitigated through the use of dexamethasone-enhanced microdialysis[82, 160, 161, 165-167], reducing the size of implantable devices is desirable to relieve additional strain on the sampled tissue. Also, although directional substrate flow from the perfusion tip to the MD probe can be achieved, the microdialysis probe samples the ECS adjacent to the entire circumference of the membrane. Thus, the signal observed is "diluted" from the MD probe hemisphere facing away from the perfusion tip, contributing to long times to reach steady state following initiation of electroosmotic flow.

In this work, we have used direct laser writing to fabricate an electroosmotic perfusion-external microdialysis (EOP-EMD) device to address these limitations. Both tissue perfusion and collection are controlled using electroomostic flow through minimally invasive implanted tips, eliminating the need for the MD probe to be implanted within the tissue. Instead, collected sample is transported to an external reservoir outside of the brain housing the microdialysis probe. We demonstrate the utility of sampling in this manner through simulation guided experiments using COMSOL Multiphysics and *in vivo* testing. Finite element models for both the EOP-MD and EOP-EMD devices were developed to study fluid flow and solute transport within the system. Comparison of *in vivo* results and simulations was also carried out to validate the model parameters. Not only do the models provide a platform to directly contrast the two designs, but they introduce a foundation to study enzymatic activity quantitatively demonstrated through tissue residence time calculations. Faster times to steady state following the induction of EO flow compared to the previous EOP-MD design was observed during *in vivo* testing, allowing for more perfused solutions per animal. These demonstrated improvements represent a more efficient, less invasive approach to study the neurochemical processes within the brain, including enzymatic activity. Combined with the accompanying FEM COMSOL models, quantitative information can be obtained.

5.2 Experimental

5.2.1 Direct Laser Writing of the EOP-EMD Probe Body

The EOP-EMD device consists of six major components: (1) perfusion channels, (2) waste reservoir, (3) MD sampling chamber, (4) tip support, (5) perfusion tip, and (6) the collection tip. These components are labeled in Figure 32 and 33A-B and include colorized liquid channels. Two perfusion channels combine to form one outlet at the perfusion tip. The collection tip inlet is offset vertically by 250 µm from the collection tip to maximize the volume of sampled tissue not in contact with the probe. The horizontal distance between the perfusion and collection tip is 100 µm, corresponding to a distance of approximately 270 µm between the center of each orifice. The outer diameter of both the perfusion and collection tip is 90 µm, with 50 µm internal channel diameters. A tip support connects the upper portion of the perfusion and collection channels to prevent tip bending during the manufacturing and tissue implantation process. This tip support has a thickness of 10 µm, with the lower 0.1 mm forming a wedge to a final thickness of 1 µm. The conical portion terminating the perfusion and collection tips were designed to minimize penetration injury with an opening angle of 20°.[192] The collection channel leads to a cylindrical MD sampling chamber (height = 1.35 mm, diameter = 290 µm). This MD sampling chamber also connects to a waste reservoir (88 nL) to prevent vacuum formation. The overall dimensions of the device used in the simulations and experiments are 0.965 mm (W) x 0.950 mm (L) x 3.71 mm (H).

The COMSOL Multiphysics geometry was exported to Solidworks and printed by 3D direct laser writing (Nanoscribe Photonic Professional, GT) with IP-S resist. Two-photon polymerization of the IP-S resist was used for printing by a femtosecond pulsed laser at 780 nm. The tip length can be modulated to match the needs of the researcher to probe the desired brain region. This is demonstrated in Figure 34A-B displaying images taken with a ZEISS Smartzoom Microscope (Jena, Germany) of probes printed in a 1.25 mm and 2.25 mm tip length configuration. For the work presented here, all simulations and experiments use the 1.25 mm configuration.

The device is designed to be implanted into the brain to a depth up to the length of the collection tip, 1.25 mm in the case of the configuration used herein. The dimensions of the perfusion and collection tips, tip support, and tip entrance angle have been formulated to minimize the negative effects of penetration injury. Rather than inserting the MD probe into the tissue, it is housed externally within the MD sampling chamber. By applying a current to the perfusion inlet and grounding the MD inlet, electroosmotic flow is used to perfuse the tissue directionally toward the collection channel. The sampled solution from the ECS then travels through the collection channel to the MD sampling chamber. The volume within this chamber is continuously filled with this solution, and collected analytes diffuse through the MD membrane for analysis.

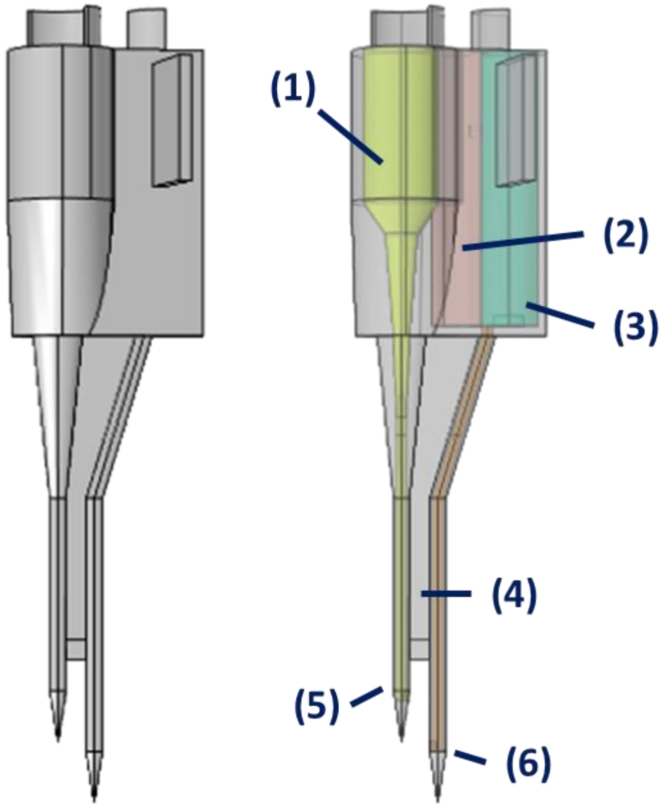

Figure 32. Geometry of the new EOP-EMD design created within COMSOL Multiphysics. The left figure displays the outer solid support of the device while the transparent image on the right displays the major device components indicated by numbers and the fluidic channels indicated by color. Major components: 1 – Perfusion channels, 2 – waste reservoir, 3 – MD sampling chamber, 4 – Tip support, 5 – Perfusion Tip, 6 – Collection tip. The fluidic channels consist of the perfusion channels (yellow), collection channel (orange), MD sampling chamber (cyan), and the waste reservoir (red).

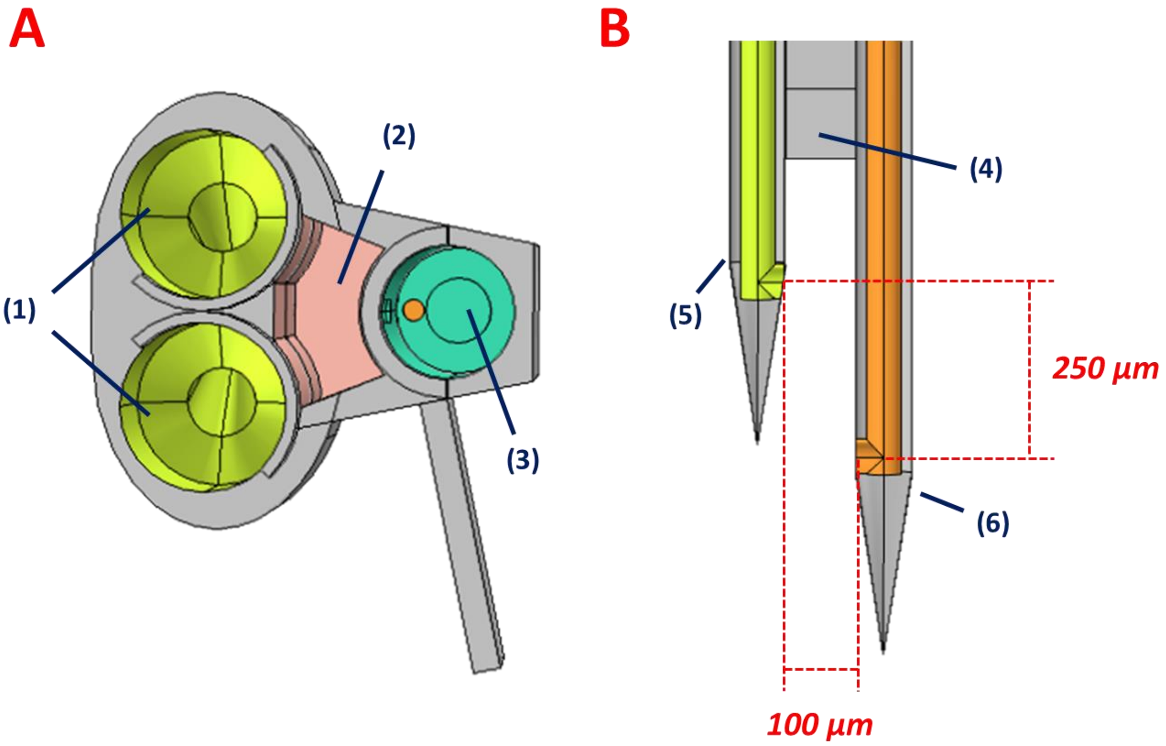

Figure 33. A - Top-down image of the EOP-EMD design; B – Enhanced image of the perfusion and collection tips. Major components: 1 – Perfusion channels, 2 – waste reservoir, 3 – MD sampling chamber, 4 – Tip support, 5 – Perfusion Tip, 6 – Collection tip. The fluidic channels consist of the perfusion channels (yellow), collection channel (orange), MD sampling chamber (cyan), and the waste reservoir (red).

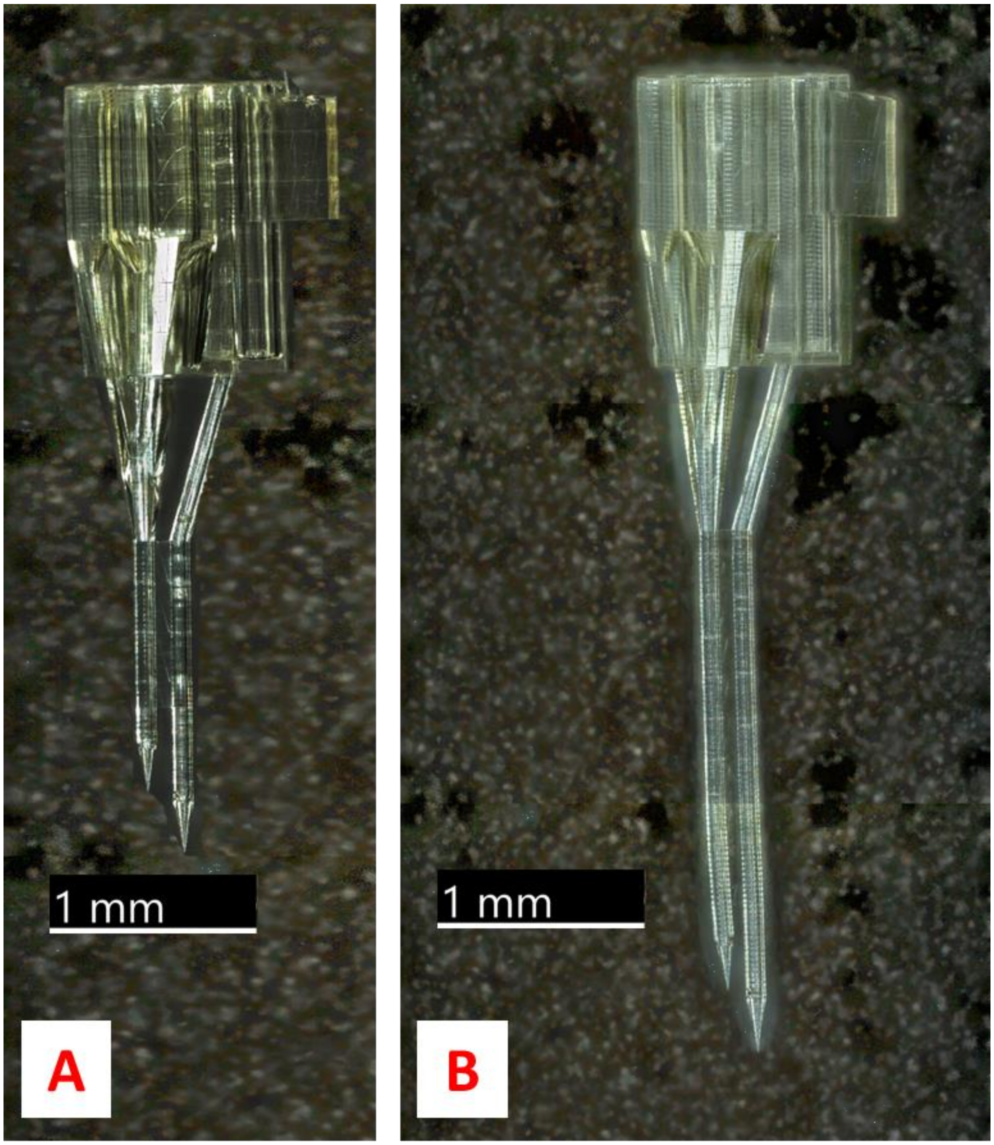

Figure 34. Images of the EOP-EMD design in the 1.25 mm probe (A) and the 2.25 mm (B) probe tip configuration. Images were captured using a ZEISS Smartzoom digital microscope.

5.2.2 Finite Element Modeling in COMSOL Multiphysics

The simulations for both the previously published probe design (EOP-MD) and the new design (EOP-EMD) were performed in COMSOL Multiphysics, version 5.6. Physics for electroomostic transport through the tissue were based on previously published models demonstrating electroosmotic push-pull perfusion of mammalian tissue.[193, 194] Three dimensional geometries representing the tissue, probe solid support, fluidic channels, and microdialysis probe were formed in COMSOL Multiphysics using simple shapes and parametric curves for both models. The probe solid support volume was subtracted from the tissue volume using Boolean operations. In the case of the EOP-MD model, the upper volume of the probe above the inlet capillary was subtracted from the tissue as well. Both the tissue and the semipermeable microdialysis membrane were programmed as homogenous porous materials. The "Electric Currents" physics module was used to calculate the potential in the tissue resulting from the applied current. The "Free and Porous Media Flow" module was used to calculate fluid flow rates, while solute transport was controlled through "Transport of a Diluted Species in a Porous Media" module. A description of the model domains is shown in Figure 35 and 36. All boundary conditions and material parameters are reported in the Supporting Information.

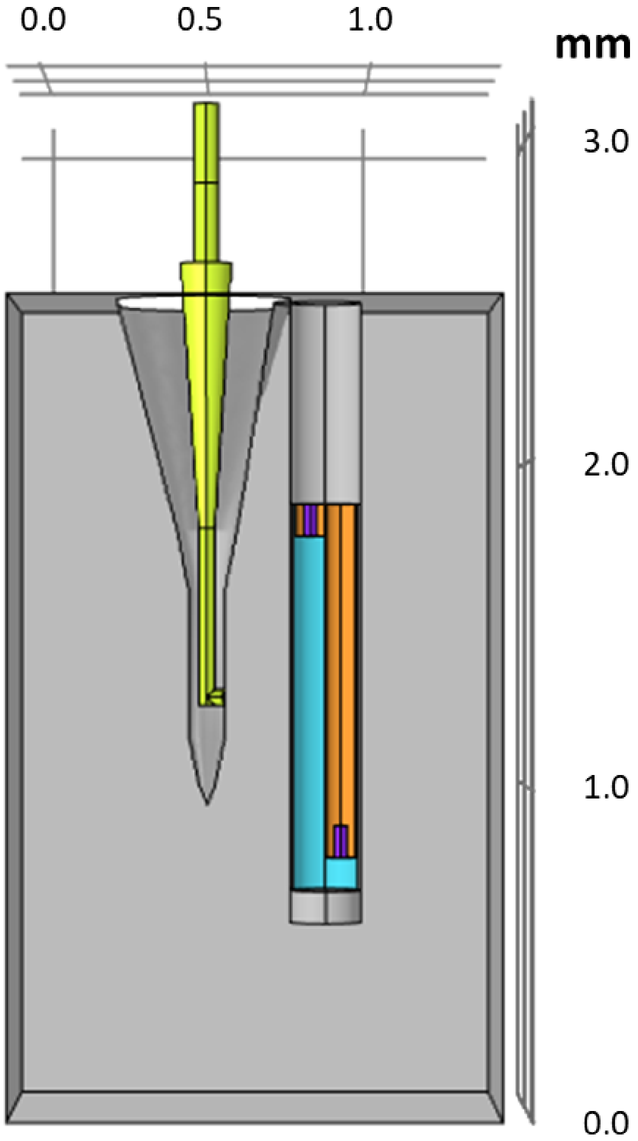

Figure 35. 3D geometry of the EOP-MD model created in COMSOL Multiphysics(v5.6). A XZ cut plane (Y=0.0 mm) of the device shows the fluidic channels containing the perfusion solution (yellow). The microdialysis probe (220 µm o.d., 200 µm i.d.) is placed 205 µm away from the perfusion orifice. This distance correlates to the MD probe being placed vertically. The MD probe consists of the probe lumen (cyan), outer capillary cylinder (orange), and inner capillary cylinder (purple). Both the perfusion inlet and MD outlet cylinder lengths are reduced to save computation time, and a pressure boundary condition is added to correct for the backpressure generated from the removed capillary length.

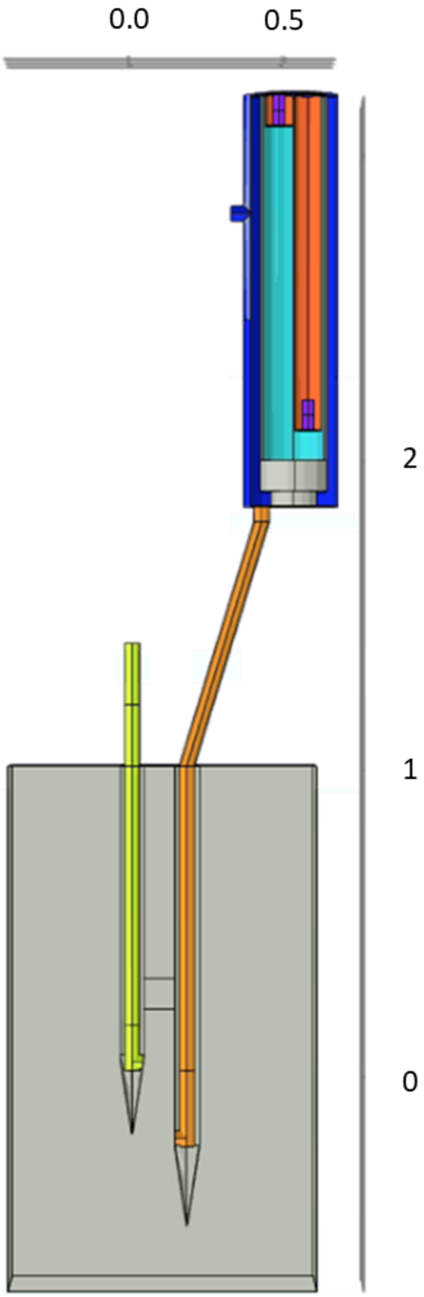

Figure 36. 3D geometry of the EOP-EMD model created in COMSOL Multiphysics(v5.6). A XZ cut plane (Y=0.0 mm) of the device shows the perfusion channel (yellow) and the collection channel (light orange). The MD probe (220 µm o.d., 200 µm i.d.) is placed within a 290 µm diameter cylindrical reservoir (blue). The MD probe consists of the probe lumen (cyan), outer capillary cylinder (dark orange), and inner capillary cylinder (purple). Both the perfusion inlet and MD outlet cylinder lengths are reduced to save computation

time, and a pressure boundary condition is added to correct for the backpressure generated from the removed capillary length.

5.2.3 EOP-MD Probe Assembly and Generating Electroosmotic Flow

The procedure to assemble and generate electroosmotic flow using the new EOP-EMD device followed the procedure outlined in detail in Wilson et al.[170] unless stated below. To fill the collection channel, a 2 cm segment of 75 μm i.d. x 150 μm o.d. fused silica capillary was threaded into a 5 cm segment of 200 μm i.d. x 360 μm o.d. capillary. The interface was sealed with a drop of 2-ton epoxy (Devcon) and allowed to cure for 2 hours at room temperature. The 75 μm i.d. x 150 μm o.d. segment was then cut to a length less than the height of the MD chamber (< 1.35 mm). Finally, the 200 μm i.d. x 360 μm o.d. capillary was connected to a syringe using a Teflon union, and the 75 μm i.d. x 150 μm o.d. segment was inserted into the 290 μm diameter MD chamber. By applying force between the epoxy and the top surface of the MD sampling chamber, the chamber can be temporarily sealed in order to fill the collection channel with modified Ringer's solution using the syringe. This process is demonstrated below in Figure 37.

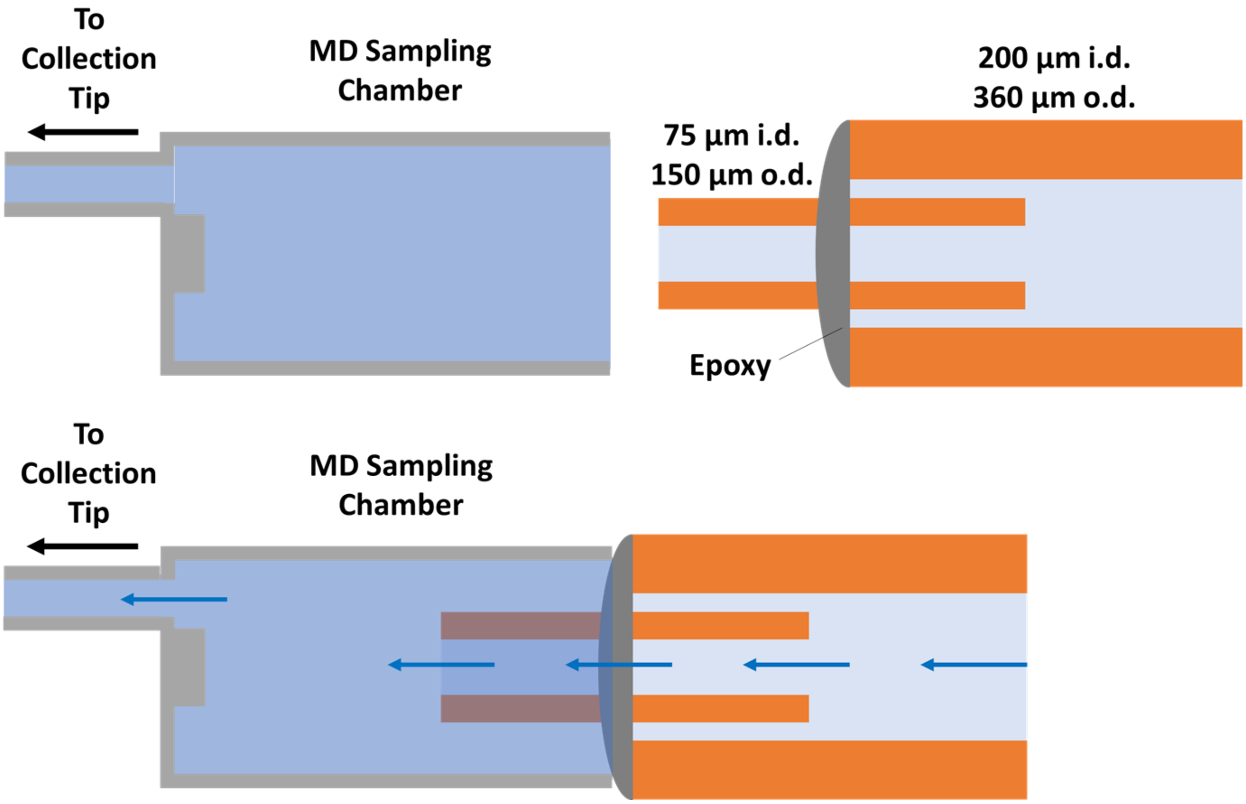

Figure 37. Filling procedure for the EOP-EMD collection channel tip. A 75 µm i.d. x 150 µm o.d. capillary is first threaded into a segment of 200 µm i.d. x 360 µm o.d. capillary. A small drop of 5-minute epoxy is then used to seal the end of the 200 µm i.d. capillary. To fill the collection channel tip, the 75 µm i.d. capillary is inserted into the MD sampling chamber. By applying force between the MD sampling chamber opening and the epoxy, the MD sampling chamber and collection channel tip can be filled using a syringe connected to the 200 µm i.d. capillary.

Microdialysis probes (1.0 mm between the inlet and outlet capillary ends, 0.1 mm space between the outlet and the epoxy tip) were constructed using hollow fiber dialysis membrane (Spectra-Por RC Hollow Fiber; MWCO = 13 kDA, 200 µm i.d., 220 µm o.d., Spectrum Laboratories Inc.; Rancho Dominguez, CA). Fused silica capillaries (40 µm i.d., 100 µm o.d.) were used as the probe inlet and outlet. Detailed instructions regarding probe construction were the same as previously described.[195]

5.2.4 Sample Preparation

A stock solution of 1.0 mM $^{D}Y^{D}A^{D}G^{D}F^{D}L$ (yaGfl) (Shanghai Royobiotech, Shanghai, China) was prepared by diluting the solid in a Modified Ringer's solution consisting of 148 mM NaCl (EMD-Millipore, Darmstadt, Germany), 1.2 mM $CaCl_2$ (EMD-Millipore), 2.7 mM KCl (Sigma-Aldrich), and 0.85 mM MgCl2 (Fisher Scientific, Fair Lawn, NJ) at pH 7.4. All solutions were then filtered using a 0.2 µm PES syringe filter (Corning Inc., Corning, NY) prior to use. To determine the limit of detection and linearity over relevant concentration ranges, a series of standards ranging from 1.56 – 100 µM were made through serial dilution.

5.2.5 Column Preparation

The method for making outlet frits for the 150 µm i.d. x 360 µm o.d. column blanks was followed the procedure outlined by Kennedy[142]. A 25% (v/v) solution of formamide (Acros, NJ) and Milli-Q water was diluted 1:1 with potassium silicate (Kasil, PQ Corporation, Valley Forge, PA). A 10 µL drop was then placed on a piece of Whatman filter paper (Whatman, UK, Cat No. 1822-025). The end of the column blank was dipped on to filter paper and placed in a Thermo Focus series GC oven set to 85 ºC for 12 hours. The Acquity CSH C_{18} 1.7 µm particles (Waters, Milford, MA) were slurried in 2-propanol at concentrations of 65 mg/mL. This was sonicated for 20 minutes before packing using the downward slurry method. A Haskel model DSF-150 pneumatic amplification pump (Burbank, CA) was used to pack the column at 20,000 psi for 20 minutes using methanol as the packing solvent, before allowing the pressure to dissipate naturally. The column was trimmed to final length of 10 cm.

5.2.6 Chromatography

The separation was achieved using a Dionex UltiMate 3000 Nano LC system (NCS-3200RS, Thermo Scientific, Germering, Germany) fitted with a micro-LC flow selector to deliver mobile phase. Channel A contained 0.1% trifluoroacetic acid (TFA, Sigma Aldrich) in Optima LC-MS grade water (Fisher Chemical) and channel B contained 0.1% TFA in LC-MS grade acetonitrile (Fisher Chemical). Isocratic elution at 20% channel B was used at a constant flow rate of 2 µL/min for the entirety of the experiment. The pump was connected to an externally mounted 6-port two-position Cheminert injection valve (C72x-669D, VICI Valco, Houston, TX) using a 750 x 0.100 mm nanoViper capillary. A 141 x 0.100 mm nanoViper capillary was used as a 1.1 µL sample loop. A 350 mm x 0.025 mm i.d. x 0.360 mm o.d. fused silica capillary was used to connect the outlet of the column to a Waters Acquity TUV fitted with a 10 nL nano flow cell (Waters Corporation, Milford, MA) set to 214 nm. An Atlas analog-to-digital convertor and Chromeleon version 6.8 software (Thermo) were used to acquire data at 100 Hz.

5.2.7 Animal Surgeries

All procedures involving animal surgeries were approved by the Institutional Animal Care and Use of Committee (IACUC) of the University of Pittsburgh. Male Sprague-Dawley rats (250-350 g, Hilltop, Scottsdale, PA) were anesthetized using isoflurane (5% induction, 2.5% maintenance), and placed in a stereotaxic frame (David Kopf Instruments, Tujunga, CA, USA). Animal placement was adjusted to flat skull by adjusting the incisor bar to reduce the dorsal measurement difference between lambda and bregma to less than 0.01 mm. Rats were wrapped in a heating blanket maintained at 37 °C. A craniotomy was performed over the prefrontal cortex

(PFC), before lowering the device slowly (10 μm/sec) into the PFC tissue (2.3 mm anterior and 3.0 mm lateral from bregma) to a final depth of 1.25 mm below dura. Aseptic technique was used throughout the experiment.

5.2.8 *In vivo* Measurements

Prior to implantation, the EOP-EMD device and the microdialysis probe were soaked in 70% ethanol (Decon, King of Prussia, PA) for 20 minutes. One perfusion channel was loaded with the 1.0 mM yaGfl in modified Ringer's solution while the other channel was loaded with modified Ringer's solution only. The MD chamber was filled with modified Ringer's solution before inserting the MD probe. Using a Harvard Apparatus PHD 4400 programmable syringe pump (Holliston, MA), the MD probe was perfused with modified Ringer's solution at a flow rate of 0.5 μL/min. Before tissue implantation, the fluidic channels of the device were checked for the presence of bubbles. The device was lowered into a solution of modified Ringer's, before connecting the perfusion channel and MD inlet silver electrodes to the current source (Model PS350, Stanford Research Systems Inc, Sunnyvale, CA). After 5 minutes of sustained current, the current was turned off and the device was lowered into the PFC. After one hour, a 15 μA current was applied to initiate the perfusion of the channel containing modified Ringer's. After 56 minutes following the start of perfusion, the current was terminated for the modified Ringer's perfusion channel and a 15 μA current was applied to the perfusion channel containing 1.0 mM yasfl in modified Ringer's. Current was modulated in step changes during the experiment, increasing to 30 μA at 112 minutes, increasing to 60 μA at 175 minutes, and decreasing to 30 μA again at 203 minutes. The current was turned off at 266 minutes after a leak was detected at the upper epoxied portion of the MD probe.

5.3 Results and Discussion

5.3.1 Assessing Device Design Performance *in silico*

The finite element model constructed for both probe designs is similar to previously published models[193, 194] constructed to assess electroosmotic flow through brain tissue. Electroosmotic flow in a porous media can be modeled through the “Electric Current” and “Free and Porous Media” modules, with an EO flow rate equal to:

Equation 13

$$U_{eo} = \frac{\varepsilon_w \zeta}{\eta} \frac{i}{\sigma_{el}}$$

where ε_w is the permittivity of water (F/m), ζ is the zeta potential (V), η is the dynamic viscosity (Pa s), i is the applied current (A), and σ_{el} is the conductivity of the electrolyte solution (S/m).[196] The zeta potential was set for the capillaries (ζ_{cap} = -46.5 mV)[197] and the tissue (ζ_{tissue} = -22.8 mV).[198] The permittivity of water was 7.1 x 10^{-10} F/m, the buffer conductivity was 1.79 S/m, and a dynamic viscosity of 8.9 x 10^{-4} Pa s was used corresponding to 25 °C. This can be used to calculate the electroosmotic velocity through the porous media where the volumeflow rate is divided by the total cross sectional area, yielding the equation:

Equation 14

$$U_{eo} = \frac{\varepsilon_w \zeta \varepsilon_p}{\eta \lambda^2} \frac{i}{\sigma_{el}}$$

where ε_p and λ^2 are the porosity and tortuosity of the media respectively. The tissue was modelled as a homogenous porous matrix with a porosity of 0.2[199] and tortuosity of 1.6[199] obtained from literature. The velocity profile with a set current of 15 μA is shown for EOP-MD (Figure 38) and EOP-EMD (Figure 39).

Both devices display directionality of flow toward the microdialysis probe (EOP-MD) or the collection channel (EOP-EMD) through the porous tissue. This is particularly distinct in the EOP-EMD model where a diagonal velocity gradient is observed at the z-direction midpoint between the perfusion and collection orifices. The EOP-EMD model also matches an observation made in previously published work[194] where the solution velocity increases approaching the collection capillary orifice. This effect is the result of the change in zeta potential mismatch between the tissue (-22.8 mV) to within the capillary (-46.5 mV). A negative pressure gradient is generated at the tissue/collection orifice, causing an increase in fluid velocity approaching the interface. In the EOP-MD model, this effect is average across the entire surface area of the microdialysis probe and is less distinct than in the EOP-EMD model.

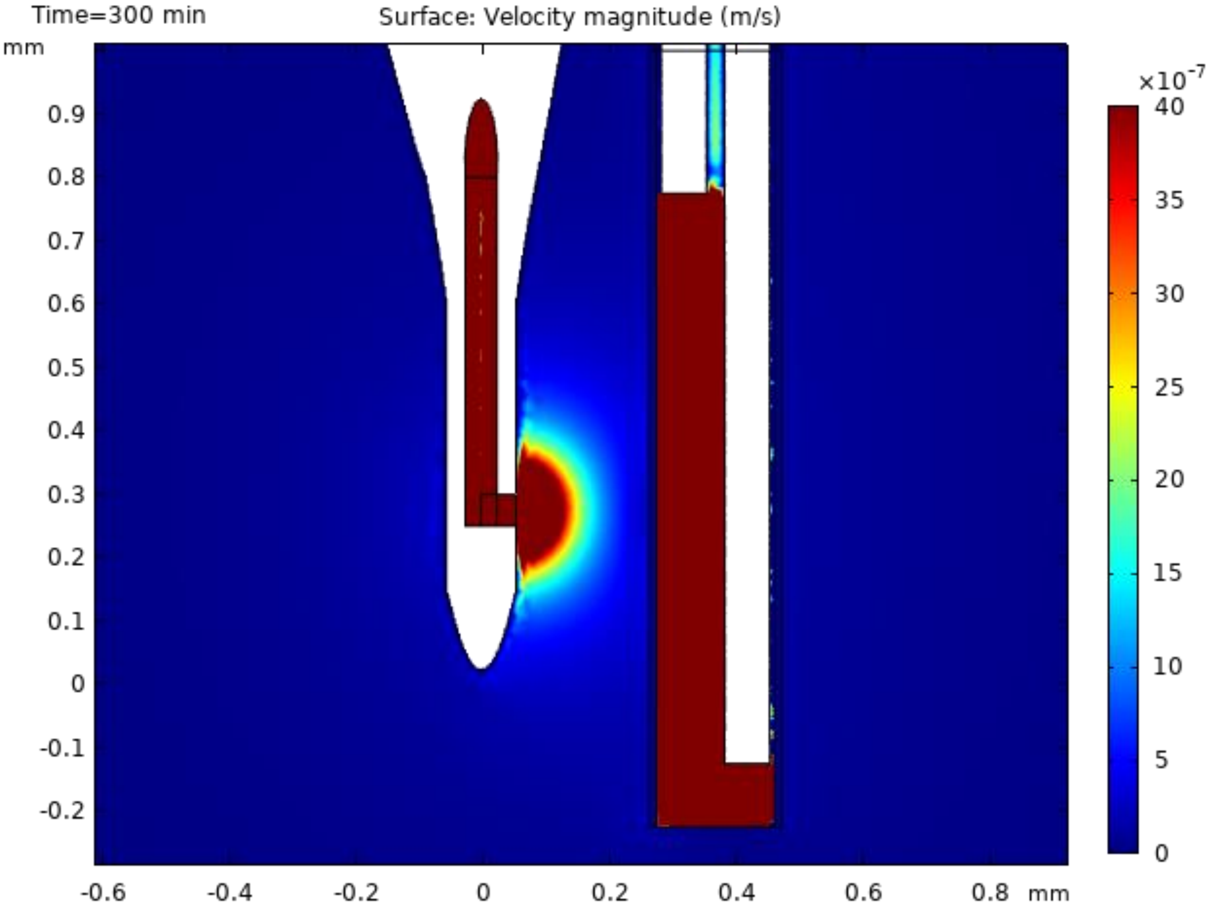

Figure 38. XZ plane velocity profile (Y=0.035 mm) for the EOP-MD model using an applied current of 15 µA. The cut plane corresponds to the center of the perfusion channel. In the EOP-MD device, the perfusion channel is offset from the MD probe capillaries, so the MD inner channels are not shown here. A maximum velocity of 4 µm/s was set for the color plot to illustrate the perfusion velocity gradient within the tissue.

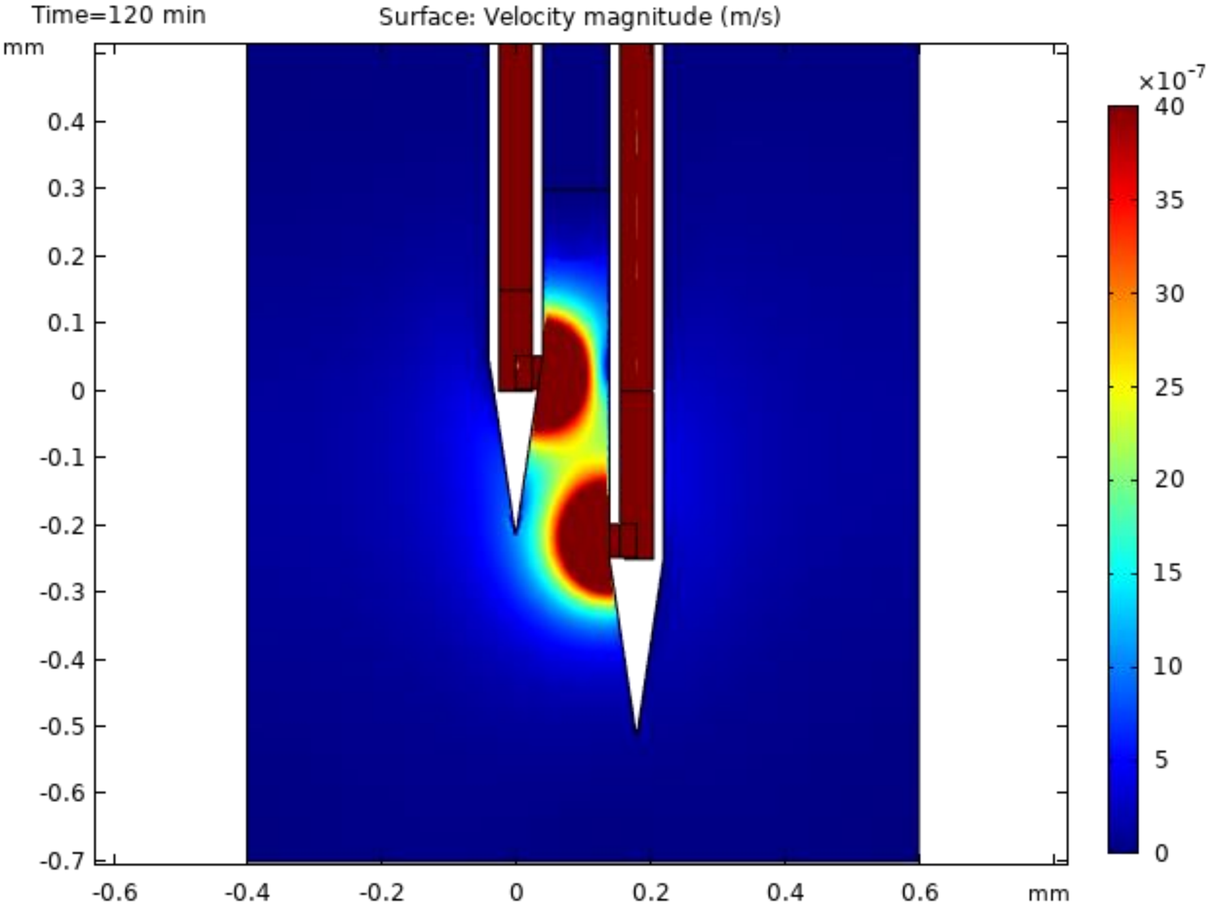

Figure 39. XZ plane velocity profile (Y=0.0 mm) for the EOP-EMD model using an applied current of 15 µA. The cut plane corresponds to the center of the perfusion channel. A maximum velocity of 4 µm/s was set for the color plot to illustrate the perfusion velocity gradient within the tissue.

The incorporation of the microdialysis probe into the simulations required accurate modelling of both the pressure driven flow within the microdialysis lumen and the peptide rate of diffusion through the semipermeable membrane. The microdialysis probe physics were identical for both models. The 10 µm membrane thickness was modelled as a homogenous porous material similarly to the tissue. The microdialysis inlet was set to a fully developed flow of 8.33 x 10^{-12} m^3/s, equivalent to 0.5 µL/min in the 40 µm i.d. capillaries. The inlet and outlet capillaries were cut to a total length of 0.1 mm to reduce the meshing volume saving computation time. To account for the outlet tubing not included within the model, a pressure boundary condition is set at the MD outlet. This pressure is equal to the backpressure generated across the length of the removed capillaries at a flow rate of 0.5 uL/min calculated using the Hagan-Poiseulle equation. The dimensions of the removed capillaries between the MD outlet and the sample loop were 49.9 x 0.04 mm, 1000 x 0.1 mm, and 141 x 0.1 mm yielding a backpressure of 9.39 x 10^3 Pa at 0.5 µL/min. The inclusion of this backpressure is necessary for accurate predictions of solute transport because this backpressure will affect the total outward flux of fluid from the membrane lumen into the tissue. Details regarding the remaining boundaries and domains is provided within the Supplemental Information. The velocity profile for the MD probe is shown in Figure 40.

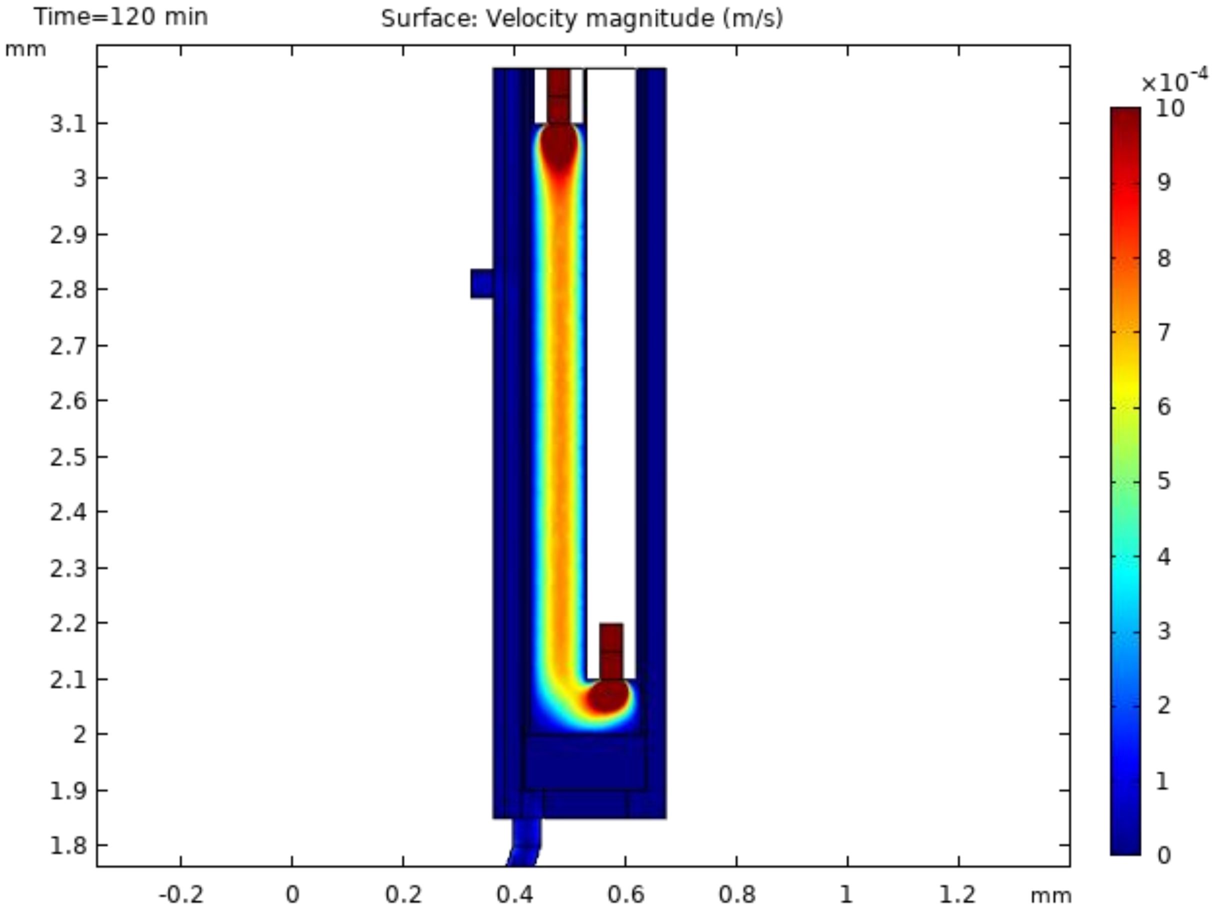

Figure 40. XZ plane velocity profile within the microdialysis probe. The cut plane was set to Y=0 with a flow rate of 0.5 µL/min.

The "Transport of a Diluted Species in a Porous Media" physics module was used to simulate solute transport within the model. Rates of diffusion through the membrane are dependent upon the solute diffusion coefficient and the tortuosity of the membrane with a relationship of D_{aq}/λ^2,[200] where D_{aq} is equal to the diffusion coefficient in free solution and λ is equal to the tortuosity of the membrane. To obtain an accurate tortuosity value for this specific membrane, the effective diffusion coefficient our group has previously measured for dopamine was used, corresponding to 1.37 x 10^{-10} m^2/s. Because these measurements were performed within living tissue at 37 °C, the diffusion coefficient was adjusted for 25 °C and compared to the diffusion coefficient for dopamine in free solution at 25 °C, 6.0 x 10^{-10} m^2/s.[201] This yields a membrane tortuosity value of 2.42. Diffusive flux (D_{flux}) across the membrane/tissue interface is affected by the membrane tortuosity and porosity with the relationship of:

Equation 15

$$D_{flux} = \frac{\phi D_{aq}}{\lambda^2}$$

where ϕ is equal to the porosity of the membrane. The porosity of the membrane was determined to be 0.2 based on microdialysis literature.[202, 203]

To compare the performance of the two device designs, a tissue perfusion of yaGfl was modeled at varied applied currents, and average MD outlet concentrations of collected peptide were calculated. The perfusion channel was programmed to contain 1000 μM yaGfl with an inflow boundary condition at the perfusion channel inlet set to the same concentration. This provides a constant infused concentration into the tissue. The volume average concentration within the 0.1

mm microdialysis outlet capillary was calculated every 2 minutes for a total of 120 minutes. The simulation was performed using three applied currents for each device: 15, 30, and 60 μA. The collected dialysate concentration as a function of time is shown in Figure 41 and 42 for the EOP-MD and EOP-EMD model respectively. The average of the concentration values for the last 20 minutes of the simulation (100-120 minutes) was defined as the steady state concentration. For the EOP-MD model, a steady state concentration of 5.944 ± 0.005 μM (mean ± SEM, n = 11) was calculated for 15 μA, 9.372 ± 0.007 μM (n=11) for 30 μA, and 13.581 ± 0.003 μM (n = 11) for 60 μA. For the EOP-EMD model, a steady state concentration of 10.572 ± 0.004 μM (n = 11) was calculated for 15 μA, 22.511 ± 0.010 μM (n=11) for 30 μA, and 38.370 ± 0.022 μM (n = 11) for 60 μA. The time to reach steady state concentration was then determined for each probe design. This was defined as the first time point corresponding to a dialysate concentration greater than 95% of the steady state concentration. For the EOP-MD device, the time to steady state was determined to be 58 minutes for 5 μA, 42 minutes for 30 μA, and 20 minutes for 60 μA., while the EOP-EMD model yielded 14 minutes for 5 μA, 10 minutes for 30 μA, and 6 minutes for 60 μA.

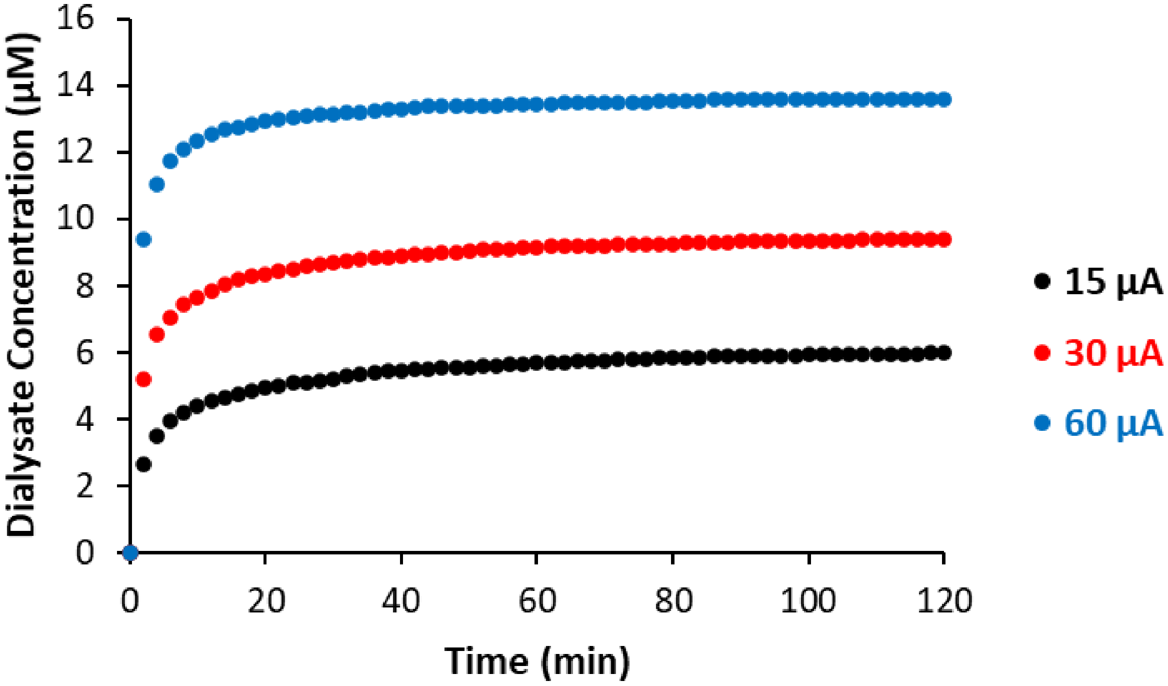

Figure 41. The yaGfl concentration (µM) measured in the dialysate as a function of time (min) and applied current for the EOP-MD design. Dialysate concentration values were measured by the volume average concentration of yaGfl in the microdialysis outlet capillary. The applied current was varied between 15 µA (black), 30 µA (red), and 60 µA (blue). For each case, the perfusion channel contained 1000 µM yaGfl.

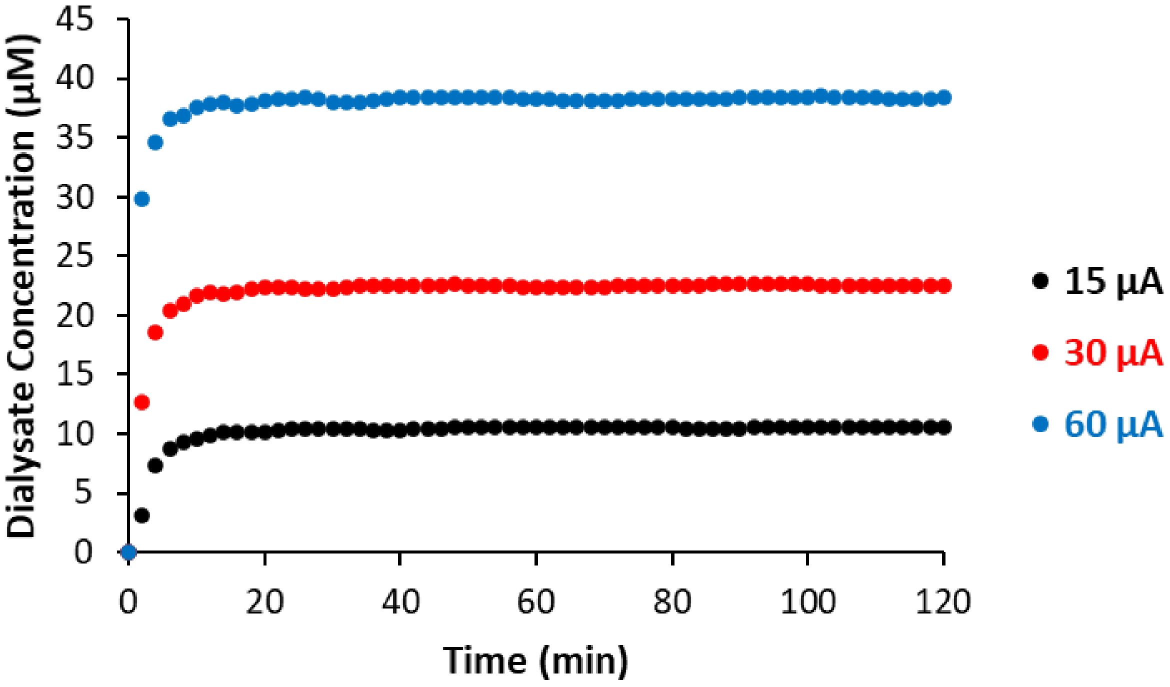

Figure 42. The yaGfl concentration (µM) measured in the dialysate as a function of time (min) and applied current for the EOP-EMD model . Dialysate concentration values were measured by the volume average concentration of yaGfl in the microdialysis outlet capillary. The applied current was varied between 15 µA (black), 30 µA (red), and 60 µA (blue). For each case, the perfusion channel contained 1000 µM yaGfl.

The results clearly illustrate the advantage of the new EOP-EMD device design over the previous EOP-MD. The average dialysate concentration is higher for the EOP-EMD design for each applied current, and the time required to reach 95% steady state concentrations is reduced dramatically when compared to the EOP-MD design. The most dramatic effect is observed at 15 µA, where the EOP-EMD design yields a 2.4-fold increase in signal and reduces the perfusion time required to reach steady state concentration by a factor of 4.1. Time required to reach steady state concentration is an important metric for device performance because it dictates the number of tissue perfusions that can be achieved using different solutions per experiment. Typical *in vivo* experiments using anesthetized rats have an upper time limit of about 8 hours, which includes the time to perform the craniotomy, probe implantation, and one hour waiting period following the probe implantation. With only approximately 6 hours remaining for tissue perfusion, decreasing the time to steady state concentrations when switching the infused solution or current increases the data density that can be achieved with a single experiment.

While careful consideration was taken to maintain reproducibility for the previous EOP-MD design, limitations in the manual assembly method left several avenues to introduce variability between devices. The two major routes for variability were differences in effective membrane length (the vertical distance between the inlet and outlet orifices of the MD capillaries), and the sampling distance (the horizontal distance between the perfusion orifice and the MD membrane surface). Both of these parameters affect the measured solute concentration in the dialysate, and these effects are illustrated using the EOP-MD model in Figures 55-58 within the supplemental information. Increasing the sampling distance from 90 to 205 μm results in a 25% loss in dialysate concentration. Decreasing the effective membrane length also has a negative effect on measured dialysate concentration where a reduction from 1.0 to 0.5 mm results in a 25% loss, and a reduction from 1.0 to 0.25 mm results in nearly a 50 % loss at 15 μA applied current. Because the MD probes are made in-house, effective membrane length can easily vary from the target length of 1 mm by ± 0.1-0.3 mm. All simulations for the EOP-MD design were performed with a sampling distance of 205 μm, but experimentally this can vary by ± 50 μm during probe construction. Additionally, the flexible MD probe can bend during tissue implantation leading to further deviation in sampling distance.

These avenues for variability were addressed in the EOP-EMD design to mitigate their influence on experimental reproducibility. While effective membrane length variability is still present in the EOP-EMD design, the effects are mitigated by placing the probe within the MD sampling chamber. Because the solute flows parallel to the length of the membrane, a vertical concentration profile is generated within the chamber, illustrated in Figure 43. This means that nearly 90% of the solute present within the sampling chamber has diffused through the membrane within the first 0.5 mm of the membrane, reducing the influence of MD probe variability. Variation in sampling distance was addressed in the design of the EOP-EMD device with the rigid solid support dictating the distance between the perfusion and collection orifice. The EOP tip support prevents the tips from bending both during manufacturing and implantation. The entrance angle of the tips of 20° also eases the resistive force of the tissue when lowering into the brain compared to the insertion of the flat tipped epoxy surface of the MD probe.

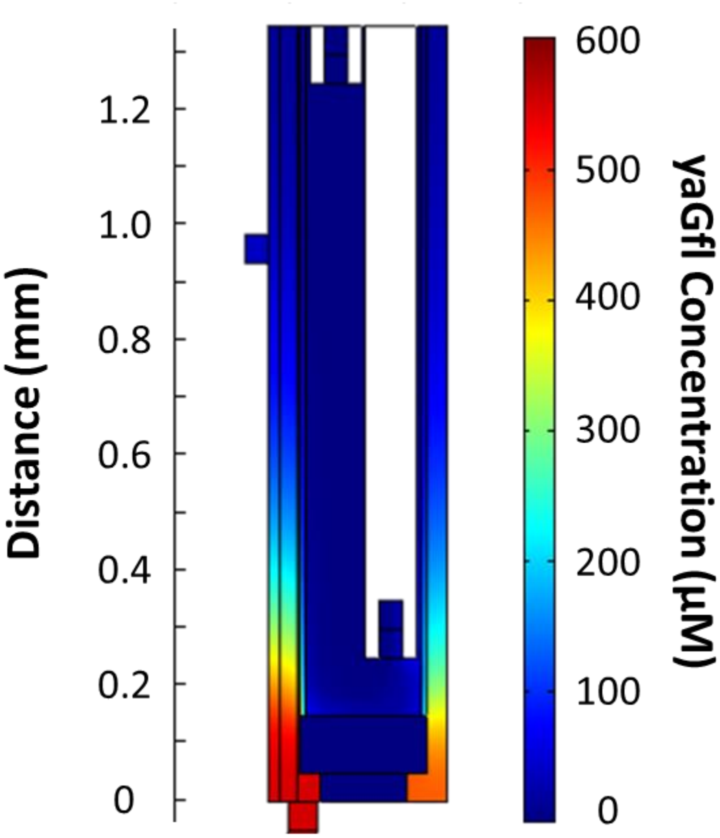

Figure 43. XZ cut plane (Y = 0.0 mm) displaying the yaGfl concentration gradient within the microdialysis sampling chamber. using the EOP-EMD model. The figure displays the yaGfl concentration (μM) after 120 minutes of 1.0 mM yaGfl infusion into the tissue with an applied current of 15 μA.

5.3.2 Simulated Determination of Substrate Residence Time

Accurate determination of residence time within the tissue is critical to obtain quantitative information regarding enzyme kinetics for peptide hydrolysis. While a given perfusion flux of substrate can be calculated, a concentration gradient within the tissue makes residence time very difficult to determine experimentally. Residence time is defined as the amount of time a given solute spends within the tissue. This time determines the duration the substrate is subjected to degradation events such as hydrolysis within the extracellular space. To explore the relationship between residence time and applied current for both the EOP-MD and EOP-EMD models, a method was developed to determine this parameter within the COMSOL Multiphysics.

In each model, a low volume portion of the perfusion channel near the outlet orifice was programmed to contain 1.0 mM yaGfl while the remainder of the perfusion channel contained only buffer. The inflow boundary condition at the perfusion inlet orifice was set to 0.0 mM yaGfl to ensure the initial pulse was the only introduction of substrate into the tissue throughout the simulation. The flux out of the tissue was calculated over 500 s at a frequency of 2 Hz for the applied currents of 15 and 30 μA. The calculation frequency was increased to 4 Hz for the applied current of 60 μA to increase the data density during the high flux rate increase within the first 15-25 s. Outward tissue flux (mol/m^2 s) was defined as the flux through the outer surface of the microdialysis membrane for the EOP-MD model and the flux into the collection orifice for the EOP-EMD model. Detailed descriptions of boundaries and domains are provided within the Supplemental Information. The peptide pulse into the tissue and subsequent collection is displayed at three different time points in Figure 44 and 45 for the EOP-MD and EOP-EMD models respectively, with an applied current of 15 μA in both cases.

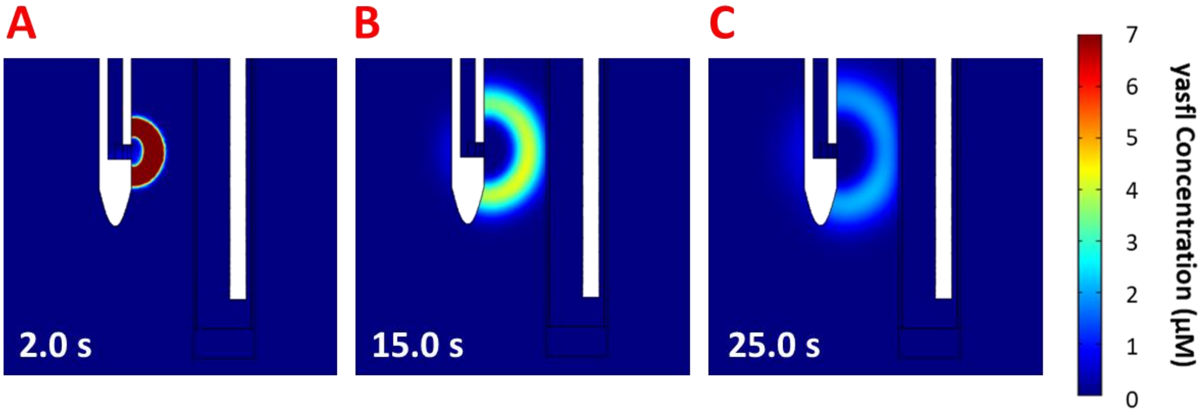

Figure 44. XZ cut plane (Y = 0.035 mm) displaying concentration (µM) of the 1.0 mM yaGfl pulse into the tissue from the perfusion tip using the EOP-MD model. The concentration within the tissue and microdialysis membrane is displayed at time points 2.0 s (A), 15.0 s (B), and 25.0 s (C), where time zero corresponds to the time that the 15 µA current was applied. The color plot indicates the concentration within the tissue, but a maximum concentration of 7 µM yaGfl was applied in order to scale the color to observe the band move throughout the tissue.

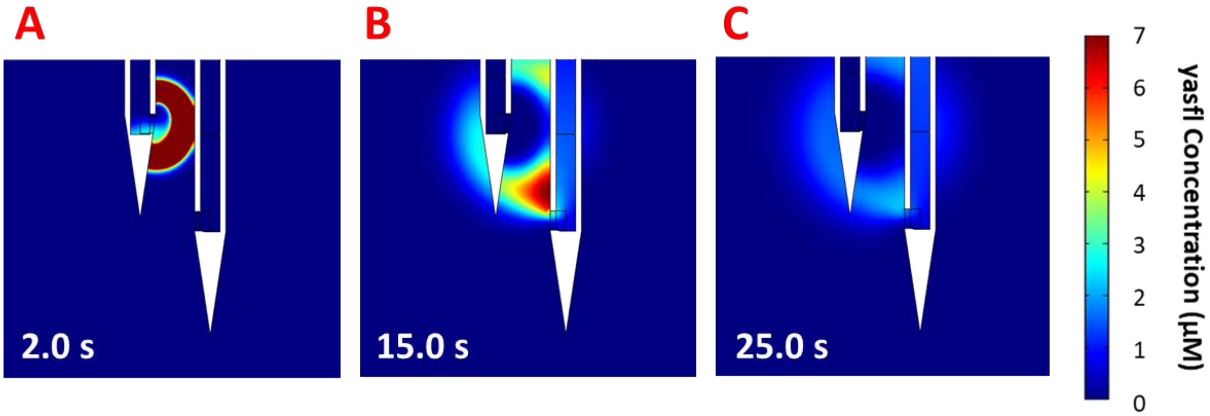

Figure 45. XZ cut plane (Y = 0.0 mm) displaying concentration (µM) of the 1.0 mM yaGfl pulse into the tissue from the perfusion tip using the EOP-EMD model. The concentration within the tissue and microdialysis membrane is displayed at time points 2.0 s (A), 15.0 s (B), and 25.0 s (C), where time zero corresponds to the time that the 15 µA current was applied. The color plot indicates the concentration within the tissue, but a

maximum concentration of 7 µM yaGfl was applied in order to scale the color to observe the band move throughout the tissue.

The outward tissue flux as a function of time for each applied current (5, 15, 30 and 60 µA) is shown in Figure 46 and 47 for EOP-MD and EOP-EMD models respectively. Residence time was defined as the first moment of each curve, with calculated values displayed in Table 9. In both models, residence time decreases as applied current increases. This is expected, as the electroosmotic velocity also increases with increasing applied current. The residence time is also shorter at each applied current for the EOP-EMD model relative to the EOP-MD model. This is an interesting result due to the difference of sampling distance between the two designs. The sampling distance for the EOP-MD design is dictated by the horizontal distance between the perfusion orifice and the MD membrane. For the EOP-EMD design, the sampling distance is dictated by the distance between the perfusion orifice and collection orifice. These values are 205 and 270 µm for the EOP-MD and EOP-EMD designs respectively. While the horizontal distance between the perfusion and collection channels is shorter for the EOP-EMD design (100 µm), the sampling distance is larger than the EOP-MD design due to the 250 µm vertical offset between the two channels. This result suggests that the geometry of the perfusion and collection tips for the new device improves the directional transport through the tissue.

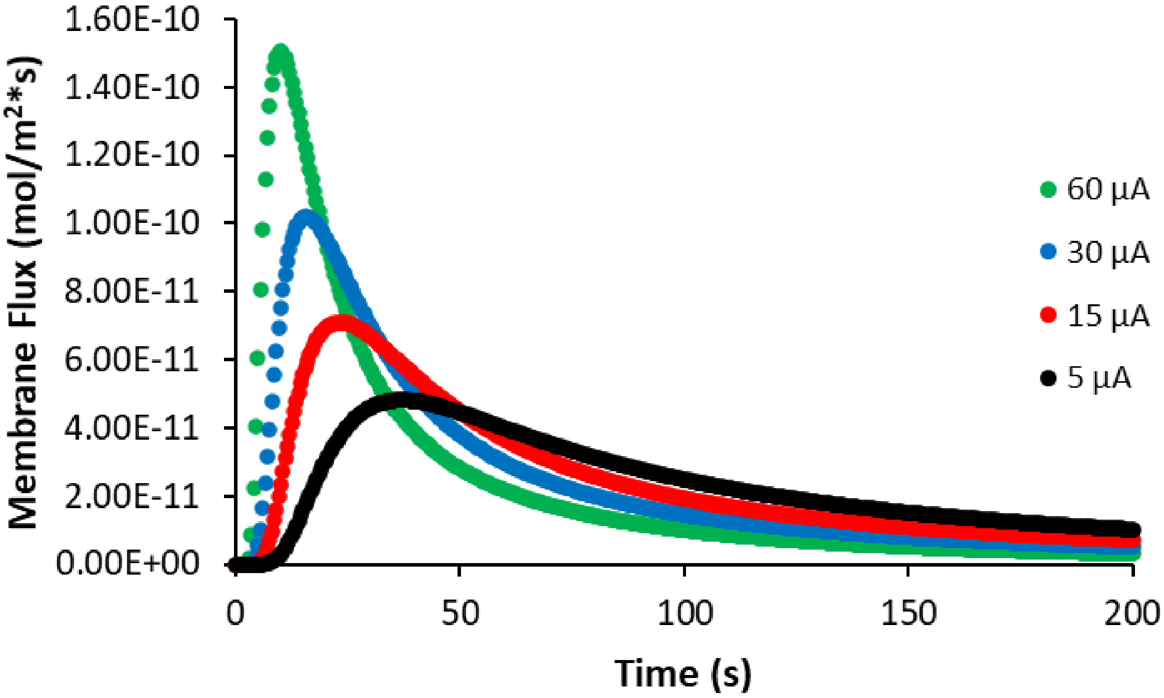

Figure 46. Using the simulation for the EOP-MD model, the flux (mol/m^{2}s) of yaGfl peptide through the outer wall of the microdialysis membrane was monitored over 500 s at four different currents: 5 μA (black), 15 μA (red), 30 μA (blue) and 60 μA (green). In each case, only the tip of the perfusion capillary was programmed to contain 1.0 mM yaGfl, while the remainder of the perfusion channel contained only aCSF.

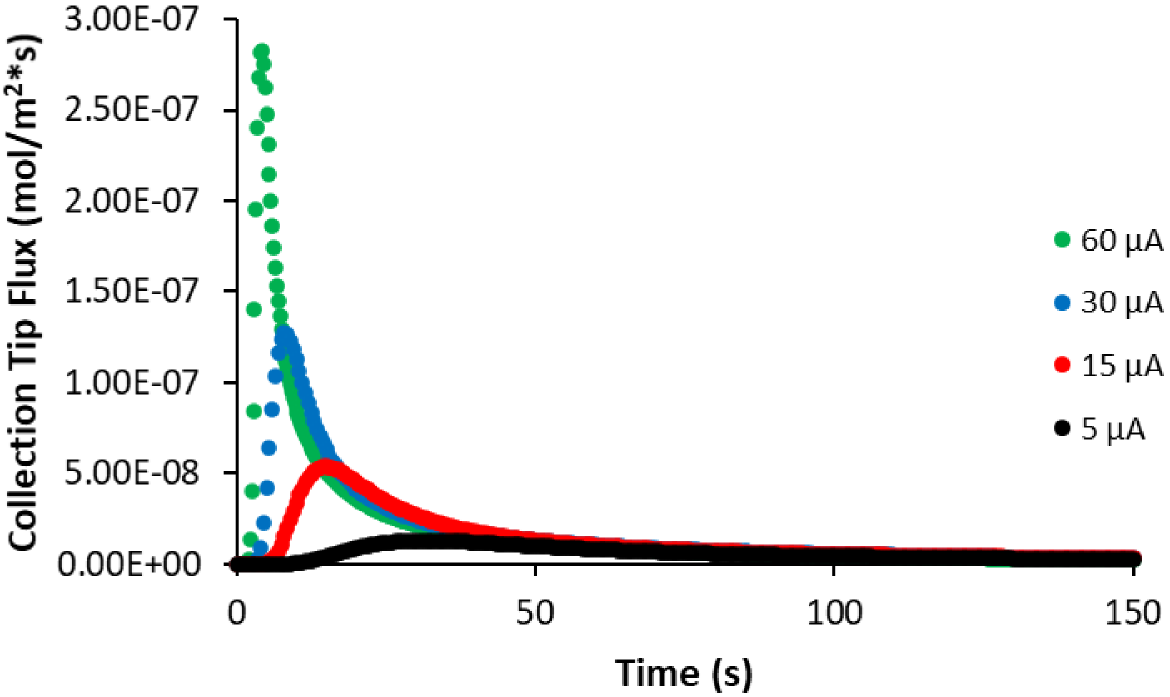

Figure 47. Using the simulation for the EOP-EMD model, the flux (mol/m^{2}s) of yaGfl peptide through the collection channel orifice was monitored over 500 s at four different currents: 5 µA (black), 15 µA (red), 30 µA (blue) and 60 µA (green). In each case, only the tip of the perfusion capillary was programmed to contain 1.0 mM yaGfl, while the remainder of the perfusion channel contained only aCSF.

Table 9. Calculated tissue residence times for both the EOP-MD and EOP-EMD devices at varied currents defiined as the first moment of the flux vs. time curve

		I_{app} (µA)			
		5	15	30	60
First Moment (s)	**EOP-MD**	141.0	112.3	89.6	65.0
	EOP-EMD	126.8	88.6	66.8	48.0

5.3.3 *In vitro* Method Development

A calibration curve was constructed to evaluate the HPLC method developed to quantify yaGfl concentrations within a dialysate matrix using UV detection. This was done to assess linearity over the expected concentration range *in vivo* based on simulated results, and to determine the limit of detection for the system. A series of yaGfl concentrations were made in modified Ringer's ranging in concentration from 1.56 – 100 μM, with each concentration analyzed in triplicate. The results are shown in Figure 48. Linearity was achieved over the concentration range analyzed, yielding a slope ± SEM = 0.0574 ±0.0004 [mV/(min*μm)] and an intercept ± SEM = 0.011 ± 0.018 mV/min. Based on the standard deviation of replicates (n = 3) for the lowest concentration measured (1.56 μM) and the slope of the calibration curve, the limit of detection for the system was found to be 0.73 ± 0.09 μM. This value fell an order of magnitude below the expected dialysate concentrations when infusing 1.0 mM yaGfl of roughly 10 μM.

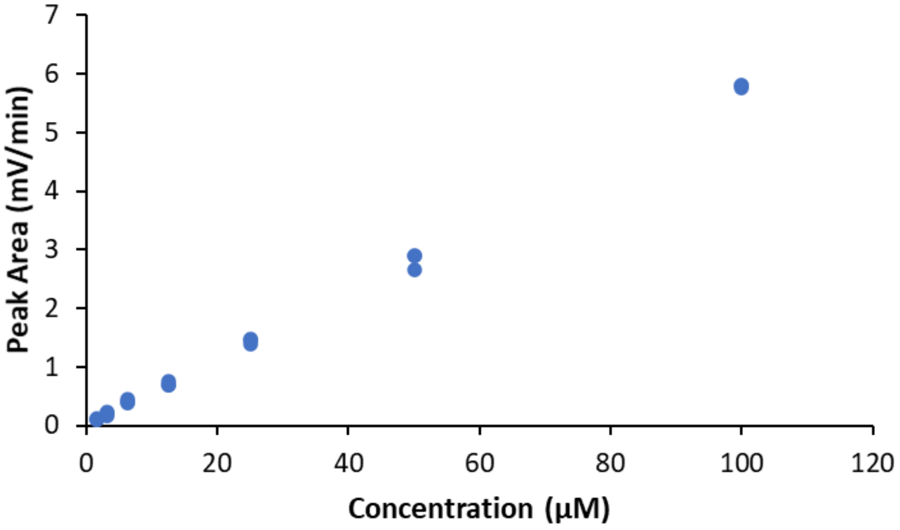

Figure 48. Calibration curve obtained for the UV detector setup using various concentration of yaGfl ranging from 1.56 – 100 μM. The detector wavelength was set to 214 nm. Each concentration was run in triplicate, with all data points displayed here.

5.3.4 Evaluation of Device Performance *in vivo*

While the simulation data for the EOP-EMD design indicated experimental benefits relative to the EOP-MD design including faster time to steady state, experimental validation of the device is essential. The device was tested *in vivo* through implantation into the prefrontal cortex of a rat and substrate dialysate concentrations were continuously monitored at various applied currents. The goals of this experiment were 1) to demonstrate control of tissue perfusion using electroosmotic flow by varying applied current, 2) to provide experimental data to compare to the theoretical models for method validation, and 3) to investigate control of infusion concentration with the dual channel mixing design. The peptide yaGfl was chosen as the perfusion substrate because it is not hydrolyzed by any known enzyme within the brain. Therefore, detected concentrations would be solely influenced by mass transport and not influenced by degradation mechanisms. A detailed description of applied current control is provided in Section 5.2.8. The yaGfl in the dialysate was detected every 7 minutes through capillary HPLC separation and UV detection at 214 nm. The calibration curve presented in Figure 5.3.3 was used to calculate concentrations. Calculated concentrations as a function of time are reported in Figure 49.

The results demonstrate that measured dialysate concentrations react more rapidly to changes in applied current for the EOP-EMD design relative to the EOP-MD design, in agreement with simulated results. The dialysate reaches a relatively stable concentration within 7-14 minutes, or 1-2 injections, of the change in current. This is significantly faster than the slow concentration rise observed in previous *in vivo* experiments using the EOP-MD design which yielded increasing concentrations even after 60 minutes after current was induced. This improvement allows for a greater number of perfusion compositions to be infused into the tissue for a given experiment, increasing the density of information that can be obtained using a single animal.

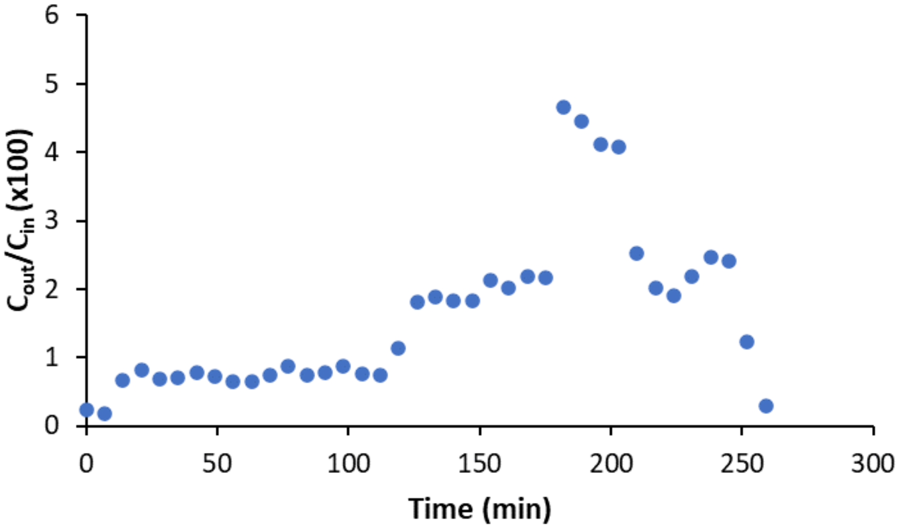

Figure 49. The ratio of yaGfl concentration measured in the dialysate (C_{out}) to the concentration of yaGfl in the perfusion solution (C_{in}) as a function of time for the *in vivo* experiment. Time = 0 min indicates when the 15 µA current was first applied to the perfusion channel containing only modified Ringer's solution. At 56 minutes, the 15 µA applied current was switched to the perfusion channel filled with 1.0 mM yasfl. This channel was infused for the remainder of the experiment. The current was increased to 30 µA at 112 minutes, increased to 60 µA at 175 minutes, and decreased to 30 µA at 203 minutes. The experiment was terminated after the microdialysis probe failed at some time after 245 minutes.

These results also demonstrated an excellent linear relationship between detected concentration and applied current, along with a good agreement with the theoretical model executed in COMSOL reported in Figure 50. The measured yaGfl dialysate concentrations were first converted to percent of perfused peptide recovered in the dialysate, [(C_{out}/C_{in})x100] and average value was determined for each applied current. The *in vivo* results yielded a slope ± 95% CI = 0.0791 ± 0.008 μA^{-1} and intercept ± 95% CI = -0.42 ± 0.33. Notably though, the intercept of this data is statistically distinguishable from 0, possibly caused by small amounts of native peptide contributing to the UV absorbance. The simulated results yielded a slope ± 95% CI = 0.06 ± 0.09 μA^{-1} and intercept ± 95% CI = 0.27 ± 3.39. While the slope is larger for the *in vivo* results compared to the simulation, this could be influenced by the small sample size at 60 μA. Bubbles were observed in the tubing connecting the MD outlet to the switching valve, so the current was dropped back down to 30 μA after only 4 injections to avoid damaging the device at higher currents. Overall, the comparison of the *in vivo* results validates the advantages of the EOP-EMD design observed in previous simulations.

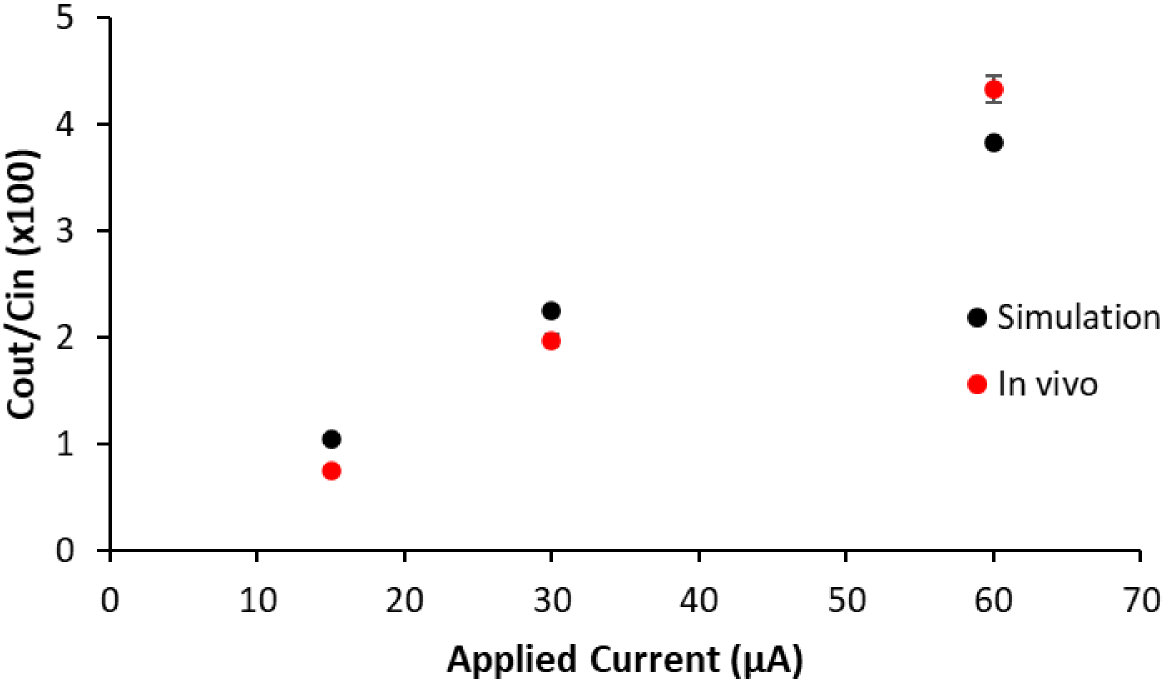

Figure 50. Comparison of simulated (black) and *in vivo* (red) percent of perfusion concentration measured as a function of applied current using the EOP-EMD device In both cases, the concentration of yaGfl in the perfusion solution was 1.0 mM. For the simulated data, the concentration of the dialysate corresponds to the

steady state concentration. For the *in vivo* data, the concentration of the dialysate corresponds to the average concentration taken within 56-112 mins, 126-175 mins, and 189-203 mins for 15, 30, and 60 µA respectively.. Error bars display the standard error of the mean for each data point.

The experimental results are encouraging yield good agreement with the theoretical advantages of the device observed in the COMSOL models. Further testing will be required to investigate the internal mixing channel design and to increase the number of *in vivo* experiments for a detailed statistical analysis of the device performance metrics. The initial test of controlling the perfusion concentration through internal mixing of the dual perfusion channel design did not work during the *in vivo* experiment. We believe this is due to perfusion channel loading errors resulting from filling each channel individually, and that this can be resolved by simultaneously filling both channels using a syringe pump. Internal mixing controlled by electroosmotic flow was tested for a two channel Y-junction model, which was ultimately implemented into the EOP-EMD design, and for a three channel T-junction design we plan to implement in the future. Simulated results are shown in Figure 53 and 54 within the Supplemental Information. Using a three-channel design, each channel can be filled with modified Ringer's, concentrated substrate, and inhibitor respectively. This provides a tunable range of substrate and inhibitor concentrations controlled through electroosmotic flow. Another future aim involves increasing the length of the perfusion and collection tips. The tips are currently long enough for implantation into the prefrontal cortex, but longer tips extending into deeper regions of the brain tissue have the ability to increase the number of biochemistry and pharmacology applications available for study.

5.4 Conclusions

In this work, we have demonstrated a novel method for sampling the neurochemical environment of the brain where the microdialysis probe is removed from the tissue and tissue perfusion/collection is achieved using electroosmotic flow. We have advanced our electroosmotic perfusion-microdialysis sampling design to be less invasive and provide faster time to steady states for detected solute concentrations. This increases the utility of this method by increasing the data density that can be obtained for a given experiment. We have also developed finite element models in COMSOL Multiphysics for both the previously published device and the new integrated probe design. We have used these models to provide information regarding how the geometric configuration of the device affects detected concentrations in the collected dialysate, and to determine solute residence time within the tissue. These models can be used to further optimize the device design, exploring more efficient ways to incorporate perfusion channel mixing through electroosmotic flow, and to determine quantitative kinetic information to study enzymatic activity. Variation to probe length can also be easily modified and constructed using direct laser writing to provide the researcher with the dimensions required to target specific areas of the brain for study.

5.5 Supplemental Information

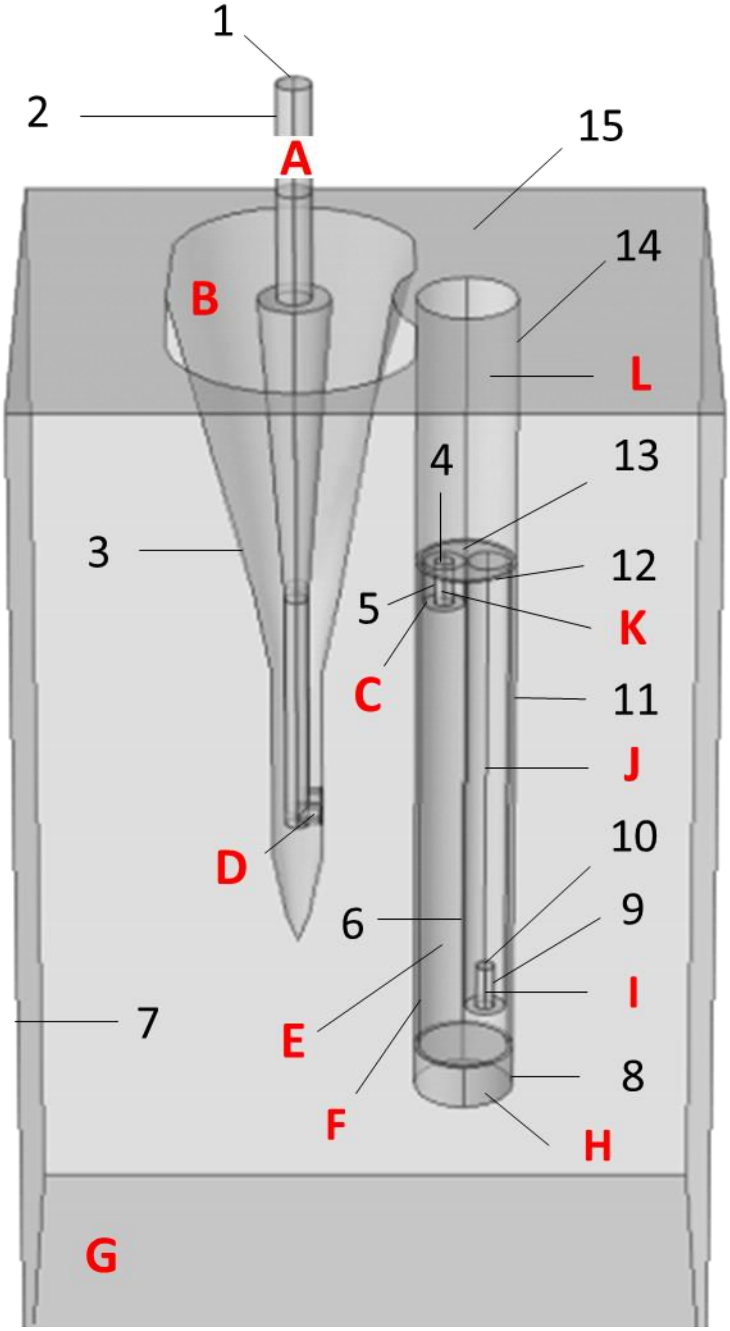

Figure 51. 3D geometry for the EOP-MD model. Domains are indicated by letters and boundaries are indicated by numbers. Domains: A - Perfusion channel, B - Probe perfusion tip, C – MD inlet capillary, D – Pulsed volume for residence time study, E – MD probe lumen, F – MD probe membrane, G – Brain tissue, H

– MD tip epoxy, I – Inner channel of MD outlet capillary, J – MD outlet capillary, K – Inner channel of MD inlet capillary, L – Subtracted upper portion of MD probe. Boundaries: 1 – Perfusion inlet, 2 – Perfusion channel walls, 3 - Probe perfusion tip walls, 4 - MD probe inlet, 5 - Inner walls of MD inlet capillary, 6 - Outer walls of MD outlet capillary, 7 - Side and bottom surfaces of tissue, 8 - MD tip epoxy walls, 9 - Inner walls of MD outlet capillary, 10 - MD probe outlet, 11 - MD membrane walls, 12 - Top surface of MD membrane, 13 – Top surface of MD lumen, 14 – Walls of subtracted upper portion of MD probe, 15 – Top surface of the tissue.

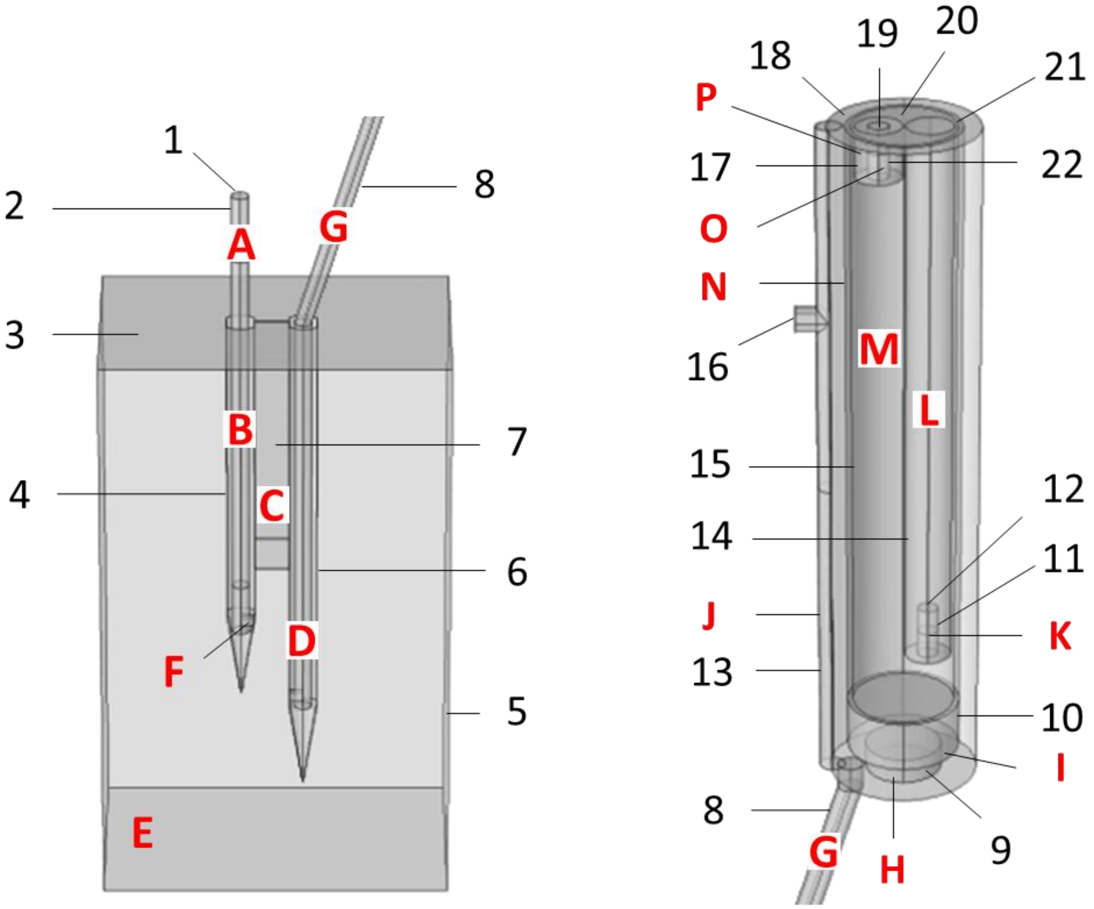

Figure 52. 3D geometry for the EOP-EMD model. Domains are indicated by letters and boundaries are indicated by numbers. Domains: A - Perfusion channel, B - Probe perfusion tip, C - Probe tip support, D – Probe collection tip, E – Brain tissue, F – Pulsed volume for residence time study, G – Collection channel, H – MD probe platform, I – MD tip epoxy, J – MD sampling chamber, K – Inner channel of MD outlet capillary,

L – MD outlet capillary, M – MD probe lumen, N – MD probe membrane, O – Inner channel of MD inlet capillary, P – MD inlet capillary. Boundaries: 1 – Perfusion inlet, 2 – Perfusion channel walls, 3 – Top surface of tissue, 4 – Probe perfusion tip walls, 5 – Side and bottom surfaces of tissue, 6 – Collection channel walls, 7 – Probe tip support walls, 8 – Collection channel walls, 9 – MD probe platform walls, 10 – MD tip epoxy walls, 11 – Inner walls of MD outlet capillary, 12 – MD probe outlet, 13 – Outer walls of MD sampling chamber, 14 – Outer walls of MD outlet capillary, 15 – MD membrane walls, 16 – MD sampling chamber outlet, 17 – Outer walls of MD inlet capillary, 18 – Top surface of MD sampling chamber, 19 – MD probe inlet, 20 – Top surface of MD probe lumen, 21 – Top surface of MD membrane, 22 – Inner walls of MD inlet capillary.

Table 10. Boundary conditions for Electric Currents module for the EOP-MD model. *J* is current density, *σ* is the conductivity, *V* is the voltage drop, *Je* is the external current density source, *n* is the normal vector, a_{MD} is the area of the MD probe inlet, and i_0 is the applied current.

Domain/Boundary	Boundary Condition	Equation
A-L	Current conservation using global coordinate system	$\nabla \cdot \vec{J} = -\nabla \cdot \left(\sigma \nabla V - \vec{J}_e\right) = 0$
2-3, 5-9, 12-15	Electric Insulation	$\vec{n} \cdot \vec{J} = 0$
4	Boundary Current Source	$J = i_0 / a_{MD}$, where $i_0 = -5, -15, -30, -60$ μA
1	Ground	$V = 0$

Table 11. Boundary conditions for the Free and Porous Media Flow for EOP-MD model. *u* is the superficial velocity, μ_{eo} is the electroomotic mobility, *E* is the electric field, *P* is the pressure, L_{Perf} is the length of perfusion inlet capillary not represented in the model to save computation time, L_{MD} is the length of MD outlet capillary not represented in the model to save computation time, η is the dynamic viscosity, Δu is the difference between the wall velocity and the average velocity, a_{Perf} is the area of the perfusion capillary, a_{MD} is the area of the MD outlet capillary, and f_0 is the normal stress.

Domain/Boundary	Boundary Condition	Equation
3, 6, 8, 12-15	No slip walls	$\vec{u} = 0$
2, 5, 9	Electroomotic velocity walls	$\vec{u} = \sqrt{\vec{u}^2{}_x + \vec{u}^2{}_y + \vec{u}^2{}_z}$ where, $\vec{u}_x = \mu_{eo} \cdot \vec{E}_x$ $\vec{u}_y = \mu_{eo} \cdot \vec{E}_y$ $\vec{u}_z = \mu_{eo} \cdot \vec{E}_z$
1	"Hagen-Poiseuille Inlet"	$\Delta P = \frac{8L_{Perf}\eta\Delta u}{a^2{}_{Perf}}$
10	"Hagen-Poiseuille Outlet"	$\Delta P = \frac{8L_{MD}\eta\Delta u}{a^2{}_{MD}}$
4	Fully Developed Flow Rate, Inlet	$F = F_0$, where $F_0 = 8.33e^{-12}\mathrm{m}^3/\mathrm{s}$
7	Open boundary	$f_0 = 0$

Table 12. Boundary conditions for Transport of Diluted Species in Porous Media module for EOP-MD model. *N* is the flux, *c* is the concentration, c_0 is the initial concentration, and D is the diffusion coefficient. *Boundary condition residence time study.

Domain/Boundary	**Boundary Condition**	**Equation**
2-3, 5-6, 8-9, 12-14	No flux	$-\vec{n}\cdot\vec{N}=0$
1	Inflow Flux	$\vec{N}=\vec{n}\cdot(c\vec{u}-D\nabla c)$
10	Outflow Flux	$\vec{N}=\vec{n}\cdot(c\vec{u}-D\nabla c)$
1	Concentration	$c=c_0;$ $c_0=1.0\text{ mM}$
7	Open Boundary	$\begin{cases}-\vec{n}\cdot D\nabla c=0 & \text{if}\,\vec{n}\cdot\vec{u}\geq 0\\ c=0 & \text{if}\,\vec{n}\cdot\vec{u}<0\end{cases}$
B-C, E-L	Initial Values	$c_0=0$
A, D	Initial Values	$c_0=1.0\text{ mM}$
A*	Initial Values	$c_0=0$
D*	Initial Values	$c_0=1.0\text{ mM}$

Table 13. Material properties for EOP-MD model.

Domain(s)	Property	Value
A, D-G, I, K	Density (ρ)	1×10^{3} kg/m^{3}
	Permittivity of water (ε_w)	7.1×10^{-10} F/m
	Permittivity of vacuum (ε_0)	8.85×10^{-12} F/m
	Dynamic viscosity (η)	8.9×10^{-4} Pa s
A, E-F, I, K	Conductivity (σ) of buffer	1.79 S/m
	Capillary ζ-potential	-46.5 mV
F	Permeability (κ)	1.55×10^{-19} m^{2}
	Porosity (ε)	0.2
	Tortuosity (λ)	2.42
	Conductivity of Membrane	0.061 S/m
G	Permeability (κ)	10^{-15} m^{2}
	Porosity (ε)	0.2
	Tortuosity (λ)	1.61
	Tissue ζ-potential	-22.8 mV
	Conductivity (σ) of Tissue	0.14 S/m
	Electroosmotic mobility* (μ_{eo})	3.7×10^{-8} m^{2}/(V*s)

Table 14. Boundary conditions for Electric Currents module in COMSOL Multiphysics (v5.6) for the EOP-EMD model. *J* is current density, *σ* is the conductivity, *V* is the voltage drop, *Je* is the external current density source, *n* is the normal vector, a_{MD} is the area of the MD probe inlet, and i_0 is the applied current.

Domain/Boundary	Boundary Condition	Equation
A-P	Current conservation using global coordinate system	$\nabla \cdot \vec{J} = -\nabla \cdot \left(\sigma \nabla V - \vec{J}_e\right) = 0$
2-14, 16-18, 20-22	Electric Insulation	$\vec{n} \cdot \vec{J} = 0$
19	Boundary Current Source	$J = i_0 / a_{MD}$, where $i_0 = -5, -15, -30, -60\ \mu\text{A}$
1	Ground	$V = 0$

Table 15. Boundary conditions for the Free and Porous Media Flow for EOP-MD model. u is the superficial velocity, μ_{eo} is the electroomotic mobility, E is the electric field, P is the pressure, L_{Perf} is the length of perfusion inlet capillary not represented in the model to save computation time, L_{MD} is the length of MD outlet capillary not represented in the model to save computation time, η is the dynamic viscosity, Δu is the difference between the wall velocity and the average velocity, a_{Perf} is the area of the perfusion capillary, a_{MD} is the area of the MD outlet capillary, and f_0 is the normal stress.

Domain/Boundary	Boundary Condition	Equation
3, 6, 8, 12-15	No slip walls	$\vec{u} = 0$
2, 5, 9	Electroomotic velocity walls	$\vec{u} = \sqrt{\vec{u}^2{}_x + \vec{u}^2{}_y + \vec{u}^2{}_z}$ where, $\vec{u}_x = \mu_{eo} \cdot \vec{E}_x$ $\vec{u}_y = \mu_{eo} \cdot \vec{E}_y$ $\vec{u}_z = \mu_{eo} \cdot \vec{E}_z$
1	"Hagen-Poiseuille Inlet"	$\Delta P = \frac{8L_{EOP}\eta\Delta u}{a^2{}_{EOP}}$
10	"Hagen-Poiseuille Outlet"	$\Delta P = \frac{8L_{MD}\eta\Delta u}{a^2{}_{MD}}$
4	Fully Developed Flow Rate, Inlet	$F = F_0$, where $F_0 = 8.33e^{-12}\mathrm{m}^3/\mathrm{s}$
7	Open boundary	$f_0 = 0$

Table 16. Boundary conditions for Transport of Diluted Species in Porous Media module for EOP-EMD model. ***N*** **is the flux,** ***c*** **is the concentration, c_0 is the initial concentration, and D is the diffusion coefficient. *Boundary condition residence time study.**

Domain/Boundary	Boundary Condition	Equation
2-3, 5-6, 8-9, 12-14	No flux	$-\vec{n} \cdot \vec{N} = 0$
1	Inflow Flux	$\vec{N} = \vec{n} \cdot (c\vec{u} - D\nabla c)$
10	Outflow Flux	$\vec{N} = \vec{n} \cdot (c\vec{u} - D\nabla c)$
1	Concentration	$c = c_0;$ $c_0 = 1.0\ \mathrm{mM}$
7	Open Boundary	$\begin{cases} -\vec{n} \cdot D\nabla c = 0 & \text{if}\, \vec{n} \cdot \vec{u} \geq 0 \\ c = 0 & \text{if}\, \vec{n} \cdot \vec{u} < 0 \end{cases}$
B-C, E-L	Initial Values	$c_0 = 0$
A, D	Initial Values	$c_0 = 1.0\ \mathrm{mM}$
A*	Initial Values	$c_0 = 0$
D*	Initial Values	$c_0 = 1.0\ \mathrm{mM}$

Table 17. Material properties for EOP-EMD model.

Domain(s)	Property	Value
A, E, F, G, K, J, M, N	Density (ρ)	1 x 10^3 kg/m^3
	Permittivity of water (ε_w)	7.1 x 10^{-10} F/m
	Permittivity of vacuum (ε_0)	8.85 x 10^{-12} F/m
	Dynamic viscosity (η)	8.9 x 10^{-4} Pa s
A, G, J, K, M, O	Conductivity (σ) of buffer	1.79 S/m
	Capillary ζ-potential	-46.5 mV
N	Permeability (κ)	1.55 x 10^{-19} m^2
	Porosity (ε)	0.2
	Tortuosity (λ)	2.42
	Conductivity of Membrane	0.061 S/m
E	Permeability (κ)	10^{-15} m^2
	Porosity (ε)	0.2
	Tortuosity (λ)	1.61
	Tissue ζ-potential	-22.8 mV
	Conductivity (σ) of Tissue	0.14 S/m
	Electroosmotic mobility* (μ_{eo})	3.7 x 10^{-8} m^2/(V*s)

Table 18. Species properties for the EOP-EMD and EOP-MD models.

Property	Value
Diffusion Coefficient of yaGfl in free solution	3.61 x 10^{-10} m^2/s

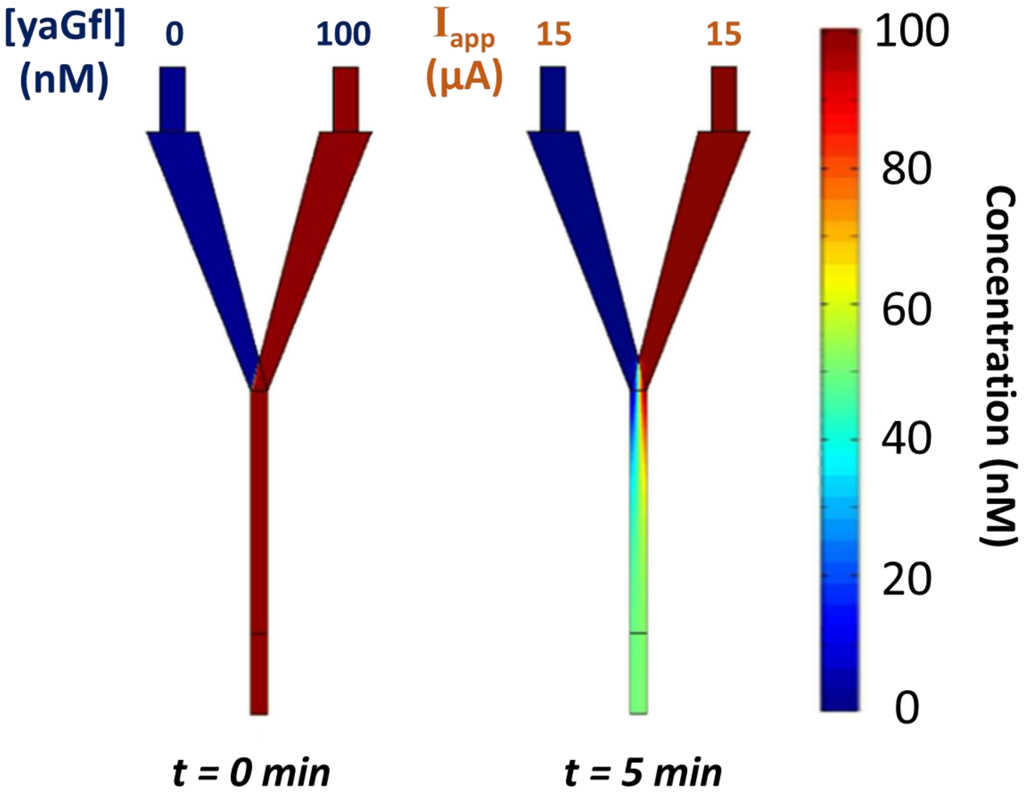

Figure 53. Two-channel Y-junction perfusion channel design tested in COMSOL Multiphysics. The left and right perfusion channel were programmed to contain 0 and 100 nM yaGfl respectively. These intial concentrations are shown for t = 0 minutes. A 15 μA current was applied to the boundary of each of the perfusion channels, and the concentration profile is shown after 5 minutes of flow.

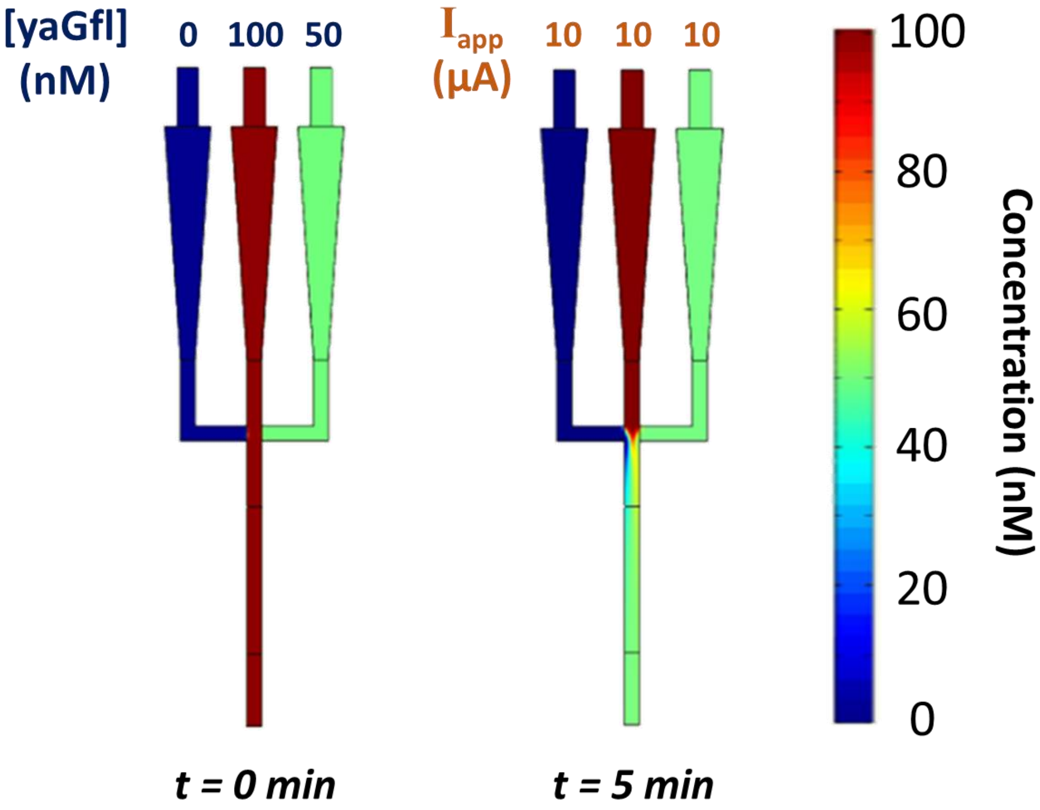

Figure 54. Three-channel T-junction perfusion channel design tested in COMSOL Multiphysics. The perfusion channels were programmed to contain 0, 100, and 50 nM yaGfl from left to right. These intial concentrations are shown for t = 0 minutes. A 10 μA current was applied to the boundary of each of the perfusion channels, and the concentration profile is shown after 5 minutes of flow.

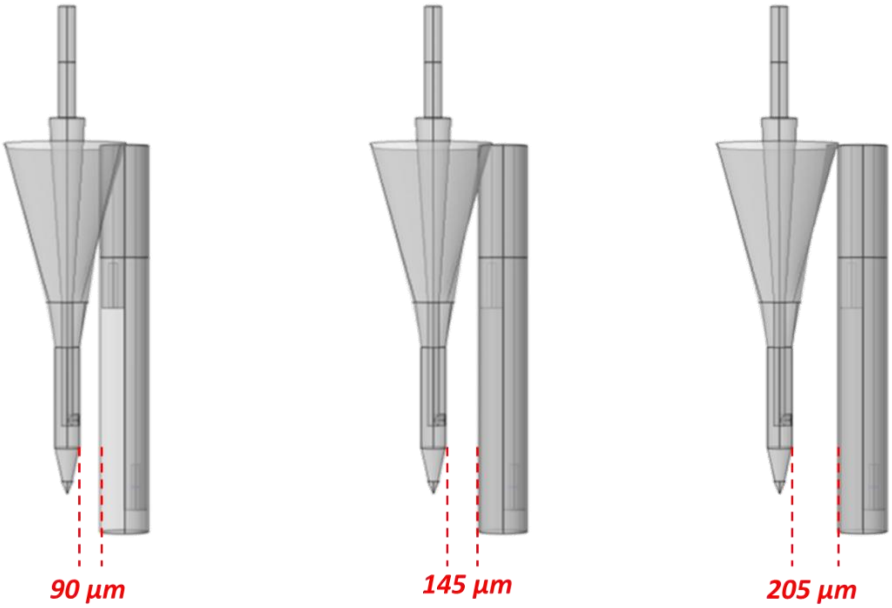

Figure 55. Schematic representation of varying microdialysis probe distance from the perfusion tip.

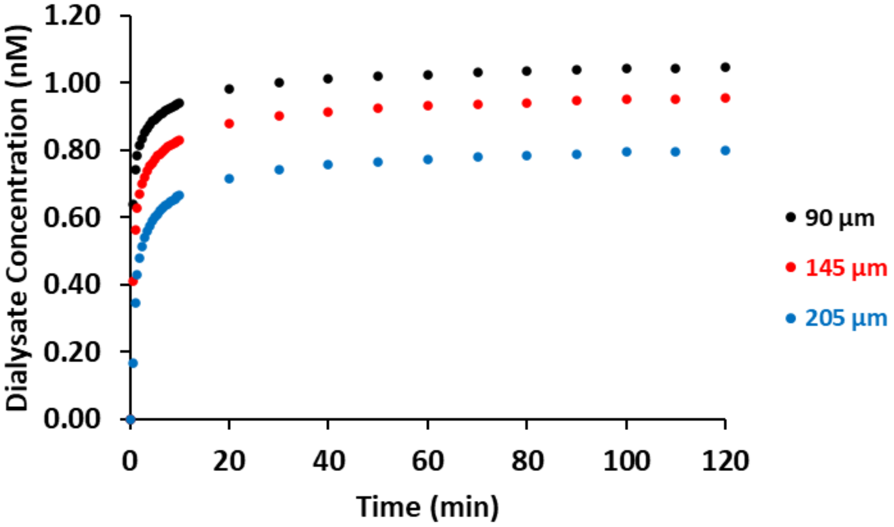

Figure 56. Concentration profiles for the previously published design, measured by the volume average concentration of yaGfl in the microdialysis outlet as a function of time. Here, the distance between the microdialysis probe and the perfusion tip was varied by 90 µm (black), 145 µm (red), and 205 µm (blue). In all cases, the perfusion solution contained 100 nM yaGfl peptide and the current was maintained at 15 µA.

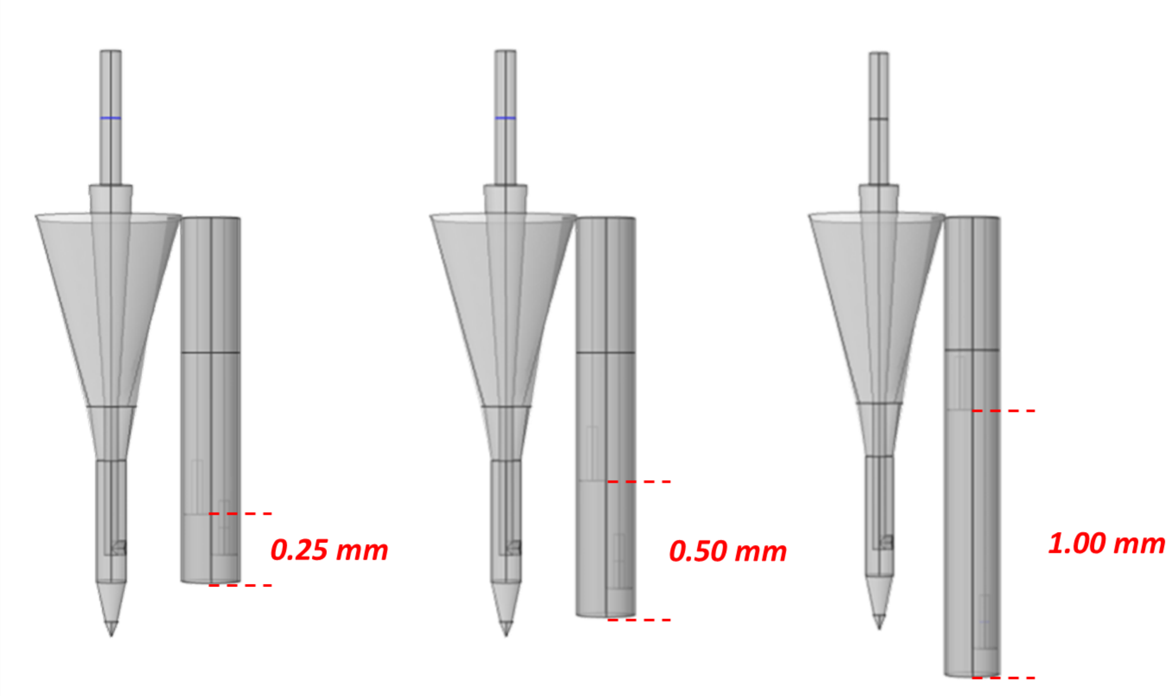

Figure 57. Schematic representation of varying the effective microdialysis probe membrane length.

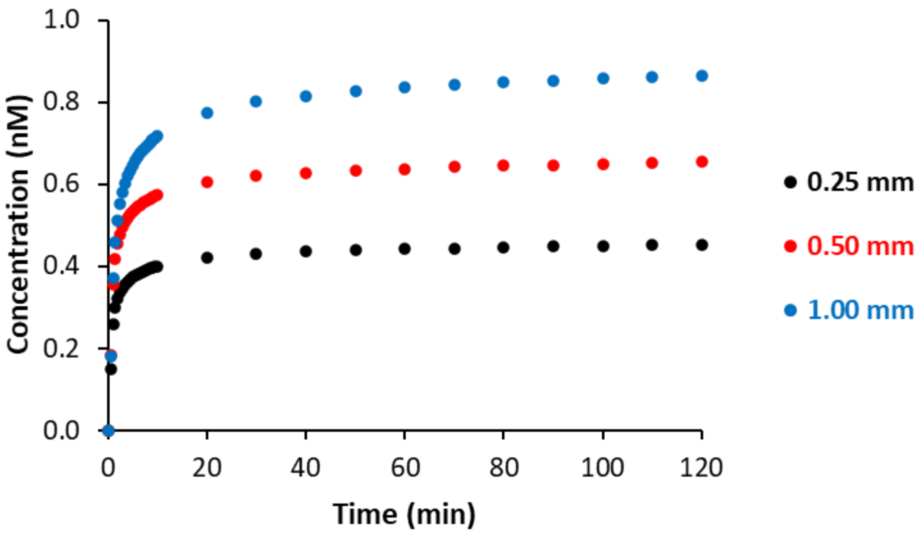

Figure 58. Concentration profiles for the previously published design, measured by the volume average concentration of yaGfl in the microdialysis outlet as a function of time. Here, the effective length of the

microdialysis was programmed to 0.25 mm (black), 0.5 mm (red), and 1.0 mm (blue). In all cases, the perfusion solution contained 100 nM yaGfl peptide and the current was maintained at 15 µA.

Bibliography

1. Buszewski, B.; Noga, S., Hydrophilic interaction liquid chromatography (HILIC)--a powerful separation technique. *Anal Bioanal Chem* **2012,** *402* (1), 231-247.

2. Hemström, P.; Irgum, K., Hydrophilic interaction chromatography. *J Sep Sci* **2006,** *29* (12), 1784-821.

3. Linden, J. C.; Lawhead, C. L., Liquid chromatography of saccharides. *Journal of chromatography A* **1975,** *105* (1), 125-133.

4. Alpert, A. J.; Shukla, M.; Shukla, A. K.; Zieske, L. R.; Yuen, S. W.; Ferguson, M. A.; Mehlert, A.; Pauly, M.; Orlando, R., Hydrophilic-interaction chromatography of complex carbohydrates. *J Chromatogr A* **1994,** *676* (1), 191-22.

5. Churms, S. C., Recent progress in carbohydrate separation by high-performance liquid chromatography based on size exclusion. *Journal of Chromatography A* **1996,** *720* (1-2), 151-166.

6. Boersema, P. J.; Mohammed, S.; Heck, A. J., Hydrophilic interaction liquid chromatography (HILIC) in proteomics. *Anal Bioanal Chem* **2008,** *391* (1), 151-159.

7. Li, R.; Huang, J., Chromatographic behavior of epirubicin and its analogues on high-purity silica in hydrophilic interaction chromatography. *J Chromatogr A* **2004,** *1041* (1-2), 163-9.

8. Snyder, L. R.; Dolan, J. W.; Carr, P. W., The hydrophobic-subtraction model of reversed-phase column selectivity. *Journal of Chromatography A* **2004,** *1060* (1), 77-116.

9. Kirkland, J. J., Development of some stationary phases for reversed-phase high-performance liquid chromatography. *J Chromatogr A* **2004,** *1060* (1-2), 9-21.

10. Poppe, H., Some reflections on speed and efficiency of modern chromatographic methods. *Journal of Chromatography A* **1997,** *778* (1), 3-21.

11. Martin, A. J.; Synge, R. L., A new form of chromatogram employing two liquid phases: A theory of chromatography. 2. Application to the micro-determination of the higher monoamino-acids in proteins. *Biochem J* **1941,** *35* (12), 1358-1368.

12. Snyder, L. R.; Kirkland, J. J.; Dolan, J. W., *Introduction to Modern Liquid Chromatography*. 3rd Edition ed.; John Wiley & Sons, Inc.: Hoboken, New Jersey, 2010.

13. Carr, P. W.; Wang, X.; Stoll, D. R., Effect of Pressure, Particle Size, and Time on Optimizing Performance in Liquid Chromatography. *Analytical Chemistry* **2009,** *81* (13), 5342-5353.

14. Deemter, J. v.; Zuiderweg, F.; Klinkenberg, A., Longitudinal diffusion and resistance to mass transfer as causes of nonideality in chromatography. *Chemical Engineering Science* **1956,** *5*, 271-289.

15. Sanchez, A. C.; Friedlander, G.; Fekete, S.; Anspach, J.; Guillarme, D.; Chitty, M.; Farkas, T., Pushing the performance limits of reversed-phase ultra high performance liquid chromatography with 1.3μm core–shell particles. *Journal of Chromatography A* **2013,** *1311*, 90-97.

16. Fekete, S.; Guillarme, D., Possibilities of new generation columns packed with 1.3μm core–shell particles in gradient elution mode. *Journal of Chromatography A* **2013,** *1320*, 86-95.

17. Xu, Q. A.; Fekete, S.; Schappler, J.; Rudaz, S. M. T.; Veuthey, J.-L.; Guillarme, D., *Ultra-high performance liquid chromatography and its applications*. Wiley Online Library: 2013.

18. Neue, U. D.; Kele, M.; Bunner, B.; Kromidas, A.; Dourdeville, T.; Mazzeo, J. R.; Grumbach, E. S.; Serpa, S.; Wheat, T. E.; Hong, P., Ultra-performance liquid chromatography technology and applications. *Adv. Chromatogr* **2009,** *48*, 99-104.

19. Op de Beeck, J.; De Malsche, W.; De Moor, P.; Desmet, G., Hydrodynamic chromatography separations in micro- and nanopillar arrays produced using deep-UV lithography. *J Sep Sci* **2012,** *35* (15), 1877-83.

20. Vangelooven, J.; Desmet, G., Theoretical optimisation of the side-wall of micropillar array columns using computational fluid dynamics. *J Chromatogr A* **2010,** *1217* (52), 8121-6.

21. Desmet, G.; Eeltink, S., Fundamentals for LC Miniaturization. *Analytical Chemistry* **2013,** *85* (2), 543-556.

22. Novotny, M. V.; Ishii, D., *Microcolumn separations: columns, instrumentation, and ancillary techniques*. Elsevier; Distruibutors for the U.S. and Canada, Elsevier Science Pub. Co.: Amsterdam; New York; New York, 1985.

23. Guiochon, G. A.; Colin, H. M., *Microcolumn high-performance liquid chromatography*. Elsevier: Amsterdam; New York, 1984.

24. Gluckman, J. C.; Novotny, M. V., *Microcolumn separations columns, instrumentation, and ancillary techniques*. Elsevier: Amsterdam; New York, 1985.

25. Colin, H.; Martin, M.; Guiochon, G., Extra-column effects in high-performance liquid chromatography: I. Theoretical study of the injection problem. *Journal of Chromatography A* **1979,** *185* (Supplement C), 79-95.

26. Bakalyar, S. R.; Phipps, C.; Spruce, B.; Olsen, K., Choosing sample volume to achieve maximum detection sensitivity and resolution with high-performance liquid

chromatography columns of 1.0, 2.1 and 4.6 mm I.D. *Journal of Chromatography A* **1997,** *762* (1), 167-185.

27. Foster, M. D.; Arnold, M. A.; Nichols, J. A.; Bakalyar, S. R., Performance of experimental sample injectors for high-performance liquid chromatography microcolumns. *Journal of Chromatography A* **2000,** *869* (1), 231-241.

28. Sternberg, J. C., Extracolumn contributions to chromatographic band broadening. *Advances in Chromatography* **1966,** *2*, 205-270.

29. Kirkland, J. J.; Yau, W. W.; Stoklosa, H. J.; Dilks, C. H., Jr., Sampling and extra-column effects in high-performance liquid chromatography; influence of peak skew on plate count calculations. *J Chromatogr Sci* **1977,** *15* (8), 303-16.

30. Héron, S.; Tchapla, A.; Chervet, J. P., Influence of injection parameters on column performance in nanoscale high-performance liquid chromatography. *Chromatographia* **2000,** *51* (7), 495-499.

31. Bakalyar, S. R.; Phipps, C.; Spruce, B.; Olsen, K., Choosing sample volume to achieve maximum detection sensitivity and resolution with high-performance liquid chromatography columns of 1.0, 2.1 and 4.6 mm I.D. *J Chromatogr A* **1997,** *762* (1-2), 167-85.

32. Gilar, M.; McDonald, T. S.; Johnson, J. S.; Murphy, J. P.; Jorgenson, J. W., Wide injection zone compression in gradient reversed-phase liquid chromatography. *J Chromatogr A* **2015,** *1390*, 86-94.

33. Holm, A.; Molander, P.; Lundanes, E.; Greibrokk, T., Novel column oven concept for cold spot large volume sample enrichment in high throughput temperature gradient capillary liquid chromatography. *Journal of Separation Science* **2003,** *26* (12-13), 1147-1153.

34. Causon, T. J.; Cortes, H. J.; Shellie, R. A.; Hilder, E. F., Temperature Pulsing for Controlling Chromatographic Resolution in Capillary Liquid Chromatography. *Analytical Chemistry* **2012,** *84* (7), 3362-3368.

35. Molander, P.; Haugland, K.; Hegna, D. R.; Ommundsen, E.; Lundanes, E.; Greibrokk, T., Determination of low levels of an antioxidant in polyolefins by large-volume injection temperature-programmed packed capillary liquid chromatography. *Journal of Chromatography A* **1999,** *864* (1), 103-109.

36. Molander, P.; Holm, A.; Lundanes, E.; Greibrokk, T.; Ommundsen, E., Separation of Ceramides by Sub-Ambient Temperature-Assisted Large Volume Injection in Temperature-Programmed Packed Capillary Liquid Chromatography. *Journal of High Resolution Chromatography* **2000,** *23* (11), 653-655.

37. Molander, P.; Holm, A.; Lundanes, E.; Hegna, D. R.; Ommundsen, E.; Greibrokk, T., Temperature-promoted large-volume solute enrichment in column-switching miniaturized liquid chromatography: determination of an antioxidant. *Analyst* **2002,** *127* (7), 892-7.

38. van de Ven, H. C.; Gargano, A. F.; van der Wal, S.; Schoenmakers, P. J., Switching solvent and enhancing analyte concentrations in small effluent fractions using in-column focusing. *J Chromatogr A* **2016,** *1427*, 90-5.

39. Hsu, S.-H.; Raglione, T.; Tomellini, S. A.; Floyd, T. R.; Sagliano, N.; Hartwick, R. A., Zone compressesion effects in high-performance liquid chromatography. *Journal of Chromatography A* **1986,** *367*, 293-300.

40. De Vos, J.; Desmet, G.; Eeltink, S., A generic approach to post-column refocusing in liquid chromatography. *Journal of Chromatography A* **2014,** *1360*, 164-171.

41. De Vos, J.; Eeltink, S.; Desmet, G., Peak refocusing using subsequent retentive trapping and strong eluent remobilization in liquid chromatography: a theoretical optimization study. *J Chromatogr A* **2015,** *1381*, 74-86.

42. Groskreutz, S. R.; Weber, S. G., Temperature-assisted on-column solute focusing: a general method to reduce pre-column dispersion in capillary high performance liquid chromatography. *J Chromatogr A* **2014,** *1354*, 65-74.

43. Groskreutz, S. R.; Horner, A. R.; Weber, S. G., Temperature-based on-column solute focusing in capillary liquid chromatography reduces peak broadening from pre-column dispersion and volume overload when used alone or with solvent-based focusing. *J Chromatogr A* **2015,** *1405*, 133-9.

44. Wilson, R. E.; Groskreutz, S. R.; Weber, S. G., Improving the Sensitivity, Resolution, and Peak Capacity of Gradient Elution in Capillary Liquid Chromatography with Large-Volume Injections by Using Temperature-Assisted On-Column Solute Focusing. *Analytical Chemistry* **2016,** *88* (10), 5112-5121.

45. Rerick, M. T.; Groskreutz, S. R.; Weber, S. G., Multiplicative On-Column Solute Focusing Using Spatially Dependent Temperature Programming for Capillary HPLC. *Analytical Chemistry* **2019,** *91* (4), 2854-2860.

46. Groskreutz, S. R.; Weber, S. G., Temperature-assisted solute focusing with sequential trap/release zones in isocratic and gradient capillary liquid chromatography: Simulation and experiment. *J Chromatogr A* **2016,** *1474*, 95-108.

47. Groskreutz, S. R.; Weber, S. G., Quantitative evaluation of models for solvent-based, on-column focusing in liquid chromatography. *J Chromatogr A* **2015,** *1409*, 116-24.

48. Snyder, L. R.; Saunders, D. L., Optimized Solvent Programming for Separations of Complex Samples by Liquid-Solid Adsorption Chromatography in Columns. *Journal of Chromatographic Science* **1969,** *7* (4), 195-208.

49. Vukmanic, D.; Chiba, M., Effect of organic solvents in sample solutions and injection volumes on chromatographic peak profiles of analytes in reversed-phase high-performance liquid chromatography. *Journal of Chromatography A* **1989,** *483*, 189-196.

50. Layne, J.; Farcas, T.; Rustamov, I.; Ahmed, F., Volume-load capacity in fast-gradient liquid chromatography: Effect of sample solvent composition and injection volume on chromatographic performance. *Journal of Chromatography A* **2001,** *913* (1), 233-242.

51. Ishihama, Y., Proteomic LC-MS systems using nanoscale liquid chromatography with tandem mass spectrometry. *J Chromatogr A* **2005,** *1067* (1-2), 73-83.

52. Washburn, M. P.; Wolters, D.; Yates, J. R., Large-scale analysis of the yeast proteome by multidimensional protein identification technology. *Nature Biotechnology* **2001,** *19* (3), 242-247.

53. Wolters, D. A.; Washburn, M. P.; Yates, J. R., An Automated Multidimensional Protein Identification Technology for Shotgun Proteomics. *Analytical Chemistry* **2001,** *73* (23), 5683-5690.

54. Haskins, W. E.; Wang, Z.; Watson, C. J.; Rostand, R. R.; Witowski, S. R.; Powell, D. H.; Kennedy, R. T., Capillary LC-MS2 at the attomole level for monitoring and discovering endogenous peptides in microdialysis samples collected in vivo. *Anal Chem* **2001,** *73* (21), 5005-14.

55. Zhou, Y.; Mabrouk, O. S.; Kennedy, R. T., Rapid Preconcentration for Liquid Chromatography–Mass Spectrometry Assay of Trace Level Neuropeptides. *Journal of The American Society for Mass Spectrometry* **2013,** *24* (11), 1700-1709.

56. Maes, K.; Béchade, G.; Van Schoors, J.; Van Wanseele, Y.; Van Liefferinge, J.; Michotte, Y.; Harden, S. N.; Chambers, E. E.; Claereboudt, J.; Smolders, I.; Van Eeckhaut, A., An ultrasensitive nano UHPLC-ESI-MS/MS method for the quantification of three neuromedin-like peptides in microdialysates. *Bioanalysis* **2015,** *7* (5), 605-19.

57. McKenzie, J. A. M.; Watson, C. J.; Rostand, R. D.; German, I.; Witowski, S. R.; Kennedy, R. T., Automated capillary liquid chromatography for simultaneous determination of neuroactive amines and amino acids. *Journal of Chromatography A* **2002,** *962* (1), 105-115.

58. Cooper, B. R.; Mark Wightman, R.; Jorgenson, J. W., Quantitation of epinephrine and norepinephrine secretion from individual adrenal medullary cells by microcolumn high-performance liquid chromatography. *Journal of Chromatography B: Biomedical Sciences and Applications* **1994,** *653* (1), 25-34.

59. Prokai, L.; Kim, H.-S.; Zharikova, A.; Roboz, J.; Ma, L.; Deng, L.; Simonsick Jr, W. J., Electrospray ionization mass spectrometric and liquid chromatographic–mass spectrometric studies on the metabolism of synthetic dynorphin A peptides in brain tissue in vitro and in vivo. *Journal of Chromatography A* **1998,** *800* (1), 59-68.

60. Ho, C. S.; Lam, C. W. K.; Chan, M. H. M.; Cheung, R. C. K.; Law, L. K.; Lit, L. C. W.; Ng, K. F.; Suen, M. W. M.; Tai, H. L., Electrospray ionisation mass spectrometry: principles and clinical applications. *Clin Biochem Rev* **2003,** *24* (1), 3-12.

61. Perry, M.; Li, Q.; Kennedy, R. T., Review of recent advances in analytical techniques for the determination of neurotransmitters. *Anal Chim Acta* **2009,** *653* (1), 1-22.

62. Buchberger, A.; Yu, Q.; Li, L., Advances in Mass Spectrometric Tools for Probing Neuropeptides. *Annual Review of Analytical Chemistry* **2015,** *8* (1), 485-509.

63. Gaddem, J., Push-pull cannulae. *J. Physiol.* **1961,** *155*, 1-2.

64. MYERS, R. D., Development of Push-Pull Systems for Perfusion of Anatomically Distinct Regions of the Brain of the Awake Animala. *Annals of the New York Academy of Sciences* **1986,** *473* (1), 21-41.

65. Thongkhao-on, K.; Wirtshafter, D.; Shippy, S. A., Feeding specific glutamate surge in the rat lateral hypothalamus revealed by low-flow push-pull perfusion. *Pharmacol Biochem Behav* **2008,** *89* (4), 591-597.

66. Patterson Ii, E. E.; Pritchett, J. S.; Shippy, S. A., High temporal resolution coupling of low-flow push-pull perfusion to capillary electrophoresis for ascorbate analysis at the rat vitreoretinal interface. *Analyst* **2009,** *134* (2), 401-406.

67. Slaney, T. R.; Nie, J.; Hershey, N. D.; Thwar, P. K.; Linderman, J.; Burns, M. A.; Kennedy, R. T., Push-pull perfusion sampling with segmented flow for high temporal and spatial resolution in vivo chemical monitoring. *Anal Chem* **2011,** *83* (13), 5207-13.

68. Kottegoda, S.; Shaik, I.; Shippy, S. A., Demonstration of low flow push–pull perfusion. *J Neurosci Methods* **2002,** *121* (1), 93-101.

69. Kottegoda, S.; Pulido, J. S.; Thongkhao-on, K.; Shippy, S. A. Demonstration and use of nanoliter sampling of in vivo rat vitreous and vitreoretinal interface *Mol Vis* [Online], 2007, p. 2073-2082. PubMed. http://europepmc.org/abstract/MED/18079681 (accessed 2007/11//).

70. Redgrave, P., A modified push-pull system for the localised perfusion of brain tissue. *Pharmacology Biochemistry and Behavior* **1977,** *6* (4), 471-474.

71. Dluzen, D. E.; Ramirez, V. D., A miniaturized push-pull cannula for use in conscious, unrestrained animals. *Pharmacology Biochemistry and Behavior* **1986,** *24* (1), 147-150.

72. Zhang, X.; Myers, R.; Wooles, W., New triple microbore cannula system for push-pull perfusion of brain nuclei of the rat. *J Neurosci Methods* **1990,** *32* (2), 93-104.

73. Zhang, X.; Wulfert, E.; Hanin, I., Development of a sensitive and inexpensive micropush—pull technique for the continuous analysis of brain neurotransmitters and metabolites in vivo. *J Neurosci Methods* **1992,** *42* (1-2), 139-147.

74. Kottegoda, S.; Shaik, I.; Shippy, S. A., Demonstration of low flow push-pull perfusion. *J Neurosci Methods* **2002,** *121* (1), 93-101.

75. Davies, M. I.; Cooper, J. D.; Desmond, S. S.; Lunte, C. E.; Lunte, S. M., Analytical considerations for microdialysis sampling. *Advanced Drug Delivery Reviews* **2000,** *45* (2), 169-188.

76. Ungerstedt, U.; Hallström, Å., In vivo microdialysis - a new approach to the analysis of neurotransmitters in the brain. *Life Sciences* **1987,** *41* (7), 861-864.

77. Badiani, A.; Oates, M. M.; Day, H. E. W.; Watson, S. J.; Akil, H.; Robinson, T. E., Amphetamine-Induced Behavior, Dopamine Release, and c-fos mRNA Expression: Modulation by Environmental Novelty. *The Journal of Neuroscience* **1998,** *18* (24), 10579.

78. Gunduz-Bruce, H., The acute effects of NMDA antagonism: From the rodent to the human brain. *Brain Research Reviews* **2009,** *60* (2), 279-286.

79. Jones, D. A.; Parkin, M. C.; Langemann, H.; Landolt, H.; Hopwood, S. E.; Strong, A. J.; Boutelle, M. G., On-line monitoring in neurointensive care: Enzyme-based electrochemical assay for simultaneous, continuous monitoring of glucose and lactate from critical care patients. *Journal of Electroanalytical Chemistry* **2002,** *538-539*, 243-252.

80. Rogers, M. L.; Feuerstein, D.; Leong, C. L.; Takagaki, M.; Niu, X.; Graf, R.; Boutelle, M. G., Continuous Online Microdialysis Using Microfluidic Sensors: Dynamic Neurometabolic Changes during Spreading Depolarization. *ACS Chemical Neuroscience* **2013,** *4* (5), 799-807.

81. Rogers, M. L.; Leong, C. L.; Gowers, S. A. N.; Samper, I. C.; Jewell, S. L.; Khan, A.; McCarthy, L.; Pahl, C.; Tolias, C. M.; Walsh, D. C.; Strong, A. J.; Boutelle, M. G., Simultaneous monitoring of potassium, glucose and lactate during spreading depolarization in the injured human brain – Proof of principle of a novel real-time neurochemical analysis system, continuous online microdialysis. *Journal of Cerebral Blood Flow & Metabolism* **2016,** *37* (5), 1883-1895.

82. Varner, E. L.; Leong, C. L.; Jaquins-Gerstl, A.; Nesbitt, K. M.; Boutelle, M. G.; Michael, A. C., Enhancing Continuous Online Microdialysis Using Dexamethasone: Measurement of Dynamic Neurometabolic Changes during Spreading Depolarization. *ACS Chemical Neuroscience* **2017,** *8* (8), 1779-1788.

83. Robbins, E. M.; Jaquins-Gerstl, A.; Fine, D. F.; Leong, C. L.; Dixon, C. E.; Wagner, A. K.; Boutelle, M. G.; Michael, A. C., Extended (10-Day) Real-Time Monitoring by Dexamethasone-Enhanced Microdialysis in the Injured Rat Cortex. *ACS Chem Neurosci* **2019,** *10* (8), 3521-3531.

84. Filla, L. A.; Yuan, W.; Feldman, E. L.; Li, S.; Edwards, J. L., Global metabolomic and isobaric tagging capillary liquid chromatography-tandem mass spectrometry approaches

for uncovering pathway dysfunction in diabetic mouse aorta. *J Proteome Res* **2014,** *13* (12), 6121-34.

85. Gao, X.; Zhang, Q.; Meng, D.; Isaac, G.; Zhao, R.; Fillmore, T. L.; Chu, R. K.; Zhou, J.; Tang, K.; Hu, Z.; Moore, R. J.; Smith, R. D.; Katze, M. G.; Metz, T. O., A reversed-phase capillary ultra-performance liquid chromatography-mass spectrometry (UPLC-MS) method for comprehensive top-down/bottom-up lipid profiling. *Anal Bioanal Chem* **2012,** *402* (9), 2923-33.

86. Theodoridis, G.; Gika, H. G.; Wilson, I. D., LC-MS-based methodology for global metabolite profiling in metabonomics/metabolomics. *TrAC Trends in Analytical Chemistry* **2008,** *27* (3), 251-260.

87. Ishihama, Y., Proteomic LC–MS systems using nanoscale liquid chromatography with tandem mass spectrometry. *Journal of Chromatography A* **2005,** *1067* (1), 73-83.

88. Wong, J. M.; Malec, P. A.; Mabrouk, O. S.; Ro, J.; Dus, M.; Kennedy, R. T., Benzoyl chloride derivatization with liquid chromatography-mass spectrometry for targeted metabolomics of neurochemicals in biological samples. *J Chromatogr A* **2016,** *1446*, 78-90.

89. Cepeda, D. E.; Hains, L.; Li, D.; Bull, J.; Lentz, S. I.; Kennedy, R. T., Experimental evaluation and computational modeling of tissue damage from low-flow push-pull perfusion sampling in vivo. *J Neurosci Methods* **2015,** *242*, 97-105.

90. Maes, K.; Van Liefferinge, J.; Viaene, J.; Van Schoors, J.; Van Wanseele, Y.; Bechade, G.; Chambers, E. E.; Morren, H.; Michotte, Y.; Vander Heyden, Y.; Claereboudt, J.; Smolders, I.; Van Eeckhaut, A., Improved sensitivity of the nano ultra-high performance liquid chromatography-tandem mass spectrometric analysis of low-concentrated neuropeptides by reducing aspecific adsorption and optimizing the injection solvent. *J Chromatogr A* **2014,** *1360*, 217-28.

91. Groskreutz, S. R.; Weber, S. G., Quantitative evaluation of models for solvent-based, on-column focusing in liquid chromatography. *Journal of Chromatography A* **2015,** *1409* (Supplement C), 116-124.

92. Colin, H.; Martin, M.; Guiochon, G., Extra-column effects in high-performance liquid chromatography: I. Theoretical study of the injection problem. *Journal of Chromatography A* **1979,** *185*, 79-95.

93. Héron, S.; Tchapla, A.; Chervet, J.-P., Influence of injection parameters on column performance in nanoscale high-performance liquid chromatography. *Chromatographia* **2000,** *51* (7-8), 495-499.

94. Mills, M. J.; Maltas, J.; John Lough, W., Assessment of injection volume limits when using on-column focusing with microbore liquid chromatography. *Journal of Chromatography A* **1997,** *759* (1), 1-11.

95. Kucera, P., *Microcolumn high-performance liquid chromatography*. Elsevier ;Distributors for the U.S. and Canada, Elsevier Science Pub. Co.: Amsterdam ; New York, NY, 1984; p xvi, 302 p.

96. Gilar, M.; McDonald, T. S.; Johnson, J. S.; Murphy, J. P.; Jorgenson, J. W., Wide injection zone compression in gradient reversed-phase liquid chromatography. *Journal of Chromatography A* **2015,** *1390*, 86-94.

97. van Deemter, J. J.; Zuiderweg, F. J.; Klinkenberg, A., Longitudinal diffusion and resistance to mass transfer as causes of nonideality in chromatography. *Chemical Engineering Science* **1995,** *50* (24), 3869-3882.

98. Westerink, B. H. C.; Cremers, T. I. F. H., *Handbook of microdialysis : methods, applications and perspectives*. 1st ed.; Elsevier Academic Press: Amsterdam ; Boston, 2007; p xiv, 697 p.

99. Greibrokk, T.; Andersen, T., Temperature programming in liquid chromatography. *Journal of Separation Science* **2001,** *24* (12), 899-909.

100. Collins, D.; Nesterenko, E.; Connolly, D.; Vasquez, M.; Macka, M.; Brabazon, D.; Paull, B., Versatile capillary column temperature control using a thermoelectric array based platform. *Anal Chem* **2011,** *83* (11), 4307-13.

101. Gritti, F., Combined solvent- and non-uniform temperature-programmed gradient liquid chromatography. I – A theoretical investigation. *Journal of Chromatography A* **2016,** *1473*, 38-47.

102. Verstraeten, M.; Pursch, M.; Eckerle, P.; Luong, J.; Desmet, G., Modelling the thermal behaviour of the Low-Thermal Mass Liquid Chromatography system. *Journal of Chromatography A* **2011,** *1218* (16), 2252-2263.

103. Gritti, F.; Guiochon, G., Performance of new prototype packed columns for very high pressure liquid chromatography. *Journal of Chromatography A* **2010,** *1217* (9), 1485-1495.

104. Gritti, F.; Guiochon, G., Measurement of the axial and radial temperature profiles of a chromatographic column: Influence of thermal insulation on column efficiency. *Journal of Chromatography A* **2007,** *1138* (1), 141-157.

105. Gritti, F.; Guiochon, G., Mass transfer resistance in narrow-bore columns packed with 1.7µm particles in very high pressure liquid chromatography. *Journal of Chromatography A* **2010,** *1217* (31), 5069-5083.

106. Larsen, Å.; Molander, P., Temperature optimization for improved determination of phosphatidylserine species by micro liquid chromatography with electrospray tandem mass spectrometric detection. *Journal of Separation Science* **2004,** *27* (4), 297-303.

107. Molander, P.; Holm, A.; Lundanes, E.; Hegna, D. R.; Ommundsen, E.; Greibrokk, T., Temperature-promoted large-volume solute enrichment in column-switching miniaturized liquid chromatography: Determination of an antioxidant. *Analyst* **2002,** *127* (7), 892-897.

108. Molander, P.; Thommesen, S. J.; Bruheim, I. A.; Trones, R.; Greibrokk, T.; Lundanes, E.; Gundersen, T. E., Temperature-programmed packed capillary liquid chromatography separation with large volume on-column focusing of retinyl esters. *Journal of High Resolution Chromatography* **1999,** *22* (9), 490-494.

109. Eghbali, H.; Sandra, K.; Tienpont, B.; Eeltink, S.; Sandra, P.; Desmet, G., Exploring the possibilities of cryogenic cooling in liquid chromatography for biological applications: a proof of principle. *Anal Chem* **2012,** *84* (4), 2031-7.

110. Young, C.; Podtelejnikov, A. V.; Nielsen, M. L., Improved Reversed Phase Chromatography of Hydrophilic Peptides from Spatial and Temporal Changes in Column Temperature. *J Proteome Res* **2017,** *16* (6), 2307-2317.

111. Wilson, R. E.; Groskreutz, S. R.; Weber, S. G., Improving the Sensitivity, Resolution, and Peak Capacity of Gradient Elution in Capillary Liquid Chromatography With Large-Volume Injections by Using Temperature-Assisted On-column Solute Focusing. *Analytical Chemistry* **2016**.

112. Groskreutz, S. R.; Weber, S. G., Temperature-assisted on-column solute focusing: A general method to reduce pre-column dispersion in capillary high performance liquid chromatography. *Journal of Chromatography A* **2014,** *1354*, 65-74.

113. Groskreutz, S. R.; Horner, A. R.; Weber, S. G., Temperature-based on-column solute focusing in capillary liquid chromatography reduces peak broadening from pre-column dispersion and volume overload when used alone or with solvent-based focusing. *Journal of Chromatography A* **2015,** *1405*, 133-139.

114. Neue, U. D.; Kuss, H. J., Improved reversed-phase gradient retention modeling. *J Chromatogr A* **2010,** *1217* (24), 3794-803.

115. Zarzycki, P. K.; Wlodarczyk, E.; Lou, D.-W.; JINNO, K., Evaluation of methanol-water and acetonitrile-water binary mixtures as eluents for temperature-dependent inclusion chromatography. *Analytical sciences* **2006,** *22* (3), 453-456.

116. Sternberg, J., *Advances in Chromatography*. Marcel Dekker: New York, 1966.

117. Ford, C. P., The role of D2-autoreceptors in regulating dopamine neuron activity and transmission. *Neuroscience* **2014,** *282*, 13-22.

118. Murphy, D. L.; Lesch, K. P., Targeting the murine serotonin transporter: insights into human neurobiology. *Nat Rev Neurosci* **2008,** *9* (2), 85-96.

119. Meeter, M.; Talamini, L.; Schmitt, J. A. J.; Riedel, W. J., Effects of 5-HT on Memory and the Hippocampus: Model and Data. *Neuropsychopharmacology* **2006,** *31* (4), 712-720.

120. Hahn, M. K.; Blakely, R. D., Monoamine transporter gene structure and polymorphisms in relation to psychiatric and other complex disorders. *The Pharmacogenomics Journal* **2002,** *2* (4), 217-235.

121. Garris, P.; Wightman, M., Regional Differences in Dopamine Release, Uptake, and Diffusion Measured by Fast-Scan Cyclic Voltammetry. 2008; pp 179-220.

122. Stein, M. B.; Andrews, A. M., Serotonin States and Social Anxiety. *JAMA Psychiatry* **2015,** *72* (8), 845-7.

123. Lotharius, J.; Brundin, P., Pathogenesis of Parkinson's disease: dopamine, vesicles and alpha-synuclein. *Nat Rev Neurosci* **2002,** *3* (12), 932-42.

124. Denys, D.; Zohar, J.; Westenberg, H. G., The role of dopamine in obsessive-compulsive disorder: preclinical and clinical evidence. *J Clin Psychiatry* **2004,** *65 Suppl 14*, 11-7.

125. Denys, D.; de Vries, F.; Cath, D.; Figee, M.; Vulink, N.; Veltman, D. J.; van der Doef, T. F.; Boellaard, R.; Westenberg, H.; van Balkom, A.; Lammertsma, A. A.; van Berckel, B. N., Dopaminergic activity in Tourette syndrome and obsessive-compulsive disorder. *Eur Neuropsychopharmacol* **2013,** *23* (11), 1423-31.

126. Figee, M.; de Koning, P.; Klaassen, S.; Vulink, N.; Mantione, M.; van den Munckhof, P.; Schuurman, R.; van Wingen, G.; van Amelsvoort, T.; Booij, J.; Denys, D., Deep brain stimulation induces striatal dopamine release in obsessive-compulsive disorder. *Biol Psychiatry* **2014,** *75* (8), 647-52.

127. Andrews, A. M.; Weiss, P. S., Nano in the brain: nano-neuroscience. ACS Publications: 2012.

128. Alivisatos, A. P.; Andrews, A. M.; Boyden, E. S.; Chun, M.; Church, G. M.; Deisseroth, K.; Donoghue, J. P.; Fraser, S. E.; Lippincott-Schwartz, J.; Looger, L. L., Nanotools for neuroscience and brain activity mapping. *ACS nano* **2013,** *7* (3), 1850-1866.

129. Borue, X.; Condron, B.; Venton, B. J., Both synthesis and reuptake are critical for replenishing the releasable serotonin pool in Drosophila. *Journal of neurochemistry* **2010,** *113* (1), 188-199.

130. Borue, X.; Cooper, S.; Hirsh, J.; Condron, B.; Venton, B. J., Quantitative evaluation of serotonin release and clearance in Drosophila. *J Neurosci Methods* **2009,** *179* (2), 300-8.

131. Robinson, D. L.; Venton, B. J.; Heien, M. L. A. V.; Wightman, R. M., Detecting Subsecond Dopamine Release with Fast-Scan Cyclic Voltammetry in Vivo. *Clinical Chemistry* **2003,** *49* (10), 1763-1773.

132. Westerink, B. H.; Cremers, T. I., *Handbook of microdialysis: methods, applications and perspectives*. Elsevier: 2007.

133. Song, P.; Mabrouk, O. S.; Hershey, N. D.; Kennedy, R. T., In vivo neurochemical monitoring using benzoyl chloride derivatization and liquid chromatography-mass spectrometry. *Analytical chemistry* **2012,** *84* (1), 412-419.

134. Yang, H.; Thompson, A. B.; McIntosh, B. J.; Altieri, S. C.; Andrews, A. M., Physiologically relevant changes in serotonin resolved by fast microdialysis. *ACS Chem Neurosci* **2013,** *4* (5), 790-8.

135. Newton, A. P.; Justice, J. B., Temporal Response of Microdialysis Probes to Local Perfusion of Dopamine and Cocaine Followed with One-Minute Sampling. *Analytical Chemistry* **1994,** *66* (9), 1468-1472.

136. Schultz, K. N.; Kennedy, R. T., Time-resolved microdialysis for in vivo neurochemical measurements and other applications. *Annu Rev Anal Chem (Palo Alto Calif)* **2008,** *1*, 627-61.

137. Liu, Y.; Zhang, J.; Xu, X.; Zhao, M. K.; Andrews, A. M.; Weber, S. G., Capillary ultrahigh performance liquid chromatography with elevated temperature for sub-one minute separations of basal serotonin in submicroliter brain microdialysate samples. *Analytical chemistry* **2010,** *82* (23), 9611-9616.

138. Zhang, J.; Liu, Y.; Jaquins-Gerstl, A.; Shu, Z.; Michael, A. C.; Weber, S. G., Optimization for speed and sensitivity in capillary high performance liquid chromatography. The importance of column diameter in online monitoring of serotonin by microdialysis. *Journal of Chromatography A* **2012,** *1251*, 54-62.

139. Zhang, J.; Jaquins-Gerstl, A.; Nesbitt, K. M.; Rutan, S. C.; Michael, A. C.; Weber, S. G., In Vivo Monitoring of Serotonin in the Striatum of Freely Moving Rats with One Minute Temporal Resolution by Online Microdialysis–Capillary High-Performance Liquid Chromatography at Elevated Temperature and Pressure. *Analytical Chemistry* **2013,** *85* (20), 9889-9897.

140. Persson, B. A., LIQUID CHROMATOGRAPHY | Ion Pair. In *Encyclopedia of Analytical Science (Second Edition)*, Worsfold, P.; Townshend, A.; Poole, C., Eds. Elsevier: Oxford, 2005; pp 157-164.

141. Verstraeten, M.; Pursch, M.; Eckerle, P.; Luong, J.; Desmet, G., Modelling the thermal behaviour of the low-thermal mass liquid chromatography system. *J Chromatogr A* **2011,** *1218* (16), 2252-63.

142. Grinias, J. P.; Kennedy, R. T., Evaluation of 5 microm Superficially Porous Particles for Capillary and Microfluidic LC Columns. *Chromatography (Basel)* **2015,** *2* (3), 502-514.

143. Paxinos, G.; Watson, C., The Rat Brain in Stereotaxic Coordinates, 4th edn Academic Press: San Diego. CA: 1998.

144. Peterson, A. B.; Zhou, H.; Thomas, K. E.; Daugherty, J. *Traumatic Brain Injury-related Hospitalizations and Deaths by Age Group, Sex, and Mechanism of Injury - United States,*

2016 and 2017; Centers for Disease Control and Prevention, U.S. Department of Heath and Human Services: Atlanta, GA, 2021.

145. Ayata, C.; Lauritzen, M., Spreading Depression, Spreading Depolarizations, and the Cerebral Vasculature. *Physiol Rev* **2015,** *95* (3), 953-993.

146. Dreier, J. P., The role of spreading depression, spreading depolarization and spreading ischemia in neurological disease. *Nature Medicine* **2011,** *17* (4), 439-447.

147. Nakamura, H.; Strong, A. J.; Dohmen, C.; Sakowitz, O. W.; Vollmar, S.; Sué, M.; Kracht, L.; Hashemi, P.; Bhatia, R.; Yoshimine, T.; Dreier, J. P.; Dunn, A. K.; Graf, R., Spreading depolarizations cycle around and enlarge focal ischaemic brain lesions. *Brain* **2010,** *133* (Pt 7), 1994-2006.

148. Dreier, J. P., The role of spreading depression, spreading depolarization and spreading ischemia in neurological disease. *Nat Med* **2011,** *17* (4), 439-47.

149. Dreier, J. P.; Fabricius, M.; Ayata, C.; Sakowitz, O. W.; Shuttleworth, C. W.; Dohmen, C.; Graf, R.; Vajkoczy, P.; Helbok, R.; Suzuki, M.; Schiefecker, A. J.; Major, S.; Winkler, M. K.; Kang, E. J.; Milakara, D.; Oliveira-Ferreira, A. I.; Reiffurth, C.; Revankar, G. S.; Sugimoto, K.; Dengler, N. F.; Hecht, N.; Foreman, B.; Feyen, B.; Kondziella, D.; Friberg, C. K.; Piilgaard, H.; Rosenthal, E. S.; Westover, M. B.; Maslarova, A.; Santos, E.; Hertle, D.; Sánchez-Porras, R.; Jewell, S. L.; Balança, B.; Platz, J.; Hinzman, J. M.; Lückl, J.; Schoknecht, K.; Schöll, M.; Drenckhahn, C.; Feuerstein, D.; Eriksen, N.; Horst, V.; Bretz, J. S.; Jahnke, P.; Scheel, M.; Bohner, G.; Rostrup, E.; Pakkenberg, B.; Heinemann, U.; Claassen, J.; Carlson, A. P.; Kowoll, C. M.; Lublinsky, S.; Chassidim, Y.; Shelef, I.; Friedman, A.; Brinker, G.; Reiner, M.; Kirov, S. A.; Andrew, R. D.; Farkas, E.; Güresir, E.; Vatter, H.; Chung, L. S.; Brennan, K. C.; Lieutaud, T.; Marinesco, S.; Maas, A. I.; Sahuquillo, J.; Dahlem, M. A.; Richter, F.; Herreras, O.; Boutelle, M. G.; Okonkwo, D. O.; Bullock, M. R.; Witte, O. W.; Martus, P.; van den Maagdenberg, A. M.; Ferrari, M. D.; Dijkhuizen, R. M.; Shutter, L. A.; Andaluz, N.; Schulte, A. P.; MacVicar, B.; Watanabe, T.; Woitzik, J.; Lauritzen, M.; Strong, A. J.; Hartings, J. A., Recording, analysis, and interpretation of spreading depolarizations in neurointensive care: Review and recommendations of the COSBID research group. *J Cereb Blood Flow Metab* **2017,** *37* (5), 1595-1625.

150. Feuerstein, D.; Manning, A.; Hashemi, P.; Bhatia, R.; Fabricius, M.; Tolias, C.; Pahl, C.; Ervine, M.; Strong, A. J.; Boutelle, M. G., Dynamic metabolic response to multiple spreading depolarizations in patients with acute brain injury: an online microdialysis study. *J Cereb Blood Flow Metab* **2010,** *30* (7), 1343-55.

151. Fabricius, M.; Fuhr, S.; Bhatia, R.; Boutelle, M.; Hashemi, P.; Strong, A. J.; Lauritzen, M., Cortical spreading depression and peri-infarct depolarization in acutely injured human cerebral cortex. *Brain* **2006,** *129* (Pt 3), 778-90.

152. Hartings, J. A.; Watanabe, T.; Bullock, M. R.; Okonkwo, D. O.; Fabricius, M.; Woitzik, J.; Dreier, J. P.; Puccio, A.; Shutter, L. A.; Pahl, C.; Strong, A. J., Spreading

depolarizations have prolonged direct current shifts and are associated with poor outcome in brain trauma. *Brain* **2011,** *134* (Pt 5), 1529-40.

153. Hartings, J. A.; Bullock, M. R.; Okonkwo, D. O.; Murray, L. S.; Murray, G. D.; Fabricius, M.; Maas, A. I.; Woitzik, J.; Sakowitz, O.; Mathern, B.; Roozenbeek, B.; Lingsma, H.; Dreier, J. P.; Puccio, A. M.; Shutter, L. A.; Pahl, C.; Strong, A. J., Spreading depolarisations and outcome after traumatic brain injury: a prospective observational study. *Lancet Neurol* **2011,** *10* (12), 1058-64.

154. Papadimitriou, K. I.; Wang, C.; Rogers, M. L.; Gowers, S. A. N.; Leong, C. L.; Boutelle, M. G.; Drakakis, E. M., High-Performance Bioinstrumentation for Real-Time Neuroelectrochemical Traumatic Brain Injury Monitoring. *Front Hum Neurosci* **2016,** *10*, 212-212.

155. Benveniste, H.; Diemer, N. H., Cellular reactions to implantation of a microdialysis tube in the rat hippocampus. *Acta Neuropathologica* **1987,** *74* (3), 234-238.

156. Zhou, F.; Zhu, X.; Castellani, R. J.; Stimmelmayr, R.; Perry, G.; Smith, M. A.; Drew, K. L., Hibernation, a model of neuroprotection. *Am J Pathol* **2001,** *158* (6), 2145-2151.

157. Lu, Y.; Peters, J. L.; Michael, A. C., Direct comparison of the response of voltammetry and microdialysis to electrically evoked release of striatal dopamine. *J Neurochem* **1998,** *70* (2), 584-93.

158. Borland, L. M.; Shi, G.; Yang, H.; Michael, A. C., Voltammetric study of extracellular dopamine near microdialysis probes acutely implanted in the striatum of the anesthetized rat. *J Neurosci Methods* **2005,** *146* (2), 149-58.

159. Jaquins-Gerstl, A.; Michael, A. C., Comparison of the brain penetration injury associated with microdialysis and voltammetry. *J Neurosci Methods* **2009,** *183* (2), 127-135.

160. Jaquins-Gerstl, A.; Shu, Z.; Zhang, J.; Liu, Y.; Weber, S. G.; Michael, A. C., Effect of Dexamethasone on Gliosis, Ischemia, and Dopamine Extraction during Microdialysis Sampling in Brain Tissue. *Analytical Chemistry* **2011,** *83* (20), 7662-7667.

161. Kozai, T. D. Y.; Jaquins-Gerstl, A. S.; Vazquez, A. L.; Michael, A. C.; Cui, X. T., Dexamethasone retrodialysis attenuates microglial response to implanted probes in vivo. *Biomaterials* **2016,** *87*, 157-169.

162. Robinson, T. E.; Camp, D. M., The effects of four days of continuous striatal microdialysis on indices of dopamine and serotonin neurotransmission in rats. *J Neurosci Methods* **1991,** *40* (2), 211-222.

163. Holson, R. R.; Bowyer, J. F.; Clausing, P.; Gough, B., Methamphetamine-stimulated striatal dopamine release declines rapidly over time following microdialysis probe insertion. *Brain Res* **1996,** *739* (1-2), 301-7.

164. Holson, R. R.; Gazzara, R. A.; Gough, B., Declines in stimulated striatal dopamine release over the first 32 h following microdialysis probe insertion: generalization across releasing mechanisms. *Brain Res* **1998,** *808* (2), 182-9.

165. Nesbitt, K. M.; Jaquins-Gerstl, A.; Skoda, E. M.; Wipf, P.; Michael, A. C., Pharmacological Mitigation of Tissue Damage during Brain Microdialysis. *Analytical Chemistry* **2013,** *85* (17), 8173-8179.

166. Nesbitt, K. M.; Varner, E. L.; Jaquins-Gerstl, A.; Michael, A. C., Microdialysis in the rat striatum: effects of 24 h dexamethasone retrodialysis on evoked dopamine release and penetration injury. *ACS chemical neuroscience* **2015,** *6* (1), 163-173.

167. Varner, E. L.; Jaquins-Gerstl, A.; Michael, A. C., Enhanced Intracranial Microdialysis by Reduction of Traumatic Penetration Injury at the Probe Track. *ACS Chemical Neuroscience* **2016,** *7* (6), 728-736.

168. Koehler, C. J.; Arntzen, M. Ø.; de Souza, G. A.; Thiede, B., An approach for triplex-isobaric peptide termini labeling (triplex-IPTL). *Analytical chemistry* **2013,** *85* (4), 2478-2485.

169. Wilson, R. E.; Jaquins-Gerstl, A.; Weber, S. G., On-Column Dimethylation with Capillary Liquid Chromatography-Tandem Mass Spectrometry for Online Determination of Neuropeptides in Rat Brain Microdialysate. *Analytical Chemistry* **2018,** *90* (7), 4561-4568.

170. Wilson, R. E.; Jaquins-Gerstl, A.; Chen, J.; Rerick, M.; Weber, S. G., Electroosmotic Perfusion–Microdialysis Probe Created by Direct Laser Writing for Quantitative Assessment of Leucine Enkephalin Hydrolysis by Insulin-Regulated Aminopeptidase in Vivo. *Analytical Chemistry* **2020,** *92* (21), 14558-14567.

171. Konkoy, C. S.; Davis, T. P., Ectoenzymes as sites of peptide regulation. *Trends in Pharmacological Sciences* **1996,** *17* (8), 288-294.

172. Pollard, H.; Bouthenet, M. L.; Moreau, J.; Souil, E.; Verroust, P.; Ronco, P.; Schwartz, J. C., Detailed immunoautoradiographic mapping of enkephalinase (EC 3.4.24.11) in rat central nervous system: Comparison with enkephalins and substance P. *Neuroscience* **1989,** *30* (2), 339-376.

173. Ziaber, J.; Baj, Z.; Paśnik, J.; Chmielewski, H.; Tchórzewski, H., Increased expression of neutral endopeptidase (NEP) and aminopeptidase N (APN) on peripheral blood mononuclear cells in patients with multiple sclerosis. *Immunol Lett* **2000,** *71* (2), 127-9.

174. Reinhold, D.; Goihl, A.; Wrenger, S.; Reinhold, A.; Kühlmann, U. C.; Faust, J.; Neubert, K.; Thielitz, A.; Brocke, S.; Täger, M.; Ansorge, S.; Bank, U., Role of dipeptidyl peptidase IV (DP IV)-like enzymes in T lymphocyte activation: investigations in DP IV/CD26-knockout mice. *Clinical Chemistry and Laboratory Medicine* **2009,** *47* (3), 268-274.

175. Hafler, D. A.; Fox, D. A.; Manning, M. E.; Schlossman, S. F.; Reinherz, E. L.; Weiner, H. L., In vivo activated T lymphocytes in the peripheral blood and cerebrospinal fluid of patients with multiple sclerosis. *N Engl J Med* **1985,** *312* (22), 1405-11.

176. Riemann, D.; Schwachula, A.; Hentschel, M.; Langner, J., Demonstration of CD13/aminopeptidase N on synovial fluid T cells from patients with different forms of joint effusions. *Immunobiology* **1993,** *187* (1-2), 24-35.

177. Mizokami, A.; Eguchi, K.; Kawakami, A.; Ida, H.; Kawabe, Y.; Tsukada, T.; Aoyagi, T.; Maeda, K.; Morimoto, C.; Nagataki, S., Increased population of high fluorescence 1F7 (CD26) antigen on T cells in synovial fluid of patients with rheumatoid arthritis. *J Rheumatol* **1996,** *23* (12), 2022-6.

178. Cutrona, G.; Leanza, N.; Ulivi, M.; Melioli, G.; Burgio, V. L.; Mazzarello, G.; Gabutti, G.; Roncella, S.; Ferrarini, M., Expression of CD10 by Human T Cells That Undergo Apoptosis Both In Vitro and In Vivo. *Blood* **1999,** *94* (9), 3067-3076.

179. Antczak, C.; De Meester, I.; Bauvois, B., Ectopeptidases in pathophysiology. *Bioessays* **2001,** *23* (3), 251-260.

180. Mentlein, R., Cell-surface peptidases. *Int Rev Cytol* **2004,** *235*, 165-213.

181. Kohsaka, A.; Watanobe, H.; Kakizaki, Y.; Suda, T., A comparative study of the effects of nitric oxide and carbon monoxide on the in vivo release of gonadotropin-releasing hormone and neuropeptide Y from rat hypothalamus during the estradiol-induced luteinizing hormone surge: estimation by push-pull perfusion. *Neuroendocrinology* **1999,** *69* (4), 245-53.

182. Mizuno, M.; Gearing, M.; Terasawa, E., The Role of Neuropeptide Y in the Progesterone-Induced Luteinizing Hormone-Releasing Hormone Surge in Vivo in Ovariectomized Female Rhesus Monkeys*. *Endocrinology* **2000,** *141* (5), 1772-1779.

183. Kent, P.; Anisman, H.; Merali, Z., Central bombesin activates the hypothalamic-pituitary-adrenal axis. Effects on regional levels and release of corticotropin-releasing hormone and arginine-vasopressin. *Neuroendocrinology* **2001,** *73* (3), 203-14.

184. Johnson, R. D.; Justice, J. B., Model studies for brain dialysis. *Brain Research Bulletin* **1983,** *10* (4), 567-571.

185. Stenken, J. A.; Holunga, D. M.; Decker, S. A.; Sun, L., Experimental and Theoretical Microdialysis Studies of in Situ Metabolism. *Analytical Biochemistry* **2001,** *290* (2), 314-323.

186. Bungay, P. M.; Morrison, P. F.; Dedrick, R. L., Steady-state theory for quantitative microdialysis of solutes and water in vivo and in vitro. *Life Sciences* **1990,** *46* (2), 105-119.

187. Buividas, R.; Rekštytė, S.; Malinauskas, M.; Juodkazis, S., Nano-groove and 3D fabrication by controlled avalanche using femtosecond laser pulses. *Opt. Mater. Express* **2013,** *3* (10), 1674-1686.

188. Kirsanske, G.; Rekštytė, S.; Jonavičius, T.; Kaziulionytė, E.; Jonušauskas, L.; Žukauskas, A.; Gadonas, R.; Piskarskas, A., Nanophotonic lithography: A versatile tool for manufacturing functional three-dimensional micro-/nano-objects. *Lithuanian Journal of Physics and Technical Sciences* **2012,** *52*, 312-326.

189. Aksit, A.; Arteaga, D. N.; Arriaga, M.; Wang, X.; Watanabe, H.; Kasza, K. E.; Lalwani, A. K.; Kysar, J. W., In-vitro perforation of the round window membrane via direct 3-D printed microneedles. *Biomed Microdevices* **2018,** *20* (2), 47.

190. Faraji Rad, Z.; Nordon, R. E.; Anthony, C. J.; Bilston, L.; Prewett, P. D.; Arns, J.-Y.; Arns, C. H.; Zhang, L.; Davies, G. J. High-fidelity replication of thermoplastic microneedles with open microfluidic channels *Microsyst Nanoeng* [Online], 2017, p. 17034.

191. Hermans, S. J.; Ascher, D. B.; Hancock, N. C.; Holien, J. K.; Michell, B. J.; Chai, S. Y.; Morton, C. J.; Parker, M. W., Crystal structure of human insulin-regulated aminopeptidase with specificity for cyclic peptides. *Protein Science* **2015,** *24* (2), 190-199.

192. Edell, D. J.; Toi, V. V.; McNeil, V. M.; Clark, L. D., Factors influencing the biocompatibility of insertable silicon microshafts in cerebral cortex. *IEEE Trans Biomed Eng* **1992,** *39* (6), 635-43.

193. Faraji, A. H.; Jaquins-Gerstl, A. S.; Valenta, A. C.; Ou, Y.; Weber, S. G., Electrokinetic Convection-Enhanced Delivery of Solutes to the Brain. *ACS Chemical Neuroscience* **2020,** *11* (14), 2085-2093.

194. Ou, Y.; Weber, S. G., Numerical Modeling of Electroosmotic Push–Pull Perfusion and Assessment of Its Application to Quantitative Determination of Enzymatic Activity in the Extracellular Space of Mammalian Tissue. *Analytical Chemistry* **2017,** *89* (11), 5864-5873.

195. Mitala, C. M.; Wang, Y.; Borland, L. M.; Jung, M.; Shand, S.; Watkins, S.; Weber, S. G.; Michael, A. C., Impact of microdialysis probes on vasculature and dopamine in the rat striatum: A combined fluorescence and voltammetric study. *J Neurosci Methods* **2008,** *174* (2), 177-185.

196. Kirby, B. J.; Hasselbrink Jr., E. F., Zeta potential of microfluidic substrates: 1. Theory, experimental techniques, and effects on separations. *ELECTROPHORESIS* **2004,** *25* (2), 187-202.

197. Ou, Y.; Wu, J.; Sandberg, M.; Weber, S. G., Electroosmotic perfusion of tissue: sampling the extracellular space and quantitative assessment of membrane-bound enzyme activity in organotypic hippocampal slice cultures. *Anal Bioanal Chem* **2014,** *406* (26), 6455-6468.

198. Guy, Y.; Sandberg, M.; Weber, S. G., Determination of zeta-potential in rat organotypic hippocampal cultures. *Biophys J* **2008,** *94* (11), 4561-9.

199. Syková, E.; Nicholson, C., Diffusion in brain extracellular space. *Physiol Rev* **2008,** *88* (4), 1277-340.

200. Rice, M. E. N., C. , *Voltammetry Methods Brain Syst.* **1994**, 27-79.

201. Rice, M. E.; Gerhardt, G. A.; Hierl, P. M.; Nagy, G.; Adams, R. N., Diffusion coefficients of neurotransmitters and their metabolites in brain extracellular fluid space. *Neuroscience* **1985,** *15* (3), 891-902.

202. Chen, K. C.; Höistad, M.; Kehr, J.; Fuxe, K.; Nicholson, C., Theory relating in vitro and in vivo microdialysis with one or two probes. *Journal of Neurochemistry* **2002,** *81* (1), 108-121.

203. Snyder, K. L.; Nathan, C. E.; Yee, A.; Stenken, J. A., Diffusion and calibration properties of microdialysis sampling membranes in biological media. *Analyst* **2001,** *126* (8), 1261-1268.